Probing Fundamental Physics and Astrophysics With Tides and Deformations of Compact Stars

(Vincent) Shu Yan Lau

Hong Kong

Bachelor of Science (Physics), The Chinese University of Hong Kong, 2014

Master of Philosophy (Physics), The Chinese University of Hong Kong, 2017

A Thesis submitted to the Graduate Faculty

of the University of Virginia in Candidacy for the Degree of

Doctor of Philosophy

Department of Physics

University of Virginia

May 2024

Kent Yagi. Advisor, Chair

David Nichols. Member

Peter Arnold. Member

Phil Arras. Member

Probing Fundamental Physics and Astrophysics With Tides and Deformations of Compact Stars

(Vincent) Shu Yan Lau

(ABSTRACT)

Compact stars are the stellar evolution remnants no longer supported by thermal and radiation pressure. Since these objects have high densities and strong surface gravity, they provide a unique environment to study fundamental physics like nuclear interactions and gravity theory. Moreover, binary compact objects serve as strong gravitational wave sources, complementing the electromagnetic observations and offering new methods to probe new physics within the compact star environment. This thesis delves into several aspects of astrophysics, gravitation, and nuclear physics related to compact stars including white dwarfs and neutron stars. In astrophysics, we consider the prospects of measuring the tidal properties of white dwarfs using the precession of periastron of eccentric binaries. This provides an alternative method to measure tides within white dwarf binaries using gravitational waves. Additionally, we examine the stability of individual compact stars by relaxing the conventional assumption of isotropic stress, accounting for realistic astrophysical conditions that cause anisotropy. There, we find a new type of instability which is caused by the spontaneous growth of the non-radial oscillation modes as the star emits gravitational waves. In gravitation, we explore the potential of utilizing gravitational wave signals from galactic compact binaries to constrain the theory of gravity with future space-based detectors. We demonstrate that proper modeling of the astrophysical factors governing the orbital motion, like the tidal deformations or the influence of

magnetic field, is essential for placing meaningful constraints on alternative gravity theories with gravitational waves. Lastly, we also explore probing the deconfinement of quarks in the neutron star core by measuring the resonance effect of tides in a binary neutron star from the gravitational wave signals. We find that even the current generation of detectors can measure the effect of the quark stellar core given that the quarks are in a crystallized state with extreme rigidity. These studies demonstrate the utilization of gravitational wave observations from compact stars to push the boundaries of fundamental physics and astrophysics.

Dedication

Dedicated to Hongkongers from 2019, those who stood up and fought for freedom, those who spoke against totalitarianism and were politically persecuted, those who loved the place we once called home.

Acknowledgments

I would like to thank Kent Yagi, who has been a supportive and insightful mentor throughout my graduate study at the University of Virginia. I would not have achieved as much without his advice on research and encouragement to connect with fellow researchers through attending conferences and collaborations. I am also grateful to Phil Arras, the co-advisor of several of my research projects who is very knowledgeable. It happens many times that his short advice and comments turn out to fill the key missing pieces in my understanding of the subject matter. Besides, I appreciate all the support from my colleagues at the University of Virginia, especially the gravity group members. I am also deeply indebted to my MPhil advisor Pui-Tang Leung and co-advisor Lap-Ming Lin at the Chinese University of Hong Kong, for their precious guidance on research. I have greatly benefited from their influence on my academic approach and philosophy. Lastly, I am thankful to my beloved family and friends in Hong Kong for their support via video calls and messaging, despite the time difference. Even though we are thousands of miles apart, our constant calls keep me connected with the place I grew up in and the people I know.

Contents

List of Figures

List of Tables

Chapter 1

Introduction

In this thesis, we discuss several research topics related to compact stars. The purpose of this chapter is to (1) provide a qualitative overview of the physics involved, (2) summarize the research topics, (3) and review the literature and development in related fields. Some basic formalisms and theories related to the subsequent chapters will be explained in Chapter 2.

Unless otherwise specified, we use the $(-,+,+,+)$ metric sign convention and the geometrized unit systems with $G = c = 1$ throughout the thesis. The abbreviations and values of the constants are explained in Appendix A.

1.1 Compact stars

Compact stars are stellar objects with extremely high densities compared to normal luminous stars. This family includes the better-known "white dwarfs (WDs)" and "neutron stars (NSs)" as well as some exotic stars like the "strange stars". They are the remnant of stellar evolution and have many interesting properties that attract attention in not only astronomy but also various fields in fundamental physics like nuclear physics and gravitation.

Due to the extreme densities, the Fermi temperature of these compact stars is usually

several orders of magnitude higher than its temperature. As a result, they are mainly supported by degeneracy pressure against their own gravity. For WDs, the major support comes from the degeneracy pressure of electrons. For denser compact stars beyond the nuclear saturation density, the supporting force comes from the degeneracy pressure of hadrons or even deconfined quarks. Since these stars are extremely compact, as characterized by their strong surface gravity field, they are also good gravitational wave (GW) sources. Starting from the first direct detection of the GW signal from the binary black hole (BH) coalescence event GW150914 [1] and the first binary NS coalescence event GW170817 [2], GWs have been a promising tool for probing the properties of compact objects. To be specific, the tidal interactions between two compact stars can be measured from the phase of the GW signal. This provides a unique way to study physics in such a high-density environment with strong gravitational field. The future space-based detectors will also measure GWs from WD binaries within our galaxy, which lie below the frequency band of the current ground-based detectors.

1.1.1 White dwarfs

The WDs are the less compact, more commonly found member of the compact star family. They originate from the core of main-sequence stars with mass $\sim M_\odot$, after they have exhausted the fuel for nucleosynthesis, and ejected the outer layers. They are mainly supported by electron degeneracy pressure.

A typical WD has a mass $\lesssim 1\ M_\odot$, and a radius of $\sim 10^4$ km. This corresponds to a small compactness of 10^{-4}, defined by M/R, where M is the gravitational mass and R is the radius. As a result, the structure and the dynamics of WDs can be

approximated well with Newtonian gravity. Nevertheless, close double WD (DWD) binaries are strong GW emitters with relatively low frequencies <1 Hz. We will demonstrate the potential of studying astrophysics and gravity theory using the GW signals from these systems in Chapter 3 and 6.

1.1.2 Neutron stars

NSs are the remnant of a supernova explosion, which can come from a massive luminous star or the collapse of a WD after accreting enough mass to pass the Chandrasekhar limit ($\approx 1.4\ M_\odot$). Due to the uncertainties of the equation of state (EOS) in the high-density, low-temperature region of the quantum chromodynamics (QCD) phase space, the exact composition and the matter properties of a large portion of the NS interior remain uncertain. Terrestrial experiments also cannot reach such high densities at relevant temperatures. Therefore, astronomical observations of these objects provide valuable information to constrain nuclear physics within this phase space region.

A typical NS has a mass of about 1.4 $M_\odot$, and a radius of $\sim$ 10 km, making it extremely compact ($M/R \sim 0.1$). Binary NSs are strong emitters of GWs in the 100-1000 Hz frequency range that can be captured with the current generation of GW detectors.

A particular class of NS models predict the existence of deconfined quark matter (QM) to exist in the inner core of a NS. Those are referred to as hybrid stars (HSs). In Chapter 7, we discuss how GW signals from binary NS inspirals allow us to probe the existence of a particular model of QM.

1.2 Gravitational waves

1.2.1 Gravitational waves from compact binaries

GWs are the radiative gravitational fields generated from the time-varying mass distributions, analogous to the radiative part of an electromagnetic field. However, they enter in the quadrupolar order instead of the dipolar order within general relativity (GR)[1]. As the GW passes through matter, it produces strain that can be measured as a time variation of distances. However, they couple weakly with matter and therefore it requires sensitive detectors to measure even the strongest GW sources in nature.

The compact binary coalescence is the major source of GWs for the current interferometry-based detectors. It consists of the inspiral phase, the merger phase, and the post-merger phase. During inspiral, the binary loses orbital energy and the separation decreases. This gives a GW signal with increasing amplitude and frequency. At merger, the two objects come into contact and merge to form a highly asymmetric dynamical object in a short period. Afterward, the remnant gradually settles through emitting the excess energy in the postmerger phase. In the case of binary NS coalescence, it can be a BH right after merger, or a metastable NS, either the supramassive NS or hypermassive NS that exists for a short time, or a stable NS. For binary WDs, the merger happens at a much larger separation. The frequency corresponding to the final stage of inspiral therefore lies below the detection range of the ground-based detectors. As described in the next section, the planned space-based detectors will be able to capture the signals from compact binaries in the earlier stage of the inspiral where the frequency and frequency evolution rate are both much lower.

[1] Even for certain alternative gravity theories that predict the existence of dipolar or even monopolar GWs, their contributions have to be small to satisfy the experimental constraints.

1.2.2 Gravitational wave detectors

The ground-based interferometers are designed to measure GW signals of 10-1000 Hz, covering those from binary NS merger events. That includes both the current detectors like the advanced Laser Interferometer Gravitational-Wave Observatory (aLIGO), Virgo interferometer, Kamioka Gravitational Wave Detector (KAGRA), and GEO600 [3, 4]. There are also planned detectors with enhanced sensitivity within this frequency range, including the Cosmic Explorer (CE) and the Einstein Telescope (ET). Due to the seismic noise, these ground-based detectors are unable to probe the $\lesssim$10 Hz region of the GW spectrum.

To overcome this, there are also planned space-based detectors that are sensitive to lower frequency range down to 10^{-4} Hz, including the Laser Interferometer Space Antenna (LISA) [5], and Deci-hertz Interferometer Gravitational-Wave Observatory (DECIGO) [3, 6, 7]. They are expected to capture signals from DWD systems within the Milky Way. At frequencies below $\sim 10^{-4}$ Hz, it is expected that each frequency bin in the spectrum is populated with almost monochromatic GW signals from multiple galactic binaries and therefore cannot be individually resolved. These unresolved binaries are the main contributors to the noise in the low-frequency region.

The sensitivities of the above-mentioned detectors are shown in Fig. 1.1. The colored curves represent the characteristic strain originating from the noise expected in each detector. Colored bars are used to roughly indicate the strain level of the GW signals expected for each source.

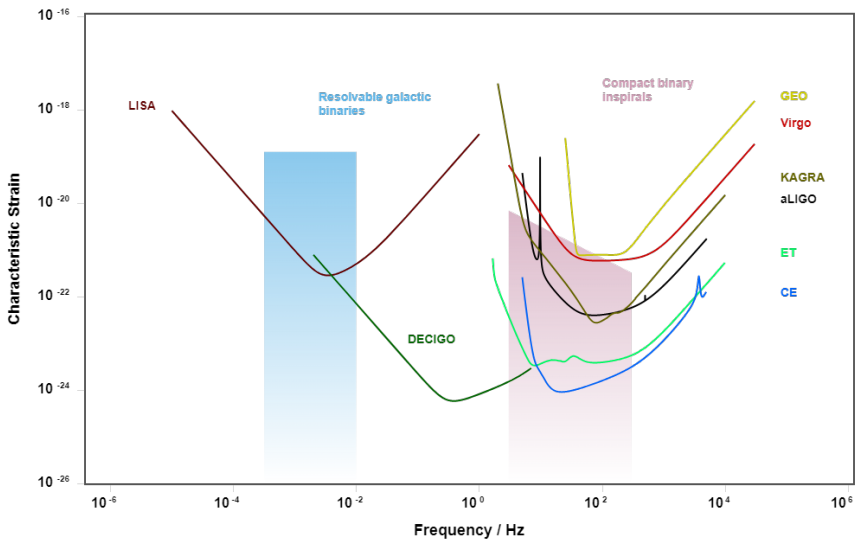

Figure 1.1: The sensitivity curves of various existing/ planned GW detectors and the characteristic strain of the GW signals from the corresponding sources. The figure is generated from the GW Plotter [8].

1.3 Tidal interactions

Unlike binary BHs, the orbits of binary compact stars are affected by finite size effects including tidally-induced deformations. The deviation of the stars from a perfect sphere affects the orbital evolution during inspiral and hence leaves an imprint in the phase of the GW signals [9–11]. The tidal interaction is specifically of interest as it carries the information of the stellar interior.

In the earlier stage of an inspiral, the tidal response is dominated by the equilibrium tide, where the two stars in the binary are effectively treated as fixed in space when we calculate the amount of tidal deformation [12]. To the leading order, this produces an extra attractive interaction within the binary that goes as $1/D^7$, where D is the orbital separation. Compared to the inverse square law of Newtonian gravity, it is 5 orders higher in power of $1/D$, making it a 5th post-Newtonian (5PN) effect. Due to the steep dependence on the orbital separation (and hence the GW frequency), such an

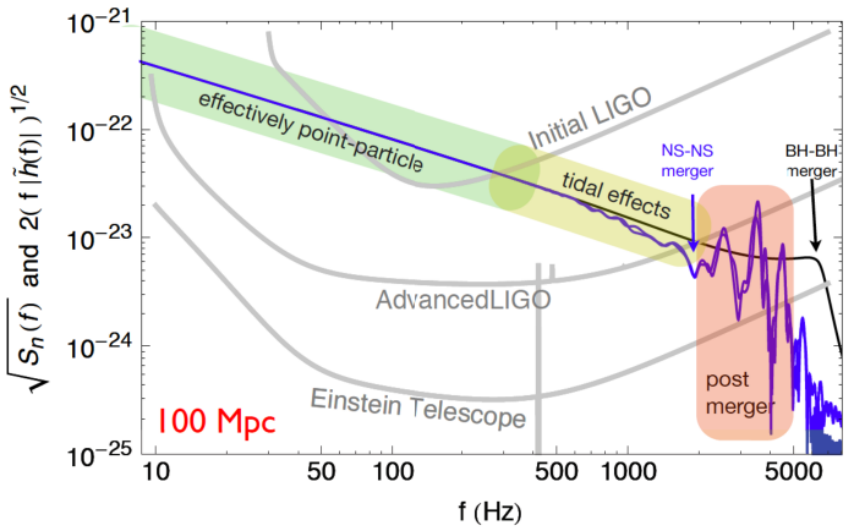

Figure 1.2: Example waveform spectrum of a binary NS and a binary BH in the frequency domain. Figure from [13], based on data from [14] for a source at 100 Mpc. The green region roughly indicates the frequency range in which the point-particle approximation works well for the waveform signal. In the yellow region, substantial deviations can be seen between the binary NS and the binary BH cases due to the tidal effect. The orange region highlights the very different post-merger signal from binary NSs compared to the binary BH case. The characteristic strains of LIGO and ET are also shown to indicate the required sensitivity to resolve the tidal effects and post-merger effects in binary NS systems.

effect becomes significant only when the stars are very close to each other. Figure 1.2 provides an example frequency-domain waveform of a binary NS and a binary BH in which the effect of tides appears just before the merger. The tidal effect can be captured with the current generation of detectors, while future detectors can also capture the post-merger part, providing additional constraints on the NS properties.

Tidal interaction is in general dynamical as the deformed star has its own restoring force that sets the natural frequencies. The equilibrium tide corresponds to the limit where the forcing frequency, i.e., the frequency of the tidal force from the companion star, is much less than the natural frequency. As the orbital frequency increases, the dynamical tide becomes more significant. The leading dynamical tide effect gives

an extra $1/D^{10}$ correction to the binary interaction (i.e., an 8PN effect) and further accelerates the phase evolution of the GW signal emitted. Meanwhile, resonance occurs as the orbital frequency reaches the natural frequencies. In this case, the orbital energy is transferred into the internal oscillations of the star(s), resulting in a sudden phase shift in the orbital motion, and also the GW signal. This shift is the effect of the tidal reaction force and tidal torque during the resonance time window, which is short compared to the whole inspiral timescale. Being able to measure the dynamical tide would provide much richer information about the stellar interior.

The left panel of Fig. 1.3 shows a schematic time-domain GW strain signal of the equilibrium tide and non-resonant dynamical tide effect on the phase. The red curve corresponds to the case with the acceleration of inspiral due to tides and it leads in phase compared to the case without it. The right panel illustrates the effect of resonance of dynamical tidal interactions, where a mode is excited as the tidal forcing frequency sweeps through its natural frequency, producing a sudden phase shift in the signal. The waveform in red is obtained by trimming a portion of the waveform in black starting from $t = t_{\rm res}$ and joining it with a later portion of the inspiral signal, which corresponds to a phase shift of the signal. In Chapter 7, we discuss how these resonance effects allow us to probe the interior structure of a NS.

1.4 Stellar pulsation modes

The standing waves permitted in a star form a spectrum of stellar pulsation modes. These modes correspond to the natural frequencies of the star which characterize the stellar internal composition and density profile. These modes can be excited under a dynamical tidal field as mentioned in 1.3, leaving an imprint in the GW phase.

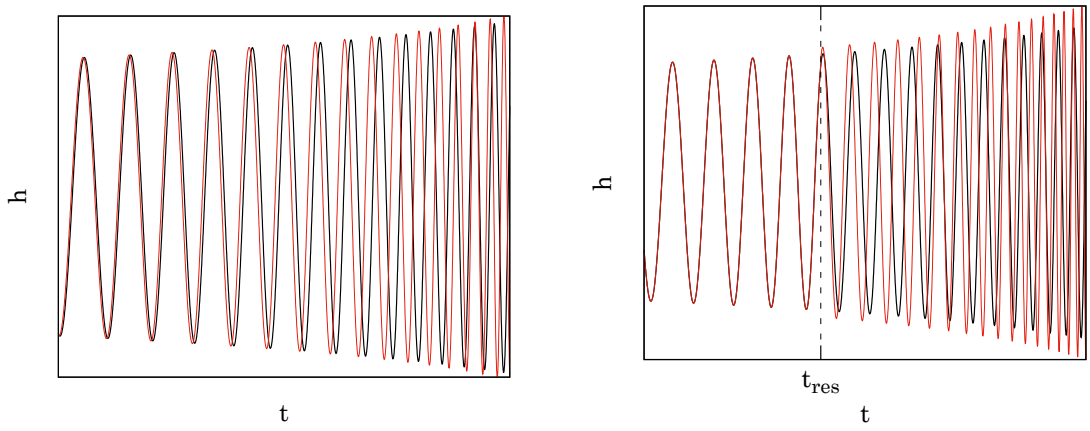

Figure 1.3: A schematic time-domain waveform of an inspiralling compact binary system. In the left panel, the red curve corresponds to the system affected by the 5PN effect from equilibrium tides and shows a lead in phase while the system of the black curve does not. In the right panel, the red curve corresponds to the system with a mode resonance at $t = t_{\rm res}$. At this point, the signal skips a certain amount in phase (and time) and is joined with a later part of the original signal.

Some of these modes may produce observable electromagnetic (EM) signals through, e.g. causing the fracture or melting of the solid layers of the star [15, 16]. With the advancement in multimessenger astronomy over the years, the detection of some of the pulsation modes is expected in the future [17–22].

Within Newtonian theory, the adiabatic pulsation modes are normal modes described by real frequencies. For even parity (polar) modes, the well-known ones include the fundamental (f-)modes, the pressure (p-)modes, and the gravity (g-)modes. In the original classification by Cowling [24], the naming of these modes is based on the local propagation behavior of the waves that form the modes. For example, via a local analysis, the g-modes can be conceived as the standing waves formed by propagating internal gravity waves with buoyancy as the main restoring force, while the p-modes are those formed from acoustic waves supported by pressure variations [25–27]. In typical stellar models, the g-modes and p-modes have propagation zones within the

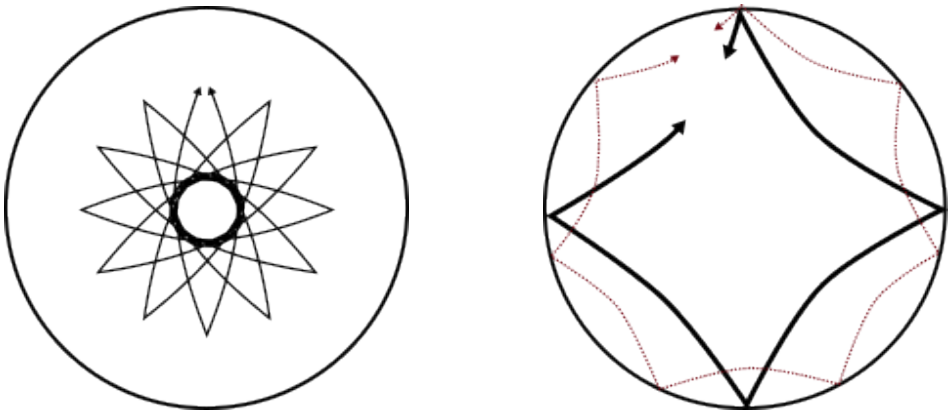

Figure 1.4: A schematic depiction of the propagating waves within the star that form the g-modes (left panel) and p-modes (right panel). The lines with arrows represent the direction of propagation of an internal wave with certain frequencies. Notice that depending on the frequency of the waves, some regions do not permit r-direction propagations (evanescent, or exponential zones). The illustration is produced following the idea of Fig. 1 in [23].

stellar interior where the wave vectors have radial components (see Fig. 1.4). The regions for the propagation zones vary depending on the thermal states of the stellar models. The f-modes are mainly formed from gravity waves propagating along the stellar surface in the transverse directions, with little or no components along the radial direction. This particular class of modes is important in tidal interactions as they have the largest overlap with the external tidal field.

In Chapter 7, we also consider a special interfacial (i-)mode [28] that exists only in stars with an interior interface, where quantities like the density or shear modulus are discontinuous (e.g., a first-order phase transition). These modes can be depicted as the standing waves formed from the interface waves propagating along the interface. An illustration of an f-mode and an i-mode are shown in Fig. 1.5.

In GR, the non-radial modes that produce moments beyond the dipolar order cause GW emission, carrying the mode energy away from the system. In this case, the pulsation modes would have complex frequencies and are known as quasi-normal

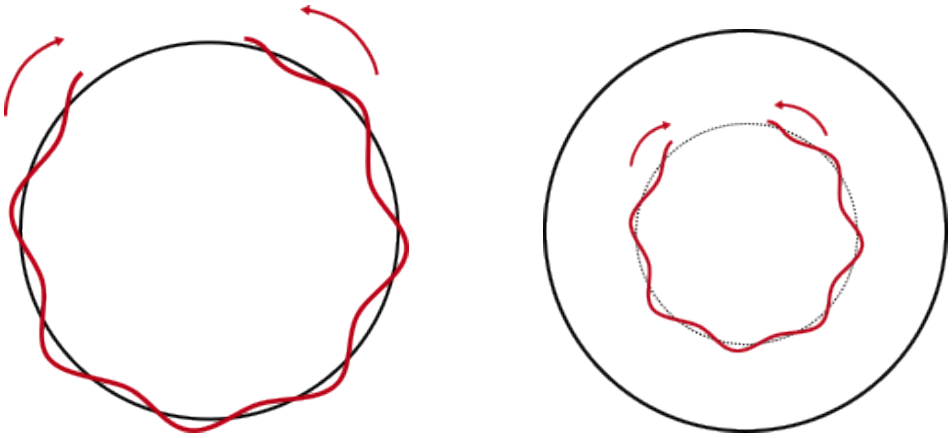

Figure 1.5: A schematic depiction of the major transverse propagating waves that form the f-modes (left panel) and i-modes (right panel). Note that these waves in transverse directions happen at all r. The red line shows the place where the amplitude of these waves is at maximum. In the right panel, the dashed line represents the interface with a jump in density or shear modulus.

modes (QNMs), as in other open systems (e.g., in electromagnetic cavities [29–31]). The above-mentioned pulsation modes, like the f-modes and g-modes, decay exponentially with time due to GW emission, described by the imaginary part of the frequencies. These modes with Newtonian counterparts are sometimes called the "fluid modes" in relativistic stars [32]. Since the vacuum permits wave-like solutions of the spacetime perturbations, new pulsation modes that involve almost no matter motion and are known as "spacetime modes" also arise [32]. These modes do not have Newtonian counterparts and usually have short damping times. They are not studied in this thesis.

1.5 Research overview

The GWs from compact stars open up a wide variety of studies in different fields. This thesis discusses relevant research in astrophysics, gravitation, and nuclear physics. In

this section, we will briefly go through the individual research topics and the related literature. The details of each topic are given in the subsequent chapters.

1.5.1 Astrophysics: Binary orbital mechanics, stability of compact stars

Measuring tides in eccentric double white dwarfs

Measuring the tidal properties of WDs from the GW signal can be challenging [33] as the majority of the sources have a relatively large separation for the tide to cause a measurable dephasing (schematically) shown in Fig. 1.3. In some rare DWD systems that have non-zero eccentricity, however, the periastron precession provides an alternative way to measure tides.

In Chapter 3, we extend the study using the precession effect to measure tide in [34], which considers only the equilibrium tide, to include the dynamical tide and perform a GW signal analysis to estimate its detectability.

Effect of tides in binary evolution

In eccentric binary systems, the dynamical tide provides a channel for the orbit to exchange energy with the internal deformations of the stars. This causes the orbital elements, like the semi-major axis and eccentricity, to evolve over many orbits. In systems with low eccentricities, this evolution is generally stable and the orbital elements oscillate back and forth over long-term evolution. However, for certain systems with high eccentricities, the evolution becomes chaotic [35–38].

An iterative mapping method has been developed to efficiently compute the dynamical

tide effect on the orbital evolution. This method first considers the secular effect of the tide on the orbital elements over one complete orbit and uses it to update the orbit at each pericenter passage. The original method by [38] has made several assumptions that are valid only in highly eccentric systems. The method therefore becomes less accurate as we go to intermediate eccentricities. For this reason, we derive an improved version of the mapping method by taking into account the above two missing factors.

In Chapter 4, we extend the formalism to systems with low eccentricities. This method allows us to better predict the long-term fate of close eccentric binaries.

Non-radial stability of neutron stars

As introduced in Sec. 1.4, the non-radial oscillation modes in GR (except the dipole modes) have complex frequencies and are known as QNMs. The sign of the imaginary part governs the stability of the oscillations, whether the mode has an exponential decay or a growth with time.

The stellar pulsation modes of relativistic stars have been extensively studied in the past few decades (e.g., [39–42]). However, the focus has been put on stars made of perfect fluid with isotropic pressure (at the background level[2]). There is no existing fully consistent GR formalism for anisotropic NSs before this work.

Local anisotropy can exist within an NS in various scenarios involving elasticity [46–48], superfluidity [49, 50], pion condensation [51], strong magnetic field [52, 53], and viscosity [54]. Certain exotic relativistic stars are also predicted to have anisotropic stress, like boson stars [55–57], strange stars [58, 59], dark matter stars [60], and

[2]There are some studies of QNMs of NSs with elastic effects that enter in the perturbative level [43–45].

gravastars [61, 62]. The solution to a static spherically symmetric anisotropic NS was first studied in [63]. After that, much work has been done on calculations of the NS structure with different anisotropic EOSs as well as assessing the radial stability [64–72].

In Chapter 5, we perform the first study of non-radial pulsations of anisotropic NSs in full GR. We discover an interesting instability in the p-modes that can only be found in the full GR theory. Previous related work on anisotropic NSs does not capture this instability due to their approximations, including taking the Newtonian limit [65] or the Cowling approximation [73] (i.e., neglecting the metric perturbations).

1.5.2 Gravity theory: Testing general relativity

Although GR has been a successful theory of gravity that satisfies all the observational constraints from the solar system to cosmological scales so far, there still exists an enormous number of alternative gravity theories that are well-motivated by fundamental physics or cosmological observations, and are consistent with the existing tests. Testing GR allows us to narrow down the variety of these alternatives and hence probe the fundamental nature of gravity.

The GW signals from galactic DWD binaries detected by LISA can potentially improve the current bounds on certain non-GR theories, especially for those effects entering the negative PN order [74, 75]. However, the tests require accurate modelling of the frequency evolution of the signal due to all astrophysical factors, like the tidal deformations [76] and magnetic interactions [77]. These effects enter different PN orders and can affect the phase in a similar manner as the non-GR effects. Failure to include these in the waveform model can lead to systematic errors in the measured

non-GR effects.

In Chapter 6, we extend the previous work by considering the bounds on non-GR effects at different PN orders using GW signals from DWDs. We further explore the systematic errors on the bound due to mismodelling of the astrophysical factors.

1.5.3 Nuclear physics: Quark matter

QCD provides the theoretical framework describing strong force. This theory can be perturbatively expanded and used to make meaningful predictions at extremely high densities, where the quarks are expected to behave as weakly interacting Fermi gas. For this reason, matter is expected to undergo a transition from the hadronic matter (HM) to a deconfined QM state at a certain density. However, the nonperturbative nature of QCD at lower densities makes it difficult to theoretically predict the properties of this transition and the phase deep inside the core.

Alternatively, observations of NSs can place constraints on the phase transition. A strong first-order phase transition that features a large density discontinuity between the hadronic and quark phases can affect the measurement of the stars. Recent electromagnetic observations [78–80] and GW observations [81, 82] have made the measurements of mass, radius, and tidal deformability of NS possible. To constrain the phase transition, one way is to use the mass-radius relations (e.g., [83–86]), via the softening of the EOS or the twin star scenarios[3]. Another way is to use the EOS-insensitive relation between the tidal deformability (the Love number) and the compactness (C), known as the Love-C relation [87–89]. If one can simultaneously measure the Love number (e.g., through GW signal [90]) and the compactness (e.g.,

[3]Twin stars correspond to two stable configurations of NS-like objects that have the same mass but different radii.

through the X-ray emission [79]), they can compare it with the universal Love-C relation that holds for NSs without the transition [91].

Furthermore, the QM is expected to exhibit color superconductivity, where the quarks form condensates of Cooper pairs. One interesting color superconducting phase is the crystalline color superconducting (CCS) phase [92–97], where the QM exists as an extremely rigid solid[4].

The phase transition and the solid core can give rise to unique stellar pulsation modes that are distinctive from other NS models, one of which being the interfacial (i-)modes [13, 15, 28, 106]. The properties of this mode depend strongly on the phase transition, and also on the elastic properties of the QM phase. As introduced in Sec. 1.3, the resonance of these modes due to dynamical tidal interactions can cause a phase shift in the GW signal.

In Chapter 7, we perform a GW waveform analysis to estimate the measurability of the i-mode from binary NS inspirals, assuming the core is composed of the rigid crystalline QM phase.

[4]The astrophysical properties of systems having such a rigid phase are investigated in [98–105].

Chapter 2

Theory

This chapter summarizes the major theories and formalisms from literature or textbooks used in this thesis so that interested readers can have a basic understanding of the methods involved without needing to go through the individual references.

2.1 Static stellar structure

One crucial step in studying compact star physics is to construct the background stellar model. In this thesis, we mainly consider non-rotating compact stars constructed with the method described in this section.

In GR, the background structure of a non-rotating star is determined by the Tolman-Oppenheimer-Volkoff (TOV) equations. These equations follow from the Einstein field equations applied on a static spherically symmetric spacetime with perfect fluid. We define the metric by

$$ds^2 = -e^{\nu}dt^2 + e^{\lambda}dr^2 + r^2 d\Omega^2, \tag{2.1}$$

where ν and λ are functions of r while $d\Omega$ is the unit 2-sphere line element. The

stress energy tensor for perfect fluid is given by

$$T^{\alpha\beta} = (\rho + p)u^{\alpha}u^{\beta} + pg^{\alpha\beta}, \tag{2.2}$$

where u^{α} is the four velocity vector. The TOV equations read (see, e.g., [107, 108])

$$\nu' = 2\frac{m + 4\pi r^3 p}{r^2}e^{\lambda}, \tag{2.3}$$

$$p' = -(\rho + p)\frac{\nu'}{2}, \tag{2.4}$$

$$\lambda' = 2\frac{-m + 4\pi r^3 \rho}{r^2}e^{\lambda}, \tag{2.5}$$

$$e^{\lambda} = \left(1 - \frac{2m}{r}\right)^{-1}, \tag{2.6}$$

where p is the local pressure, ρ is the energy density, m is interpreted as the gravitational mass enclosed within a radius r. Here, the superscript prime denotes derivative with respect to r. The stellar surface is defined at $p(R) = 0$, with R being the stellar radius.

This set of equations can be easily reduced to the Newtonian limit by taking $p/\rho \to 0$, $m/r \to 0$, and $r^3 p/m \to 0$:

$$p' = -\frac{\rho m}{r^2}, \tag{2.7}$$

$$m' = 4\pi r^2 \rho. \tag{2.8}$$

In both cases, ρ is not determined by the differential equations and has to be informed by the EOS of the matter.

2.2 Equation of state

A cold compact star has a temperature much lower than the Fermi temperature, allowing us to ignore the thermal effects. In thermal and chemical equilibrium, its EOS can then be expressed as a single-variable relation between the energy density and the pressure, i.e., $\rho = \rho(p)$ [109]. The EOS can either be given in the tabulated form, based on complicated nuclear physics computations involving many-body interactions, or in an analytic form for simplified models.

2.2.1 Tabulated equations of state

Most EOSs obtained from nuclear theory, based on effective nucleonic interactions or perturbative QCD, are presented as multi-parameter tables [110]. At equilibrium cold dense matter, the table is reduced to a single parameter, usually chosen as the baryonic number density n_b. Hence, the values of ρ and p both depend on a discrete list of n_b. An example used in this thesis is the SLy4 [111] EOS table, which describes the cold NS matter at beta equilibrium based on a Skyrme-type effective nucleonic interactions "SLy" [112]. Another example is the NL3 EOS [113] (see Fig. 2.1).

These EOS tables are often used to construct the static background of NSs. The intermediate values of p and ρ between data points of the tables are conventionally extracted using a linear-logarithmic interpolation. In Chapters 5 and 7, we employ several EOS tables to construct the NS structures.

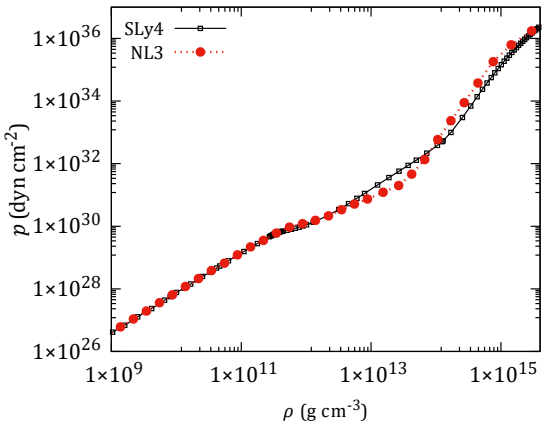

Figure 2.1: The p-ρ relations of the EOS tables SLy4 and NL3.

2.2.2 Analytic equations of state

In simple models, one can obtain the EOSs in analytic forms. Whenever they are available, these EOSs are preferred over the tabulated ones as they avoid the interpolation error.

Simplified cold WD models assuming the pressure comes from electron degeneracies and the energy density comes from the rest mass of the nucleons can be obtained analytically. Here, we briefly summarize the EOS provided in [107]

$$p = \frac{m_e c^2}{\lambda_e^3}\phi(x), \tag{2.9}$$

$$\rho = \mu_e m_u n_e(x), \tag{2.10}$$

where $m_e = 9.108 \times 10^{-28}$ g is the mass of an electron, $\lambda_e = \hbar/(m_e c) = 3.862 \times 10^{-11}$ cm is the reduced Compton wavelength, μ_e is the mean molecular weight and is taken as 2 for typical WDs with low hydrogen content, $m_u = 1.661 \times 10^{-24}$ g is the atomic mass unit, n_e is the electron number density and is a function of x by

inverting its definition: $x = \lambda_e(3\pi^2 n_e)^{1/3}$, and ϕ is a function given by

$$\phi(x) = \frac{1}{8\pi^2}\left[x\sqrt{1+x^2}\left(\frac{2}{3}x^2 - 1\right) + \ln\left(x + \sqrt{1+x^2}\right)\right]. \tag{2.11}$$

In practice, we need to invert Eq. (2.9) numerically to obtain $\rho(p)$. This can be done with a root-finding scheme like the secant method or Newton's method. In Chapters 3 and 6, we employ this EOS to construct the WD models.

Another commonly used simplified model in astrophysics is the polytropic EOS. This EOS is a phenomenological model that partially captures the properties of matter in certain density ranges. The form of the polytropic EOS is

$$p = K_0 n^\Gamma, \tag{2.12}$$

$$\begin{aligned}\rho &= \frac{K_0 n^\Gamma}{\Gamma - 1} + \left(\frac{K_0}{K}\right)^{1/\Gamma} n \\ &= \frac{p}{\Gamma - 1} + \left(\frac{p}{K}\right)^{1/\Gamma},\end{aligned} \tag{2.13}$$

where n is the particle number density, Γ is called the polytropic index, K_0 and K are also parameters of the model. To relate ρ and p, we simply use the last equality of Eq. (2.13) that contains two parameters Γ and K. To obtain the Newtonian limit, we simply set $p/(\Gamma - 1)$ to zero.

Note that this model can capture the EOSs of classical degenerate Fermi gas with $\Gamma = 5/3$ and the ultra-relativistic case with $\Gamma = 4/3$. In Chapter 5, we use this EOS to construct some of the anisotropic NS models. In some NS studies, the above model is extended to piecewise polytropic EOSs which consists of several polytropic models with different polytropic indices joined together. We have not employed such models in this thesis.

Quark matter (QM) is expected to behave as free Fermi gas at extreme densities. As a result, it can also be described with analytical EOSs in the perturbative region. A parametrized EOS is proposed in [114] to model QM, including the effects of quark interactions and color superconductivity. The model is written as

$$p = \frac{3}{4\pi^2} a_4 \mu_q^4 - \frac{3}{4\pi^2} a_2 \mu_q^2 - B_{\text{eff}}, \tag{2.14}$$

$$\rho = \frac{9}{4\pi^2} a_4 \mu_q^4 - \frac{3}{4\pi^2} a_2 \mu_q^2 + B_{\text{eff}}. \tag{2.15}$$

where p is the pressure, μ_q is the quark chemical potential, and $(a_4, a_2, B_{\text{eff}})$ are phenomenological parameters. The physical meaning and the ranges of the parameters are discussed in [114]. The parameter a_4 accounts for the QCD coupling constant and takes a value between 0 and 1, and a_2 is the contribution from both the pairing gap of the color-superconducting phase and the strange quark mass. The effective bag constant B_{eff} models the effect of confinement. In the case of the simplest MIT Bag model consisting only of free ultrarelativistic quarks, $a_2 = 0$, and the bag constant, B_{MIT}, lies within the range of 145 MeV $< B_{\text{MIT}}^{1/4} <$ 160 MeV (see, e.g., [115] and references therein). In the modified Bag model, it is instead treated as an arbitrary parameter [114].

This EOS is used to model the QM in the HS core in Chapter 7.

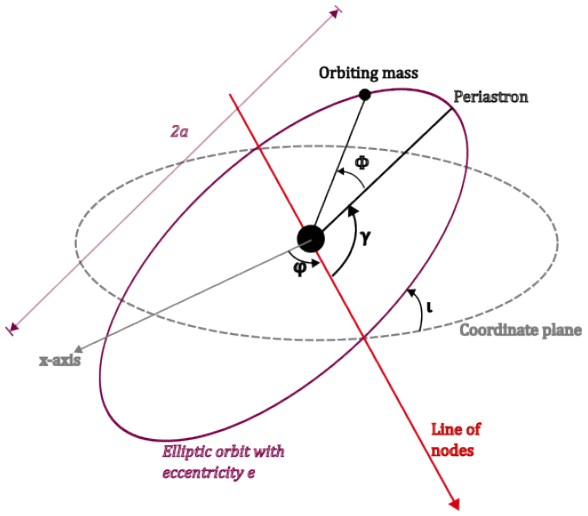

Figure 2.2: The orbital elements of a binary system. The semi-major axis a and eccentricity e specifies the shape of the orbit. Three angles are used to specify the orientation of the orbit relative to the coordinate system: the argument of periastron γ, the inclination angle ι, and the longitude of ascending node φ. The remaining orbital element, the time of periastron passage T, is not shown here. Aside from the six orbital elements, the true anomaly Φ is used to specify the position of the orbiting mass.

2.3 Orbital mechanics of binary compact stars

2.3.1 Keplerian orbits

The orbital motion of a binary compact star system is dominated by Newtonian gravity except in the late inspiral stage. We first give a brief review of the Keplerian solution of bounded binary systems.

A Keplerian orbit is described by six orbital elements, namely the semi-major axis a, the eccentricity e, the argument of pericenter γ, the time of pericenter passage T, the inclination angle ι, and the longitude of ascending node φ, as shown in Fig. 2.2.

The Keplerian solution gives

$$D(u) = a(1 - e\cos u), \tag{2.16}$$

$$\cos\Phi(u) = \frac{\cos u - e}{1 - e\cos u}, \tag{2.17}$$

where D is the orbital separation, Φ is the true anomaly that gives the angular position with respect to the pericenter angle γ. The parameter u is the eccentric anomaly and is related to time and orbital frequency Ω through Kepler's equation

$$t - T = \frac{1}{\Omega}(u - e\sin u), \tag{2.18}$$

and Ω is given by Kepler's third law

$$\Omega = \sqrt{\frac{m_1 + m_2}{a^3}}. \tag{2.19}$$

For binary systems, we use small letters m_1 and m_2 to represent the masses of the stars in the binary.

The orbital energy $E_{\rm orb}$ and angular momentum $L_{\rm orb}$ are given by

$$E_{\rm orb} = -\frac{m_1 m_2}{2a}, \tag{2.20}$$

$$L_{\rm orb} = \sqrt{\frac{a(1-e^2)}{m_1 + m_2}}\, m_1 m_2. \tag{2.21}$$

2.3.2 Perturbed Keplerian formalism

When there is a small force other than Newtonian gravity in the orbital interaction, a useful way to describe the orbit is the method of osculating orbits. At any given

moment, the orbit can be described by a set of orbital elements of a Keplerian orbit with the same instantaneous position and velocity. The orbital elements become time-dependent as a result. The secular evolution of the orbital elements is governed by the Burns equations [116]. We employ the formulation summarized in [117]:

$$\frac{da}{dt} = \frac{2}{\Omega\sqrt{1-e^2}}\left[a_r e \sin\Phi + a_\Phi(1+e\cos\Phi)\right], \tag{2.22}$$

$$\frac{de}{dt} = \frac{\sqrt{1-e^2}}{\Omega a}\left[a_r \sin\Phi + a_\Phi(\cos\Phi+\cos u)\right], \tag{2.23}$$

$$\frac{d\gamma}{dt} = \frac{\sqrt{1-e^2}}{\Omega a e}\left[-a_r\cos\Phi + a_\Phi \sin\Phi\left(\frac{2+e\cos\Phi}{1+e\cos\Phi}\right)\right], \tag{2.24}$$

$$\frac{dT}{dt} = \frac{3}{2a}\frac{da}{dt}(T-t) + \frac{\sqrt{1-e^2}}{\Omega}\frac{d\gamma}{dt} + \frac{2(1-e^2)}{\Omega^2 a}\frac{a_r}{1+e\cos\Phi}, \tag{2.25}$$

where a_r and a_Φ are the acceleration due to the perturbing force in the radial and azimuthal directions respectively. Note that a and Ω (related by Eq. (2.19)) are both used here so that the mass of the binary does not explicitly appear.

In this thesis, we consider only the planar systems without forces in the out-of-plane direction. Therefore, the remaining two orbital elements are constant and not listed here. We apply the above formalism to determine the effect of tidal interaction on the orbital elements of DWD binaries in Chapters 3, 6 and 4.

2.4 Tidal interactions

In this section, we introduce the method to compute the tidal deformations within a star. For the equilibrium tide, we review both the Newtonian and GR formalism describing small deformations. For the dynamical tide, a fully consistent GR pertur-

bation formalism is currently unavailable[1] and we focus on Newtonian formalism.

2.4.1 Equilibrium tide

Compact stars within a binary are tidally deformed. When the orbital separation is large, the tidal interaction is dominated by the equilibrium tide, which neglects the natural response rate of the bodies under deformations. At each multipole, the equilibrium tide depends on a single parameter known as tidal deformability λ_ℓ. For instance, in the quadrupole order

$$Q_{ij} = -\lambda_2 \mathcal{E}_{ij}, \tag{2.26}$$

where Q_{ij} is the mass quadrupole moment, and $\mathcal{E}_{ij}$ is the external tidal field. The GR formalism is given in [120–122]. We briefly summarize the procedures by [123] involved in computing λ_2 below.

We first set the origin at one of the stars in the binary. We write the (Eulerian) metric perturbation as [124]

$$\delta g_{\alpha\beta} = \sum_{\ell m} \mathrm{diag}\left\{-e^{\nu(r)}H_0(r), e^{\lambda(r)}H_2(r), r^2K(r), r^2K(r)\sin^2\theta\right\} Y_{\ell m}, \tag{2.27}$$

and the stress energy tensor (Eq. (2.2)) is under time-independent perturbations. The equation governing the deformation is then obtained from the perturbed Einstein field

[1]The GR consistent dynamical tide has been formulated to the subleading order in orbital frequency by neglecting all resonances [118]. This formalism has been recently extended to capture the resonance effects through a resummation of the expansion in orbital frequency and include the viscous dissipation [119]. Nevertheless, it is still not the full formalism without small frequency expansions and resummations.

equations. For $\ell = 2$, the equation can be written as

$$ry' + y^2 + ye^{\lambda}\left[1 + 4\pi r^2(p-\rho)\right] + r^2 Q(r) = 0, \tag{2.28}$$

where $y = rH_0'/H_0$ is a function of r, and $Q(r)$ is given by

$$Q(r) = 4\pi e^{\lambda}\left[5\rho + 9p + (\rho+p)\frac{\rho'}{p'}\right] - \frac{6e^{\lambda}}{r^2} - (\nu')^2. \tag{2.29}$$

Equation (2.28) is integrated from $r = 0$, with $y(0) = 2$, towards the stellar surface. Across any interface where the density is discontinuous, the quantity at the two sides, $y(R_i - \epsilon)$ and $y(R_i + \epsilon)$ with $\epsilon \to 0^+$, are related by

$$\left[y - \frac{4\pi r^3 \rho}{m + 4\pi r^3 p}\right]_{R_i} = 0, \tag{2.30}$$

where R_i is the radial location of the interface, and the square bracket denotes the difference between the quantities enclosed evaluated at the two sides of the interface.

The tidal deformability can then be obtained by matching with the exterior solution of the metric, and the solution is explicitly written as

$$\begin{aligned}\lambda_2 =& \frac{16M^5}{15}(1-2C)^2\left[2 + 2C(y-1) - y\right]\Bigg\{2C\Big[4(1+y)C^4 + (6y-4)C^3 + (26-22y)C^2 \\ &+ 3C(5y-8) - 3y + 6\Big] + 3(1-2C)^2\big[2 - y + 2C(y-1)\big]\log(1-2C)\Bigg\}^{-1},\end{aligned} \tag{2.31}$$

where y is evaluated at $R + \epsilon$, M is the total gravitational mass, $C = M/R$ is the compactness.

The Newtonian limit is obtained by taking $p/\rho \to 0$, $r^3 p/m \to 0$, and $m/r \to 0$. This reduces Eq. (2.28) and Eq. (2.31) to

$$ry' + y^2 + y + \left[-6 + 4\pi\rho r^2 \frac{\rho'}{p'}\right] = 0, \tag{2.32}$$

$$\lambda_2 = \frac{R^5}{3}\left(\frac{2-y}{3+y}\right). \tag{2.33}$$

The deformed body causes a change in the orbital interaction. Following the derivation in [12], this extra acceleration is

$$\mathbf{a}_{\text{tide}} = -\frac{9(m_1+m_2)}{D^7}\frac{m_2}{m_1}\lambda_{2,1}\mathbf{n}, \tag{2.34}$$

where $\mathbf{a}_{\text{tide}}$ corresponds to the acceleration on star 1, $\mathbf{n}$ is the unit vector in the radial direction from star 2, and $\lambda_{2,1}$ here refers to the tidal deformability ($\ell = 2$) of star 1.

2.4.2 Dynamical tide

The equilibrium tide introduced in Sec. 2.4.1 has ignored the natural response rate of the body, which is classified by its natural frequencies. In Newtonian gravity, the star has a set of normal modes that form a complete basis so that we can write any small deformations as a superposition of these modes. This allows us to perceive dynamical tidal deformation as excitations of different normal modes of the star. However, this device is not applicable in GR as the QNMs of a relativistic star do not form a complete basis (e.g., [13]). For this reason, a fully consistent relativistic formalism for the dynamical tidal interactions does not exist currently. We focus on

a brief summary of the Newtonian formalism in this section. Further details can also be found in [125, 126].

The classical Lagrangian perturbation theory [127, 128] allows us to describe the fluid motion inside a star at any instant in terms of the Lagrangian displacement vector $\boldsymbol{\xi}(t, \mathbf{x})$. In the center-of-mass frame of one of the stars in a binary, whose quantities are marked with the subscript 1 hereafter, the position vector of a fluid element in the perturbed star is given by $\mathbf{x} + \boldsymbol{\xi}(t, \mathbf{x})$, where $\mathbf{x}$ is the original position of the fluid element. The vector $\boldsymbol{\xi}(t, \mathbf{x})$ satisfies the equation of motion:

$$\rho \ddot{\boldsymbol{\xi}} = \boldsymbol{f}[\boldsymbol{\xi}] - \rho \boldsymbol{\nabla} U, \tag{2.35}$$

where $\boldsymbol{f}[\boldsymbol{\xi}]$ represents the internal restoring force against deformations, ρ is the density and U is the tidal potential due to the companion star, denoted with subscript 2. We follow the formulation in [125] to determine the tidal response and the corresponding back-reaction on the orbit.

We first focus on the deformation of star 1. The induced quadrupolar deformation causes star 1 to exert an extra force in addition to the point-mass contribution onto the orbit. The contributions from star 2 on the orbital motion are completely symmetric to that from star 1 and can be found by switching the labels, as well as noting that the azimuthal angle Φ from star 2 differs by a phase of π.

Following [125], we expand the phase space vector as

$$\begin{bmatrix} \boldsymbol{\xi} \\ \dot{\boldsymbol{\xi}} \end{bmatrix} = \sum_{\alpha} q_{\alpha}(t) \begin{bmatrix} \boldsymbol{\xi}_{\alpha}(\mathbf{x}) \\ -i\omega_{\alpha} \boldsymbol{\xi}_{\alpha}(\mathbf{x}) \end{bmatrix}. \tag{2.36}$$

Here, $\boldsymbol{\xi}_{\alpha}$ represents an eigenmode with an eigenfrequency ω_{α}, $q_{\alpha}(t)$ is the excitation

amplitude of the mode and the subscript α represents the set of quantum numbers (n, ℓ, m, s), where the former three specifies an eigenmode, and $s = \pm 1$ specifies the sign of the frequency to account for a phase space mode and its complex conjugate. The eigenvalue problem is written as

$$-\rho\omega_\alpha^2 \boldsymbol{\xi}_\alpha = \boldsymbol{f}[\boldsymbol{\xi}_\alpha]. \tag{2.37}$$

The eigenmodes are normalized such that

$$2\omega_\alpha^2 \int d^3x \rho \boldsymbol{\xi}_\alpha^* \cdot \boldsymbol{\xi}_\alpha = \frac{Gm_1^2}{R_1}. \tag{2.38}$$

The detail of Eq. (2.37) and the eigenvalue problem can be found in e.g., [26, 129]. Note that we use another normalization in Chapter 7 for consistency with the formalism applied.

In the comoving frame of star 1, the mode amplitude $q_\alpha(t)$ satisfies the equation [125, 126]

$$\dot{q}_\alpha + i\omega_\alpha q_\alpha = i\omega_\alpha U_\alpha, \tag{2.39}$$

where

$$U_\alpha = \frac{m_2}{m_1} \sum_{\ell m} W_{\ell m} I_{\alpha \ell m} \left(\frac{R_1}{D}\right)^{\ell+1} e^{-im\Phi}. \tag{2.40}$$

Here, D is the orbital separation, Φ is the azimuthal coordinate of star 2 as seen by star 1, and $W_{\ell m}$ is given by $[4\pi/(2l+1)]Y_{\ell m}(\pi/2, 0)$. We have also defined the overlap

integral $I_{\alpha\ell m}$

$$I_{\alpha\ell m} = \frac{1}{m_1 R_1^\ell} \int d^3x \rho \boldsymbol{\xi}_\alpha^* \cdot \boldsymbol{\nabla} \left[r^\ell Y_{\ell m}(\theta, \phi) \right], \tag{2.41}$$

where $Y_{\ell m}$ are the spherical harmonics and (r, θ, ϕ) are the spherical coordinates with the origin at the stellar center of the star 1. Note that since we have not included the Coriolis force in Eq. (2.35), $I_{\alpha\ell m} = I_\alpha \delta_{\ell,\ell_\alpha} \delta_{m,m_\alpha}$, where $\delta_{i,j}$ is the Kronecker delta function and ℓ_α, m_α are the spherical harmonic indices contained in α. For simplicity, we use I_α in the following since we do not consider calculations that fully account for the Coriolis effect. Following Appendix C of [126], the orbital acceleration due to the tidally deformed stars is given by

$$\mathbf{a}_{\rm tide} = -\frac{m_1 + m_2}{R_1^2} \sum_\alpha W_{\ell m} I_\alpha \left(\frac{R_1}{D} \right)^{\ell+2} e^{-im\Phi} q_\alpha^* \left[(\ell + 1)\mathbf{n} + im\boldsymbol{\lambda} \right], \tag{2.42}$$

where $\mathbf{n}$ is the unit vector in the radial direction from star 2 to star 1 and $\boldsymbol{\lambda}$ is the unit vector in the tangential direction.

Note that Eq. (2.39) can be reduced to the limit of the equilibrium tide by taking $\dot{q}_\alpha = 0$. Substituting this into Eq. (2.42) and comparing it with Eq. (2.34), we can show that

$$\lambda_2 = \frac{R^5}{3} \sum_\alpha (W_{\ell m} I_\alpha)^2. \tag{2.43}$$

Equation (2.34) does not have the $\boldsymbol{\lambda}$ component due to the symmetry of the tidal bulge about the line connecting the binary since the bulge always points towards the companion star for equilibrium tide.

2.5 Stellar pulsations

In this section, we briefly discuss the basic setup of the linearized time-dependent perturbations of a non-rotating star that leads to the set of pulsation modes. Let us focus on the Newtonian theory here. The GR extension will be discussed briefly at the end and the details will be in Chapter 5 for anisotropic stars. The problem has been schematically written as an eigenvalue problem in Eq. (2.37). The following provides the explicit forms of the governing equations.

The equations of motion governing the motion of a mass element inside a continuum consist of the momentum conservation equation, continuity equation, and the Poisson equation:

$$\rho \frac{\partial \boldsymbol{v}}{\partial t} = \nabla \cdot \boldsymbol{\sigma} - \rho \nabla \Psi, \tag{2.44}$$

$$\frac{\partial \rho}{\partial t} = -\nabla \cdot (\rho \boldsymbol{v}), \tag{2.45}$$

$$\nabla^2 \Psi = 4\pi\rho. \tag{2.46}$$

Here $\boldsymbol{v}$ is the velocity vector of the mass element, Ψ is the gravitational potential, while $\boldsymbol{\sigma}$ is the stress tensor. For a perfect fluid,

$$\sigma_{ij} = -p\delta_{i,j}. \tag{2.47}$$

Under small perturbations, we use the Eulerian and Lagrangian perturbations to describe the small variations from the equilibrium background. The Eulerian perturbations, denoted by the prefix δ, are related to the Lagrangian perturbations, denoted by the prefix Δ, via the Lie derivative: $\Delta = \delta + \mathcal{L}_\xi$ [130].

From thermodynamics, an adiabatic perturbation of a perfect fluid follows

$$\Delta\sigma_{ij} = -\frac{\Gamma_1 p}{\rho}\Delta\rho\delta_{i,j}, \tag{2.48}$$

where Γ_1 is the (Newtonian) adiabatic index defined by $\Gamma_1 = \rho/p(\partial p/\partial\rho)_S$ for a fixed entropy.

For an isotropic solid[2] following a Hookean relation, it is given by [28, 131]

$$\Delta\sigma_{ij} = \Gamma_1 p\,\mathrm{Tr}\left(\Delta\boldsymbol{U}\right)\delta_{i,j} + 2\mu\left[\Delta U_{ij} - \frac{1}{3}\mathrm{Tr}\left(\Delta\boldsymbol{U}\right)\delta_{i,j}\right], \tag{2.49}$$

where $\Delta U_{ij} = (\partial_i\xi_j + \partial_j\xi_i)/2$ is the infinitesimal symmetric strain tensor and μ is the shear modulus of the isotropic elastic medium. Setting μ to zero reduces the Eq. (2.49) to Eq. (2.47).

Next, we assume that each mass element inside the star is oscillating about its equilibrium position so that we can decompose the displacement vector and perturbed scalar quantities as follows. The displacement vector of a mass element under spheroidal (also called polar or even parity) oscillations is given by

$$\boldsymbol{\xi} = \sum_{\ell,m}\left[\xi_r^\ell(r)\boldsymbol{e}_r + r\xi_\perp^\ell(r)\nabla\right]Y_{\ell m}(\theta,\phi)e^{i\omega t}, \tag{2.50}$$

where $\xi_r^\ell(r)$ and $\xi_\perp^\ell(r)$ are the radial and tangential displacement functions of degree ℓ respectively, while $Y_{\ell m}(\theta,\phi)$ are the spherical harmonics and ω is the angular frequency. The perturbations of the scalar quantities are also expanded in terms of the

[2] A solid with a scalar shear modulus. Not to be confused with an isotropic fluid which has no shear stress. An isotropic solid can give rise to an anisotropic stress, which is a situation discussed in Chapter 5.

spherical harmonics:

$$\delta Q(r,\theta,\phi,t) = \sum_{\ell,m} \delta Q_\ell(r) Y_{\ell m}(\theta,\phi) e^{i\omega t}, \tag{2.51}$$

where Q represents the scalar quantities ρ, p, and Ψ. From now on, we will suppress the spherical degree ℓ in the radial components of the perturbed quantities.

Substituting the perturbed quantities into Eqs. (2.44)-(2.46) and using $\boldsymbol{v} = i\omega\boldsymbol{\xi}$, we obtain the equation of motion of spheroidal pulsation modes. The formalism for both perfect fluid and isotropic solid will be provided in Appendix F.1.

The pulsation equations together with the appropriate boundary conditions form the eigenvalue problem in Eq. (2.37). Solving it gives the discrete set of pulsation frequencies and the corresponding mode functions. We solve these equations for the Newtonian pulsation modes in Chapters 4 and 7.

The stellar pulsation theory in GR is derived in the same spirit using the perturbed Einstein field equations. The perturbed metric tensor and the stress energy tensor are expanded in terms of (tensorial) spherical harmonics with the time dependence $e^{i\omega t}$. The difference is that the vacuum now permits wave-like solutions and one has to consider the propagations of metric perturbations in the stellar external. A pulsation mode in GR corresponds to a purely outgoing wave in the far-field region, which means the mode decays over time by losing energy through GW emission. The theory and formalism for the GR stellar pulsations of anisotropic stars are discussed in Chapter 5.

2.6 Gravitational wave analysis

In this section, we introduce the method to estimate the optimal signal-to-noise ratio (SNR) and the statistical error of the waveform parameters from a noisy GW signal.

2.6.1 Signal-to-noise ratio

The GW signals from astrophysical sources are often buried in noise with a much larger amplitude. Matched filtering is a common technique to identify the GW from the detector output. This involves integrating the output multiplied by a filter function. Using the Wiener filter function, the integral returns the SNR of the GW signal with the chosen filter. The maximum SNR for the optimal choice of the filter is given by [132]

$$\text{SNR} \equiv ||h|| = \sqrt{\langle h|h\rangle}, \tag{2.52}$$

where $h(t)$ is the GW signal inside the detector output. The inner product $\langle ...|...\rangle$ is defined by

$$\langle a|b\rangle = 4\,\text{Re}\int_0^\infty df \frac{\tilde{a}^*(f)\tilde{b}(f)}{S_n(f)}, \tag{2.53}$$

for any time series $a(t)$, $b(t)$. Here, the overhead tilde denotes a Fourier transform, and $S_n(f)$ is the (one-sided) noise power spectral density.

Equation (2.52) allows us to estimate the optimal SNR of a signal when it is detected with the correct waveform template.

2.6.2 Parameter estimation

The parameters of the astrophysical GW sources can be estimated by analyzing the signal. Due to the randomness of the uncontrolled factors, i.e., noise, the measurements of the parameters are best represented as a probability distribution through statistical reasoning. The two statistical approaches are known as the frequentist approach and the Bayesian approach. The former is more suitable for experiments where the parameters are well-controlled and can be repeated many times, which constructs probability distributions for the measured parameters based on the frequency of occurrence. The latter is suitable for astrophysics that rely on observations with a limited number of sources. In this approach, we use observed data to update our "degree of belief" of the parameters, represented by a probability distribution known as the "prior" [132]. Hence, the Bayesian approach is taken in GW signal analysis, as in this thesis.

The Bayesian approach is based on Baye's theorem

$$P(\theta|d) = \mathcal{N} P(\theta) P(d|\theta), \tag{2.54}$$

where $\mathcal{N}$ is the normalization constant, d is the measured data, θ is the set of parameters of the GW waveform (e.g., the masses, spins of the binary), $P(\theta)$ is the "prior": the probability distribution of θ, $P(d|\theta)$ is the "likelihood": the probability distribution of the data given the parameters, and $P(\theta|d)$ is the "posterior": the probability distribution of the parameters given the data.

In a GW measurement, the posterior corresponds to our measured distribution of the waveform parameters, while the likelihood is obtained from the measured signal. For

a colored Gaussian noise, the likelihood is given by

$$P(d|\theta) = \mathcal{N} \exp\left[-\frac{\langle n|n\rangle}{2}\right], \tag{2.55}$$

where $\mathcal{N}$ is the normalization constant, $n(t)$ is the noise and is given by $d(t) = n(t) + h(t;\theta)$, and $h(t;\theta)$ is the waveform model as a function of time with the true value of the parameters. This expression can be understood as the intersections of a continuous set of Gaussian distributions centered at $\tilde{n}(f) = 0$ with a frequency-dependent width given by $S_n(f)$.

From Eqs. (2.54) and (2.55), we can write the posterior distribution as

$$\begin{aligned} P(\theta|d) =& \mathcal{N} P(\theta) \exp\left[-\frac{\langle d - h(\theta)|d - h(\theta)\rangle}{2}\right] \\ =& \mathcal{N} P(\theta) \exp\left[\langle d|h(\theta)\rangle - \frac{\langle h(\theta)|h(\theta)\rangle}{2}\right]. \end{aligned} \tag{2.56}$$

The part involving $\langle d|d\rangle$ is absorbed into $\mathcal{N}$ in the second line. This equation allows one to find the posterior of the GW model parameters, given the prior of the parameters $P(\theta)$, the measured signal $d(t)$, and the waveform template $h(t;\theta)$. However, the set of parameters θ usually contains several parameters and the extraction of the distribution for each parameter requires a high dimensional integration. To reduce the computation cost, one can use the Fisher matrix to estimate the measurement uncertainties, if the signal-to-noise ratio is large enough.

2.6.3 Fisher matrix

The exponential function in Eq. (2.56) can be expanded about the values of θ that maximizes the likelihood function [133]:

$$\exp\left[\langle d|h(\theta)\rangle - \frac{\langle h(\theta)|h(\theta)\rangle}{2}\right] \approx \mathcal{N}\exp\left[-\frac{1}{2}\Gamma_{ij}\Delta\theta^i\Delta\theta^j\right], \tag{2.57}$$

where $\Delta\theta^i$ is the deviation of the i-th parameter from the maximum-likelihood value, Γ_{ij} is the Fisher matrix defined by

$$\begin{aligned}\Gamma_{ij} &= -\left\langle \frac{\partial^2 h}{\partial\theta^i\partial\theta^j}\middle| d-h\right\rangle + \left\langle \frac{\partial h}{\partial\theta^i}\middle|\frac{\partial h}{\partial\theta^j}\right\rangle \\ &\approx \left\langle \frac{\partial h}{\partial\theta^i}\middle|\frac{\partial h}{\partial\theta^j}\right\rangle .\end{aligned} \tag{2.58}$$

The second line holds for large SNR. The likelihood is now a multivariate Gaussian distribution. The posterior under this approximation is given by

$$P(\theta|d) = \mathcal{N}P(\theta)\exp\left(-\frac{1}{2}\Gamma_{ij}\Delta\theta^i\Delta\theta^j\right). \tag{2.59}$$

We can further define the covariance matrix

$$\Sigma^{ij} \equiv \left(\Gamma^{-1}\right)^{ij}, \tag{2.60}$$

and the correlation coefficients to quantify the correlations between different parameters:

$$C^{ij} = \frac{\Sigma^{ij}}{\sqrt{\Sigma^{ii}\Sigma^{jj}}}. \tag{2.61}$$

The diagonal element of C^{ij} is normalized to unity while the off-diagonal elements quantify the amount of correlation between two different parameters, ranging from 0 (no correlation) to ± 1 (strong correlation).

If the prior is constant, the expectation value of the measurement error can be obtained from the diagonal element of its inverse:

$$\langle \Delta\theta^i \rangle = \sqrt{(\Gamma^{-1})^{ii}} = \sqrt{\Sigma^{ii}}. \tag{2.62}$$

Note that the repeated indices here are not summed over.

If the prior is Gaussian, the width of the prior of the i-th parameter, σ_i, can be combined with the exponential term and we can define a new Fisher matrix

$$\tilde{\Gamma}_{ij} = \Gamma_{ij} + \frac{\delta_{i,j}}{\sigma_i^2}. \tag{2.63}$$

The diagonal elements of the inverse of this new Fisher matrix give the square of the error. Since these Gaussian priors allow us to estimate the error in the posterior with such a slight modification, we assume Gaussian priors in the following studies for simplicity.

This formalism using the Fisher matrix to estimate the statistical error of the GW measurements is applied in Chapter 6 on testing gravity and Chapter 7 on probing nuclear physics.

Chapter 3

Measuring tides in eccentric white dwarf binaries with gravitational waves

The major content of this chapter is based on the published article [134]. We extend previous studies on using periastron advance of a binary to measure the equilibrium tide of an eccentric DWD system with LISA [34] to include the dynamical tide effect. Our result shows that the dynamical tide becomes strong enough to produce resolvable sidebands in the GW signal in the frequency domain due to periastron advance for systems close to Roche-lobe contact. This effect can potentially be distinguished from the waveform for high-mass systems with large SNR.

In Sec. 3.2, we first derive the expression of the periastron precession based on the formalism in Sec. 2.3.2, and numerically compute the precession rate for various DWD systems. We then study how the precession affects the GW signal in Sec. 3.3.

mass $M_\odot$	radius 10^3 km	ω_α s^{-1}	I_α
0.20	14.66	0.135	0.234
0.60	8.84	0.520	0.216

Table 3.1: WD parameters obtained by solving the eigenvalue problem Eq. (2.37). The eigenfrequency and overlap integral, ω_α and I_α, of the $\ell = 2$ f-modes are listed.

3.1 White dwarf models

We begin by constructing the WD models and computing their properties under dynamical perturbations. The background model is constructed using the Newtonian formalism in Sec. 2.1 and the dynamical properties are computed using the method described in [129] and Sec. 2.4.2 (or see Appendix F.1).

In Table 3.1, we list the parameters of the WDs in this study, which are constructed using the analytic WD EOS described in Sec. 2.2.2. The important non-radial mode, known as the f-mode (see Sec. 1.4), dominates the tidal deformation at the quadrupolar order ($\ell = 2$) in such models. For simplicity, we consider only the contributions from the $\ell = 2$ f-mode in the following as the overlap integrals of other modes, e.g., the p-modes, are smaller by at least one order of magnitude.

3.2 Precession rate due to the dynamical tide

In an eccentric DWD system, the dynamical tide provides a non-Keplerian force that leads to the precession of the pericenter. Willems *et al.* [34] have studied precession in DWD systems due to equilibrium tide, rotation, and 1PN correction and have shown that detecting the various precession effects with LISA allows one to probe the interior structure of WDs (also see [135] which extends the work by considering more

detailed WD models). Unlike these factors that have a relatively simple dependence on the parameters of the WD or the orbit, the effect of dynamical tide depends on the details of the interplay between the oscillation modes and the orbital motion. In this section, we investigate the precession rate due to the dynamical tide and its effects on the GW signal.

3.2.1 The precession formula

To quantify the amount of precession caused by the tidal interaction, we can use the method of osculating orbit described in Sec. 2.3.2. The precession rate evolution is governed by Eq. (2.24). The secular change of γ over one complete radial orbit is denoted by $\Delta\gamma$.

We express the driven part of the solution of Eq. (2.39) as a Fourier series in the orbital frequency Ω. Together with the introduction of the Hansen coefficients, $X_k^{\ell,m}(e)$, defined by

$$\left(\frac{a}{D}\right)^{\ell+1} \exp\left(-im\Phi\right) = \sum_k X_k^{\ell,m}(e) \exp\left(-ik\Omega t\right), \tag{3.1}$$

we have

$$\Delta\gamma = \sum_\alpha \left(W_{\ell m} I_\alpha\right)^2 \left(\frac{R_1}{a}\right)^{\ell+1} \sum_k \left(\frac{\omega_\alpha^2}{\omega_\alpha^2 - k^2\Omega^2}\right) X_k^{\ell,m} A_k^{\ell,m}, \tag{3.2}$$

where k is the Fourier series index of the Hansen coefficients, α is a set of indices (n, ℓ, m, s) as explained in Sec. 2.4.2, and

$$A_k^{\ell,m} = \frac{2\pi}{e\sqrt{1-e^2}} \left\{ \left(\frac{\ell+1}{2} - m\right) X_k^{\ell,m-1} + \left(\frac{\ell+1}{2} + m\right) X_k^{\ell,m+1} \right.$$

$$+\frac{e}{4}\Big[\,(\ell+1-m)\,X_k^{\ell,m-2}+2(\ell+1)X_k^{\ell,m}+(\ell+1+m)\,X_k^{\ell,m+2}\Big]\Bigg\}. \tag{3.3}$$

The full tidal contribution to $\Delta\gamma$ is separated into the equilibrium component and the dynamical component, $\Delta\gamma = \Delta\gamma_{\rm eq} + \Delta\gamma_{\rm dyn}$, by decomposing the factor in the mode amplitude as

$$\left(\frac{\omega_\alpha^2}{\omega_\alpha^2 - k^2\Omega^2}\right) = 1 + \left(\frac{k^2\Omega^2}{\omega_\alpha^2 - k^2\Omega^2}\right), \tag{3.4}$$

where the first term denotes the equilibrium component and the second one is the dynamical component.

For $k\Omega$ not near ω_α, we can take the leading order of $\Delta\gamma_{\rm dyn}$, given by

$$\Delta\gamma_{\text{off-res}} = \sum_\alpha \frac{m_2}{m_1}\left(W_{\ell m} I_\alpha\right)^2 \left(\frac{R_1}{a}\right)^{2l+1} \left(\frac{\Omega}{\omega_\alpha}\right)^2 \sum_k k^2 \left(X_k^{\ell,m} A_k^{\ell,m}\right). \tag{3.5}$$

Here, we define $\Delta\gamma_{\text{off-res}}$ as the off-resonant approximation of $\Delta\gamma_{\rm dyn}$, which has a simple power law dependence on the orbital frequency as $\Omega^{16/3}$ obtained by applying the Kepler's third law of orbital motion on $1/a^5$.

3.2.2 Comparison with other factors of precession

It has been shown in [34] that the equilibrium tide contribution to the precession rate dominates at intermediate separations, while the 1PN contribution becomes important at larger separations. The equilibrium tide precession in the quadrupolar order, $\Delta\gamma_{\rm eq}$, can be written in a simple form (see, e.g., [12])

$$\Delta\gamma_{\rm eq} = 45\pi\lambda_{2,1}\frac{m_2}{m_1}\left[\frac{1}{a(1-e^2)}\right]^5 \left(1+\frac{3}{2}e^2+\frac{1}{8}e^4\right), \tag{3.6}$$

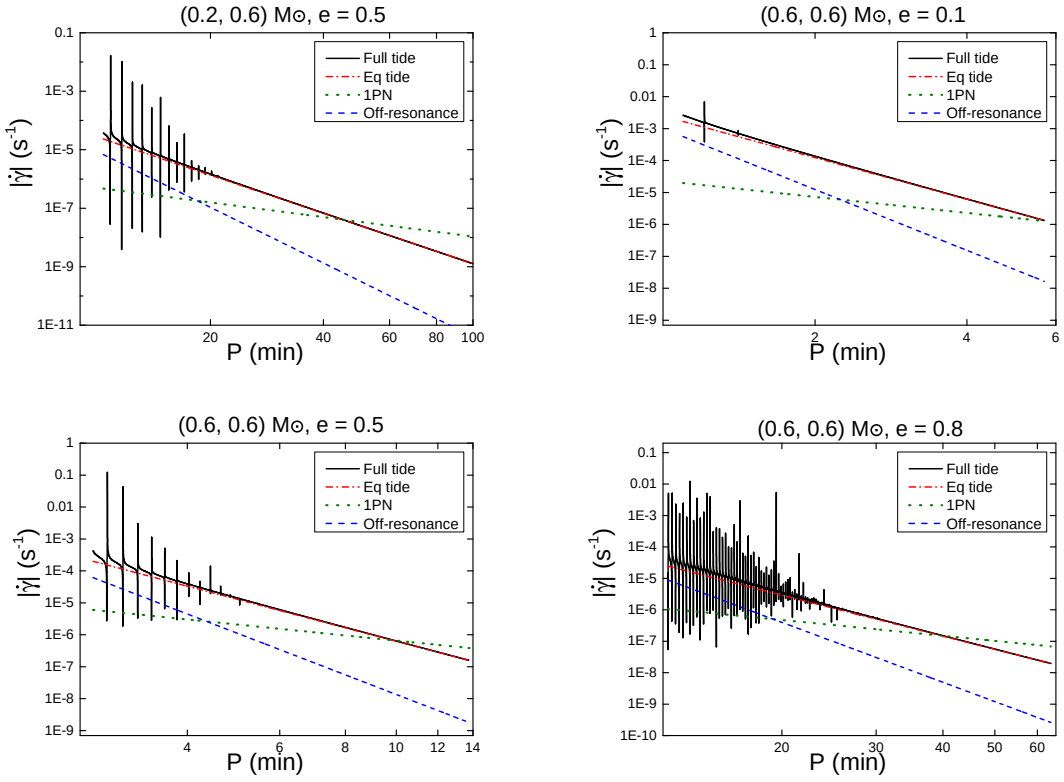

Figure 3.1: The absolute value of the precession rate of DWDs with different masses and eccentricities. The upper left panel has (0.2, 0.6) $M_\odot$ and e =0.5, and the others have (0.6, 0.6) $M_\odot$ and e =0.1, 0.5, 0.8. The full tidal contribution is given in solid black lines. The individual factors of precession include the equilibrium tide (dash-dotted red), 1PN (dotted green), and off-resonant dynamical tide (dashed blue). The smallest P corresponds to the separations where the WDs fill the Roche lobe at pericenter.

where $\lambda_{2,1}$ is the $\ell = 2$ tidal Love number of WD 1, described in Sec. 2.4.1. The 1PN precession is given by

$$\Delta\gamma_{\rm 1PN} = 6\pi \frac{m_1 + m_2}{a(1-e^2)}. \tag{3.7}$$

Both precession effects are positive, meaning they are in the same direction as the orbital motion.

In Fig. 3.1, we compare the full tidal contribution, Eq. (3.2), for the precession rate averaged over one orbit, $\dot{\gamma} \equiv \Delta\gamma/P$, with Eqs. (3.6) and (3.7) for a (0.2, 0.6) $M_\odot$ DWD system with $e = 0.5$ and (0.6, 0.6) $M_\odot$ systems with $e = 0.1, 0.5, 0.8$ at different orbital periods P. We also show the off-resonant approximation of the dynamical tide from Eq. (3.5).

The full tidal contribution is calculated using Eq. (3.2), summing up k from $-k_{max}$ to k_{max}, where the value of k_{max} is chosen to be

$$k_{max} = 16 k_{\rm peri} = 16 \ {\rm Int}\left[\frac{(1+e)^2}{(1-e^2)^{3/2}}\right], \tag{3.8}$$

where Int[...] means taking the nearest integer of the argument, and $k_{\rm peri}$ represents the harmonic corresponding to the motion closest to pericenter passage. The result shows a resonant response when the frequency of a harmonic comes close to the f-mode frequency, causing a series of narrow peaks at different P. Unlike the equilibrium tide and the 1PN effect, the precession caused by resonance can be orders of magnitude larger than the other effects and can be negative for orbits just inside the resonance. As the eccentricity increases, the resonance peaks also become more significant and cover a larger range of P. Note that even though the peaks appear only in the part with small P in Fig. 3.1, they are evenly distributed along the horizontal

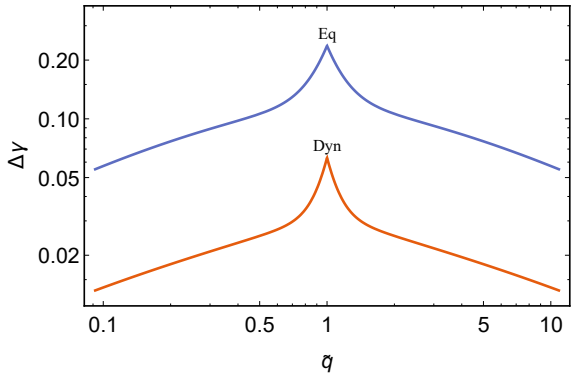

Figure 3.2: The precession angle caused by the different components of the tide of DWDs at $e \to 0$ limit with pericenter separation $r_p = a_{RL}$ with different mass ratio $\tilde{q} = m_1/m_2$. We only include the off-resonant contribution for dynamical tides.

axis. For peaks at larger P, it requires a more refined grid to show them in the plot due to the decreased width of resonance. We shall discuss these resonant effects on orbital precession in Sec. 3.2.4.

The 1PN, equilibrium tide, and the off-resonant part of the dynamical tide all contribute to positive precession of the orbit, and have power law dependence of $P^{-5/3}$, $P^{-13/3}$ and $P^{-19/3}$ respectively. As a result, the 1PN effect dominates at large separations, while the tidal contributions, mainly the equilibrium tide, become the dominant effects at small separations. The off-resonant contribution from the dynamical tide is a relatively small effect but increases rapidly when the system is close to Roche-lobe filling separation, becoming comparable to the equilibrium tide for extremely close orbits. Comparing the (0.2, 0.6) and (0.6, 0.6) $M_\odot$ cases, an increase in mass causes the tidal effect on $\dot{\gamma}$ to decrease for orbits with the same period and eccentricities. However, the more massive systems can also have closer orbits before filling the Roche lobe, which results in a larger maximum tidal effect.

3.2.3 Off-resonant contribution to precession

While the effect of resonance is enormous, it only occurs in a narrow region of the frequency space. To quantify the maximum potential of the off-resonant contribution from the dynamical tide, we explore its dependence on the orbital parameters at the $e \to 0$ limit of Eq. (3.5) that contains a small number of terms:

$$\Delta\gamma_{\text{off-res}} = 447.5 \left(\frac{m_2}{m_1}\right)\left(1+\frac{m_2}{m_1}\right)(I_\alpha)^2\left(\frac{R_1}{a}\right)^8, \tag{3.9}$$

where we have used the low eccentricity expansion of $X_k^{\ell,m}$ (see, e.g., [126]):

$$\begin{aligned} X_k^{\ell,m}(e) =& \delta_{k,m} + \frac{e}{2}[(\ell+1-2m)\delta_{k,m-1} \\ &+ (\ell+1+2m)\delta_{k,m+1}] + O(e^2), \end{aligned} \tag{3.10}$$

and we have assumed that ω_α is proportional to $\sqrt{Gm_1/R_1^3}$. We choose the proportionality constant such that $\omega_\alpha = 0.52$ s^{-1} when $m_1 = 0.6\ M_\odot$ and $R_1 = 8840$ km. The maximum possible effect from detached DWD is when a equals the Roche-lobe filling separation, a_{RL}. We employ Eggleton's formula [136] to approximate a_{RL}, which is a function of mass ratio $\tilde{q} = m_1/m_2$ and R_1. Equation (3.9) can be further simplified by relating the WD radius to the mass, which we employ the approximate relation by [137]. The overlap integral, I_α, has a weak dependence on the mass and is set to 0.2. Hence, from Eq. (2.43), $\lambda_{2,1} \approx 0.1R_1^5$.

The expressions in Eqs. (3.6) and (3.9) are plotted in Fig. 3.2 for different $\tilde{q}$ including the contributions from both WDs. The precession effect of both the dynamical tide and equilibrium tide reaches a maximum at $\tilde{q} = 1$. We see that the off-resonant dynamical tide contributes to a maximum of about 20% of the precession caused by

the overall tidal effect.

As the DWD system approaches the Roche-lobe filling separation, the dynamical tide precession starts to deviate significantly from the off-resonant approximation due to the increase in the resonance width. In the following subsection, we focus on analysing the significance of these resonance peaks.

3.2.4 The width of resonance

As the pericenter separation, r_p, gets closer to a_{RL}, the harmonics near $k_{\rm peri}$, which have large Hansen coefficients, have frequencies closer to the f-mode frequency. As a result, we expect a stronger resonance effect when the system is close to Roche-lobe filling. To quantify the significance of such an effect, we calculate the width of the resonance where the contribution from a single mode dominates the overall precession due to tides.

We rearrange the summations in Eq. (3.2) to write it as a sum of contributions from each harmonic

$$\Delta\gamma = \sum_k \Delta\gamma_k. \tag{3.11}$$

At any orbital frequency, there is one harmonic closest to the f-mode frequency, which the harmonic order is denoted by k_r. The resonance width, $\Delta\Omega_{k_r}$, is defined to be the range of frequency where the magnitude of a single mode contribution to the precession exceeds the overall equilibrium tide contribution, i.e., the region with condition $|\Delta\gamma_{k_r}| \geq \Delta\gamma_{\rm eq}$. The width-to-separation ratio of the resonance, $\Delta\Omega_{k_r}/\Delta\Omega_s$, of DWDs with different eccentricities are shown in Fig. 3.3. Here, $\Delta\Omega_s$ is the frequency difference between subsequent resonance, taken to be $\omega_\alpha/(k_r - 1)$. It shows

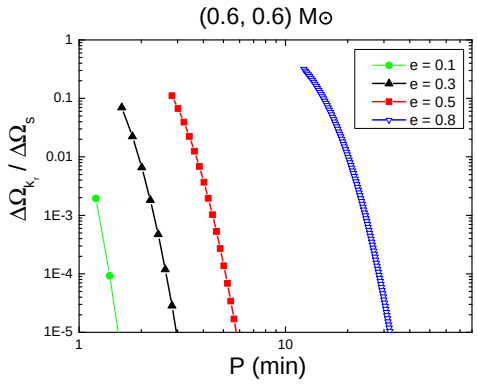

Figure 3.3: The width-to-separation ratio of the resonance of (0.6, 0.6) $M_\odot$ DWDs with different eccentricities. The smallest P of each curve corresponds to the orbital period with a harmonic in resonance right before Roche-lobe filling.

that within the more eccentric systems, the width of resonance takes about 10% of the separation between harmonics when the system is close to Roche-lobe filling separations. This ratio decays very rapidly as the orbital period increases. For systems with small eccentricities, only a few resonance peaks with the smallest P have significant width. This ratio increases with eccentricities since $\Delta\Omega_s$ scales as $(1-e)^3$, while $\Delta\Omega_{k_r}$ stays within the same order of magnitude at a fixed pericenter distance for different eccentricities.

3.2.5 The effect of spin

So far we have ignored the effect of rotation of the WD on the dynamical tide. One reason is the complexity when we include the Coriolis force, which changes the spectrum of eigenmodes [138]. Also, the angular dependence of the modes can no longer be expressed simply by a single spherical harmonic [26]. Here we want to estimate how the Coriolis force affects the results without including the full details. If we treat the effect of the Coriolis force as a small perturbation to the mode frequency

and ignore the changes to I_α, the mode amplitudes in the inertial frame have a similar expression as those in the non-rotating case:

$$q_\alpha^{(k)} = \frac{\sigma_\alpha}{\sigma_\alpha - k\Omega + m\Omega_{\rm s}} U_\alpha^{(k)}, \tag{3.12}$$

where $\Omega_{\rm s}$ is the spin rate of the WD, σ_α is the mode frequency including the correction due to Coriolis force observed in the rotating frame, which is given in the leading order of the spin rate by (see e.g., [26, 139, 140])

$$\sigma_\alpha = \omega_\alpha^{(0)} - m\Omega_{\rm s} C_{n\ell}, \tag{3.13}$$

where $\omega_\alpha^{(0)}$ is the eigenfrequency of the non-rotating WD, i.e., the quantity denoted by ω_α in previous sections and the rest of the chapter where the WD's rotation is not included, and the coefficient $C_{n\ell}$ depends on the mode eigenfunctions of the non-rotating WD. The explicit form of this coefficient can be found in e.g., [26, 139]. In this subsection, we take $C_{n\ell} = 1/\ell$ for f-modes, which can be shown to be the exact result for an incompressible star and is a good approximation for the WD models.

Including this change on the mode frequencies and amplitudes, we have the precession angle $\Delta\tilde{\gamma}_{\rm dyn}$ with spin correction given by

$$\Delta\tilde{\gamma}_{\rm dyn} = \frac{m_2}{m_1} \sum_\alpha \sum_k \left(W_{\ell m} I_\alpha\right)^2 X_k^{\ell,m} A_k^{\ell,m} \left[\frac{(k\Omega - m\Omega_{\rm s})(k\Omega - m\Omega_{\rm s} + mC_{nl}\Omega_{\rm s})}{\omega_\alpha^{(0)2} - (k\Omega - m\Omega_{\rm s} + mC_{nl}\Omega_{\rm s})^2} \right]. \tag{3.14}$$

This equation shows that the resonance frequency of the f-mode is split into the modified mode frequencies $\omega_\alpha^{(0)} + m(1 - C_{nl})\Omega_s$.

To estimate the effect of a range of rotation rates, we vary the spin from 0 to twice

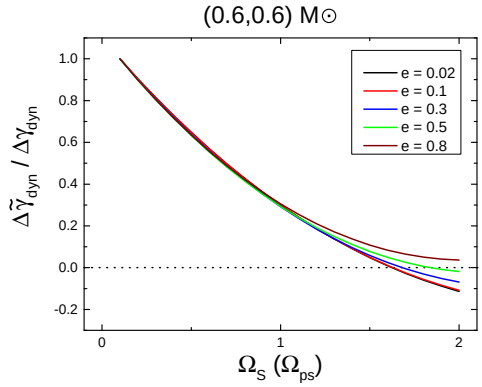

Figure 3.4: The normalized precession angle of the (0.6, 0.6) $M_\odot$ DWDs including the correction on the mode frequency due to the Coriolis effect at different spin rates. The WDs are in an orbit with $r_p = 2\ a_{RL}$. A horizontal dotted line is used to indicate $\Delta\tilde{\gamma}_{\rm dyn} = 0$.

the pseudo-synchronous value, $\Omega_{\rm ps}$, determined using the weak friction model by Hut [141],

$$\Omega_{\rm ps} = \frac{\Omega}{(1-e^2)^{3/2}}\left(\frac{16+120e^2+90e^4+5e^6}{16+48e^2+6e^4}\right). \tag{3.15}$$

This equation describes the spin rate of the WD such that there is no net torque from the equilibrium tide onto the orbit. The more general tidal synchronization problem involving dynamical tide involves the damping mechanisms of the eigenmodes and is not considered here.

In Fig. 3.4, we show the change of $\Delta\tilde{\gamma}_{\rm dyn}$ normalized by the precession angle of the non-rotating WD, $\Delta\gamma_{\rm dyn}$, when the spin rate of both of the WDs increases from 0 to 2 $\Omega_{\rm ps}$, with the pericenter separation fixed at 2 a_{RL}. As the spin rate increases, $\Delta\tilde{\gamma}_{\rm dyn}$ decreases and crosses zero at some value larger than $\Omega_{\rm ps}$ depending on the eccentricity. It shows that if the WD has a high spin rate, the dynamical tide precession is suppressed or even becomes negative. As the eccentricity increases, the $\Omega_{\rm s}$ at which $\Delta\tilde{\gamma}_{\rm dyn}$ crosses zero increases until it stays above zero when $e \gtrsim 0.8$.

The precession angle of the lower eccentricity orbits has a steeper dependence on $\Omega_{\rm s}$. We illustrate a specific example with the $e \to 0$ limit of Eq. (3.14) that contains a small number of terms, which we explicitly write down as

$$\Delta\tilde{\gamma}_{\rm dyn} = \frac{m_2}{m_1}\sum_{\alpha}(\pi I_\alpha)^2\left(\frac{R_1}{a}\right)^5\left\{\left(\frac{9}{5}\right)\frac{\Omega^2}{\omega_\alpha^{(0)2}-\Omega^2}+\left(\frac{3}{10}\right)\frac{(\Omega-2\Omega_{\rm s})[\Omega-2(1-C_{nl})\Omega_{\rm s}]}{\omega_\alpha^{(0)2}-[\Omega-2(1-C_{nl})\Omega_{\rm s}]^2}\right.$$
$$\left.-\frac{24(\Omega-\Omega_{\rm s})[\Omega-(1-C_{nl})\Omega_{\rm s}]}{\omega_\alpha^{(0)2}-4[\Omega-(1-C_{nl})\Omega_{\rm s}]^2}+\left(\frac{147}{10}\right)\frac{(3\Omega-2\Omega_{\rm s})[3\Omega-2(1-C_{nl})\Omega_{\rm s}]}{\omega_\alpha^{(0)2}-[3\Omega-2(1-C_{nl})\Omega_{\rm s}]^2}\right\}. \tag{3.16}$$

The value of $\Omega_{\rm s}$ which causes $\Delta\tilde{\gamma}_{\rm dyn}$ to become zero can be solved analytically in the off-resonant approximation. The result is independent of $\omega_\alpha^{(0)}$ and is found to be $\Omega_{\rm s} = (81-\sqrt{1041})/30\ \Omega_{\rm ps} \approx 1.62\ \Omega_{\rm ps}$, where we used $\Omega = \Omega_{\rm ps}$ when $e = 0$ from Eq. (3.15).

The centrifugal force from the rotating WDs deforms the stars and causes extra precession. Willems *et al.* [34] compared this effect with that of the 1PN and equilibrium tide. They showed that for systems close to pseudo-synchronous, it gives a precession rate with the same power law dependence on orbital separation as the equilibrium tide, but several times smaller in size. Therefore, while the Coriolis force suppresses the dynamical part of the tide, the centrifugal force gives an extra precession that enhances the equilibrium tide effect by an amount depending on the rotation rate.

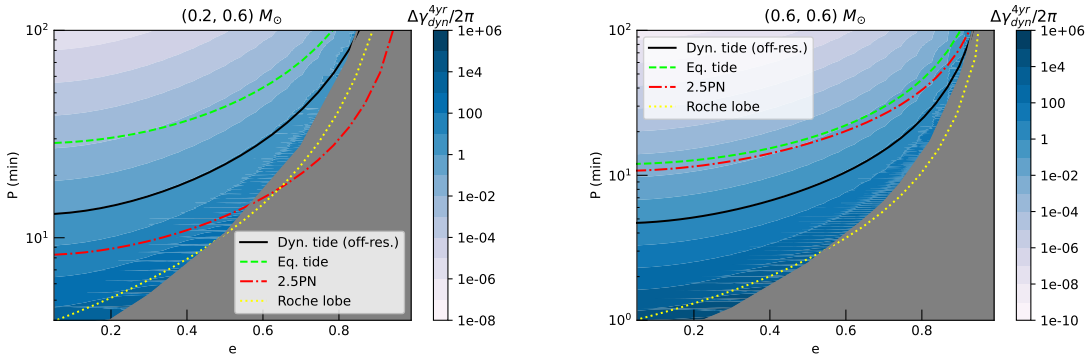

Figure 3.5: The total phase shift caused by the dynamical tide precession (including both resonant and off-resonant contributions) divided by 2π in a 4-year observation, $\Delta\gamma^{4\mathrm{yr}}_{\mathrm{dyn}}/(2\pi)$ (color contours). The maximum P for the frequency change caused by the precession from the off-resonant dynamical tide (black solid line), equilibrium tide (green dashed line), and the chirping of the 2.5PN orbital decay (red dash-dotted line) to be within the resolution of LISA are also shown. The orbital period corresponding to Roche-lobe filling separation is indicated with the yellow dotted line. The DWD systems have masses (0.2, 0.6) $M_\odot$ (left panel) and (0.6, 0.6) $M_\odot$ (right panel). The grey region indicates the parameter space for which the orbit performs chaotic motion.

3.3 The effect of precession on gravitational wave detection

3.3.1 The parameter space affected by the dynamical tide

The detection of the dynamical tide effect is limited by the resolution of LISA. A shift in phase over the observation period is resolvable if it exceeds 2π. In Fig. 3.5, we show the total phase shift (in units of 2π) caused by dynamical tide precession over 4 years within the (e, P) parameter space for a (0.2, 0.6) $M_\odot$ and a (0.6, 0.6) $M_\odot$ DWD system. The phase shift increases towards the large e and small P region. The horizontal strips appearing in the high eccentricity region correspond to the large phase shift due to resonance between a certain harmonic and the f-mode. These resonances provide a phase shift larger than 2π even for relatively large P. Note

that due to the limited resolution of the plot, the resonances appear to vanish at lower eccentricity as the resonance width decreases, even though they are expected to extend all the way to the low eccentricity region.

The maximum orbital period required for the precession caused by the equilibrium tide and the off-resonant dynamical tide to remain resolvable by LISA are represented by the green dashed line and the black solid line respectively. Similarly, the leading order effect on the frequency shift due to GW emission, i.e., the 2.5PN effect (given in [142]), is also subject to this limit and is shown with the red dash-dotted line. In the (0.2, 0.6) $M_\odot$ system, the off-resonant dynamical tide effect is resolvable for a larger range of P than the 2.5PN effect, while it is the opposite for the (0.6, 0.6) $M_\odot$ system. In both cases, the equilibrium tide effect has the largest resolvable range for all eccentricities.

The parameter space within the grey region at high eccentricities corresponds to chaotic evolution of the orbit. This phenomenon is caused by dynamical tide in highly eccentric binaries, first studied in [35] (see also [36–38]). Ivanov and Papaloizou [37] illustrate that such a chaotic behaviour due to the secular accumulation of mode energy over many pericenter passages can be understood as a kind of stochastic instability, as the mode amplitude receives a phase change at each passage which can be approximated as a uniformly distributed random variable. Here, we employ the result by [37, 38] to approximately map out the chaotic region for the DWD system, which is written as $|\omega_\alpha \Delta P| \geq 1$, with ΔP being the change in orbital period over one orbit due to the tide. In the case of (0.2, 0.6) $M_\odot$, we consider only the $|\omega_\alpha \Delta P|$ of the 0.2 $M_\odot$ WD, as it is expected to provide the dominant tidal effect inside the binary.

This region of chaotic behaviour limits the detectability of the GW signal itself in the

highly eccentric small separation regions, as the waveform is no longer predictable. In Fig. 3.6, we show the frequency domain strain signal $|h_I|$ (Eq. (B.4), see also Appendix B.1) of a system within the grey region of the (0.6, 0.6) $M_\odot$ case due to the influence of full tide and equilibrium tide respectively. The initial conditions are chosen such that the pericenter separation is 1.2 a_{RL}, and the osculating Keplerian orbit has an eccentricity of 0.82. The distance from the source is set as 10 kpc. We see that the waveform inside the chaotic region has a spread of power along the frequency domain, instead of concentrating in the vicinity of each harmonic. This behaviour completely alters the waveform, making it impossible to detect with template matching. Note that even though the waveform becomes chaotic, it still has larger amplitudes in the vicinity of the harmonics corresponding to the angular speed near the pericenter, which is similar to the periodic waveform without dynamical tides.

The orbital period corresponding to Roche-lobe filling separation is indicated with the yellow dotted line in Fig. 3.5, setting the lower bound of the orbital period of detached DWDs. This line crosses the chaotic boundary with the chaotic region covering a larger P at $e \gtrsim 0.5$. The crescent shape region in between the black solid curve and the lower bounds set by the Roche-lobe filling separation or the chaotic boundary, together with the resonant regions, represent the parameter space where the dynamical tide is resolvable by LISA.

Within these regions, the dynamical tide can have an impact on the waveform analysis, which we discuss in detail in the next subsection. However, it still requires a detailed Fisher analysis in order to quantify the actual measurability in parameter estimation. We shall leave it for future work.

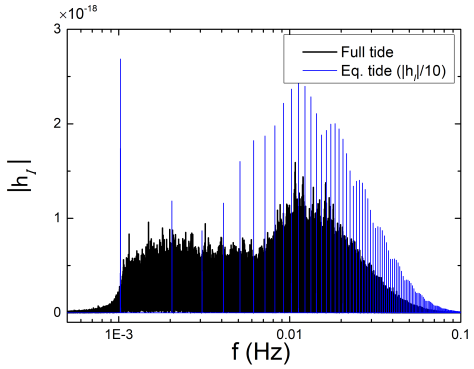

Figure 3.6: Frequency domain waveform amplitude of a (0.6, 0.6) $M_\odot$ DWD system inside the chaotic regime obtained by numerically integrating the orbital equation of motion Eq. (B.2) for a duration of 0.25 years. The initial eccentricity and pericenter distance are set to be 0.82 and 1.2 a_{RL} (P = 14.7 min) respectively (within the grey region in Fig. 3.5), and the distance is at 10 kpc. The waveform including only equilibrium tide is shown in blue lines and is rescaled by a factor of 1/10.

3.3.2 The effect of precession on waveform analysis

The waveform from the eccentric DWDs consists of a superposition of nearly monochromatic signals at every orbital harmonic, with each of them split into a triplet with frequencies $k\Omega$, $k\Omega \pm 2\dot{\gamma}$ [34, 143]. The precession rate contains the combined effects of the tide and the 1PN effect. In the following, we consider whether it is possible to separate the dynamical tide from the other factors through waveform analysis.

A useful quantity that determines the distinguishability of two waveforms h_1 and h_2 with or without the dynamical tide effect is given by

$$||\delta h|| = \sqrt{\sum_{j=I,II} \langle h_{1,j} - h_{2,j} | h_{1,j} - h_{2,j} \rangle}, \tag{3.17}$$

where $j = I, II$ is the interferometer index of LISA ([144]). The inner product $\langle ... | ... \rangle$ is introduced in Sec. 2.6.1. This quantity, $||\delta h||$, can be interpreted as the SNR of the difference between the signals. The two waveforms are said to be indistinguishable if

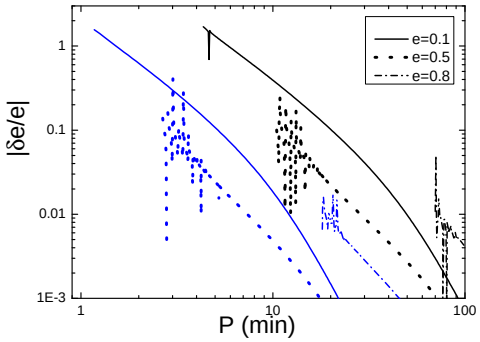

Figure 3.7: The fractional difference of the eccentricities of the two different waveform models with and without the dynamical tide effect on the precession as a function of the orbital period P. Here, we fix the precession rate and orbital frequency in the two models to determine the fractional difference in e. The DWD systems have masses (0.2, 0.6) $M_\odot$ (black lines) and (0.6, 0.6) $M_\odot$ (blue) at different P. The pericenter separation of the smallest P of each curve corresponds to the Roche-lobe filling separation, except for the $e = 0.8$ case in which the closest separation is limited by the chaotic boundary in Fig. 3.5.

$||\delta h|| < 1$ [145–147]. Here, we employ the Peters and Mathews waveform model with precession for the plus and cross polarizations [34, 142, 143, 148], whose explicit form is described in Appendix B.2. The wave amplitude of this model at each harmonic follows that of a Keplerian eccentric orbit, which is found to be a good approximation based on our preliminary calculations using the numerical waveform in Appendix B.1 for comparison. The antenna pattern acts to project the two polarizations into the detector strain signal, and is also given in Eq. (B.4).

We assume the actual signal contains the full tidal contribution as well as the 1PN effect, and compute $||\delta h||$ by using a template without the dynamical tide component to estimate the difference caused by it. The eccentricity of the template is adjusted to match the precession rate with the signal. When the chirp is small, this is expected to maximize its match with the signal.

In Fig. 3.7, we illustrate the effect of dynamical tide on the eccentricity measurement

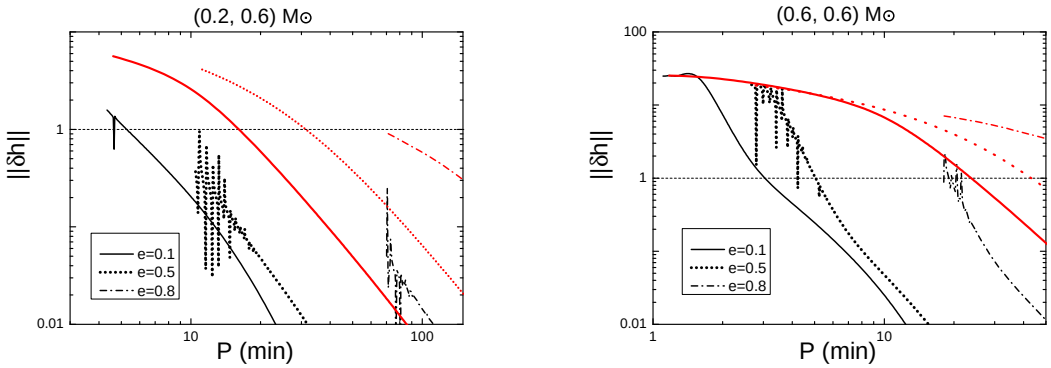

Figure 3.8: The quantity $||\delta h||$ of the (0.2, 0.6) $M_\odot$ system (left panel) and the (0.6, 0.6) $M_\odot$ system (right) in Fig. 3.7 are shown with black curves. The distance from the source, d, is taken to be 10 kpc. The observation time of the signal is set at 0.25yr. The horizontal dashed line corresponds to $||\delta h|| = 1$, the minimum value for the two signals to be distinguishable. The red curve shows $\sqrt{||h_1||^2 + ||h_2||^2}$, the estimated value of $||\delta h||$ when the waveform with full tidal contribution is at resonance and the two signals are completely mismatched.

by showing the fractional difference of the eccentricities between the precession rate models with and without the dynamical tide. We assume the model with the full tidal contribution has eccentricity e, while the other model with the equilibrium tide contribution alone has eccentricity $e + \delta e$, such that the two models have the same precession rates and orbital frequencies. The result shows that the fractional shift in the eccentricity due to not including dynamical tide can be of the size of unity for orbits with low eccentricities at closest separations. At higher eccentricities, this shift is below several percent and is insignificant even for close orbits except at resonance. This is because the off-resonant dynamical tide precession effect decreases for orbits with larger eccentricities and fixed pericenter separations. On the other hand, the near-resonant cases appear as narrow peaks and can have an order of magnitude difference in $|\delta e/e|$ from the off-resonant cases.

We show the dependence of $||\delta h||$ on P for the (0.2, 0.6) and the (0.6, 0.6) $M_\odot$ DWD

systems with different eccentricities in Fig. 3.8. For illustrative purposes, we assume the signal is observed for 0.25 years and the distance from the source is 10 kpc. The maximum SNR of the signal ranges from 0.5 to 2.5 for the (0.2, 0.6) $M_\odot$ systems and 8 to 25 for the (0.6, 0.6) $M_\odot$ systems depending on the eccentricity. We choose the observation period of 0.25 years for computational efficiency, and for a 4-year long signal, the SNR can be enhanced by a factor of 4. In both systems, $||\delta h||$ shows narrow peak features at small P near resonance. The number of peaks appearing depends on the width of the resonance and the resolution of the plot.

For orbits very close to resonance, the dynamical tide precession is much stronger than the other factors and cannot be replicated by choosing a waveform with an eccentricity within the reasonable range. The overlap between h_1 and h_2 will be small and the value of $||\delta h||$ can therefore be approximated as $\sqrt{||h_1||^2 + ||h_2||^2}$, where $||h_1||$ and $||h_2||$ are the SNRs of h_1 and h_2 with the same eccentricities respectively. We treat this as the maximum $||\delta h||$ at resonance, which are presented as red curves in Fig. 3.8. The resonance can cause the dynamical tide effect distinguishable from the other factors at a large P (>20 min for small eccentricities with this parameter choice) given a signal with large SNR. Note that $\sqrt{||h_1||^2 + ||h_2||^2}$ is an approximate upper limit when the two waveforms have small match and is not necessarily always greater than $||\delta h||$. For the $e = 0.1$ orbit of the $(0.6, 0.6)$ $M_\odot$ system at $P \approx 2$ min, $||\delta h||$ exceeds this value since $\sum_{j=I,II} \langle h_{1,j} | h_{2,j} \rangle < 0$.

Focusing on the region outside resonance, the quantity $||\delta h||$ is larger than 1 at small separations and approaches the maximum value in the case of (0.6, 0.6) $M_\odot$ but is less than 1 for most separations in the (0.2, 0.6) $M_\odot$ case, even though the fractional difference in eccentricities between h_1 and h_2 are similar (Fig. 3.7). This different behaviour of $||\delta h||$ is mainly caused by the chirp of the signal. Since the 2.5PN effect

also depends on eccentricity, measuring it helps resolve the degeneracy between the tidal effect and the eccentricity within the precession rate and allows us to identify the effect of dynamical tide[1]. This shows that LISA has the potential to identify the dynamical tide effect for high mass, eccentric DWD systems with low orbital periods, or systems with a higher harmonic close to resonance.

3.4 Chapter summary

In this chapter, we investigate the effect of dynamical tide on periastron precession of DWD binaries. We show that the dynamical tide has a strong influence on the eccentric DWD systems when they are close to the Roche-lobe filling separations, especially when the orbital motion resonates with the oscillation modes. At resonance, the dynamical tide causes a precession effect that can be orders of magnitude larger than that from the equilibrium tide alone and can become negative in some frequency range as opposed to the equilibrium tide effect and the 1PN effect that only causes the pericenter to advance. The resonance is shown to take about 10% of the frequency space within the more eccentric systems near Roche-lobe filling. On the other hand, the off-resonant approximation shows that the dynamical tide can contribute to ∼20% of the precession for the orbits with small eccentricities at close separations. We also study the effect of the WD rotations on the precession rate. The Coriolis force from the rotation of the WDs has a suppression effect on the dynamical tide precession and can also cause negative precession if the spin is high enough[2].

[1]The 3.5PN effect on the phase [149] is found to cause less than 0.01% difference in $||\delta h||$ for the (0.6, 0.6) $M_\odot$ at close separations, and hence is considered negligible in our calculations.

[2]Note that the centrifugal force induces a quadrupolar deformation of the WDs which gives extra positive precession comparable to the equilibrium tide effect when the system is at a pseudo-synchronous state, as shown in Willems *et al.* [34]. This is a separate effect from the tidal contributions studied in this chapter.

We then look into the effect of the dynamical tide precession on the GW signal. Assuming a 4-year signal duration, we show the parameter space where the dynamical tide precession is resolvable by LISA. Compared to the frequency shift due to 2.5PN radiation reaction in a (0.2, 0.6) $M_\odot$ system, this effect is resolvable within a larger range of orbital parameters. At close separations, it causes a $\gtrsim 10\%$ systematic shift in the eccentricity measurement in less eccentric systems since the precession rate depends on both the eccentricity and the tidal parameters. For the case with (0.6, 0.6) $M_\odot$, the resolvable parameter range of the 2.5PN effect is larger than that of the effect of the dynamical tide except at resonance. Hence, a stronger chirp effect is expected in systems with higher masses. The highly eccentric systems at close separations can lie within the chaotic regime, where the dynamical tide causes the orbit to evolve chaotically, a phenomenon first illustrated by Mardling [35]. This produces an unpredictable GW signal that poses problems in the detection.

Assuming a non-chaotic signal, we show that the dynamical tidal effect in the precession rate can be distinguished from other factors by analyzing the waveform if the chirp from the 2.5PN effect is strong enough, which helps constrain the eccentricity of the system, or if the system is at resonance, given a high enough SNR. Therefore, we conclude that LISA can measure the dynamical tide within high-mass eccentric DWD systems or the low-mass systems at resonance.

Regarding future work, a more detailed waveform analysis of the influence of the precession effect on the signal is required to analyze the measurement error in parameter estimation. Besides, the effect of the g-modes on the orbital motion and evolution of the eccentric DWDs can also be an interesting direction to pursue. We anticipate that the multiple harmonics in eccentric systems would lead to a richer resonance behaviour than in the circular case. This allows us to potentially probe the dissipa-

tion mechanisms and learn more about the interior structure of the WDs from the excitation and damping of the modes.

Chapter 4

An improved mapping method for the dynamical tide contributions to binary evolution

In this chapter, we discuss an improved version of an iterative mapping method used to approximate the time evolution of binary systems under the influence of dynamical tide. This formalism can be applied to eccentric DWD binaries, a potential GW source of the future space-based GW detector LISA.

The original method has been used to study tidally interacting highly eccentric systems [37, 38]. One remarkable result is that it can capture the chaotic evolution of systems with small pericenter separations due to dynamical tide. This method has made several assumptions that hold only in highly eccentric orbits. To study the orbits with moderate or low eccentricities, an improved method is required.

In the following, we first review the original iterative mapping method by [38] in Sec. 4.1. Then we discuss the newly developed method in Sec. 4.2. In Sec. 4.3, we summarize how to implement the newly developed iterative method. We leave the computation part as future work.

4.1 Original iterative mapping method

This section provides a brief review of the original iterative mapping method given by [38]. Readers only interested in the major formulas for implementing the method can skip to the summary below Eq. (4.10).

The iterative mapping method is based on discretizing the effect of the dynamical tide on the orbital evolution and updating the orbit with the overall change in one complete orbit at each pericenter passage. The formalism is derived from energy conservation

$$E_{\rm tot} = E_{\rm orb} + E_{\rm mode}, \tag{4.1}$$

where $E_{\rm tot}$ is the total energy of the system, $E_{\rm orb}$ is the gravitational binding energy of the binary, $E_{\rm mode}$ is the energy of the pulsation mode due to tidal excitation.

The term $E_{\rm orb}$ in [38] is approximated as

$$E_{\rm orb} = -\frac{m_1 m_2}{2a}, \tag{4.2}$$

which is the energy between two perfectly spherical stars and has ignored the correction due to the tidal deformation (see Sec. 4.2). The term $E_{\rm mode}$ is given by

$$\begin{aligned} E_{\rm mode} =& \frac{m_i^2}{R_i} |q_\alpha|^2 \\ =& \mathcal{B} |E_{\rm orb}| \cdot |Q_\alpha|^2 , \end{aligned} \tag{4.3}$$

where q_α is the mode amplitude given in Eq. (2.39), and Q_α is the scaled mode

amplitude, with the scaling factor:

$$\mathcal{B} = \frac{2a}{R_i}\left(\frac{m_j}{m_i}\right) W_{\ell m}^2 I_\alpha^2 \left(\frac{R_i}{a(1-e)}\right)^{2\ell+2}, \tag{4.4}$$

where the i-th star is the star with the tidally excited mode and the j-th star is the companion. We here consider only a single mode excitation with the mode indices α.

In this iterative mapping formalism, the mode amplitude is updated orbit by orbit. We therefore denote each quantity within the n-th orbit with the subscript n. When it goes from the $(n-1)$-th orbit to the n-th orbit, the mode amplitudes are related by

$$Q_{\alpha,n} = Q_{\alpha,n-1} + \Delta Q_\alpha e^{ik\pi}, \tag{4.5}$$

where the change in the (rescaled) mode amplitude, ΔQ_α, is assumed fixed in each orbit. This comes from the fact that the orbit trajectory stays almost unaltered near the pericenter even when the semi-major axis changes significantly in highly eccentric orbits [38]. The expression of ΔQ_α is given by

$$\begin{aligned}\Delta Q_\alpha =& i\omega_\alpha \int dt \left(\frac{r_p}{D}\right)^{\ell+1} e^{i\omega_\alpha t - im\Phi} \\ =& i\tilde{k}(1-e)\int_{-\pi}^{\pi} du \left(\frac{1-e}{1-e\cos u}\right)^{\ell} \cos\left[\tilde{k}(u - e\sin u) - m\Phi(u)\right],\end{aligned} \tag{4.6}$$

where r_p is the pericenter separation, Φ is the true anomaly, ΔQ_α is a function of e and $\tilde{k}$, with $\tilde{k} = \omega_\alpha/\Omega$. In the high eccentricity limit, this integral can be approximated by the parabolic limit given in [139, 150], which is the approach taken in [38]. In that case, ΔQ_α is a single variable function of $\tilde{k}$. We instead choose to parameterize it with $y = \omega_\alpha/\Omega_{\rm peri} = \tilde{k}(1-e)^{1.5}$, where $\Omega_{\rm peri}$ is the orbital frequency at periastron

passage. This parameter is more natural for nearly parabolic orbits. In principle, one can relax this approximation by computing Eq. (4.6) numerically. Note that this integral converges slowly for high eccentricities.

The mode energy is then given by

$$\Delta E_{\mathrm{mode},n} = \mathcal{B}|E_{\mathrm{orb}}| \left(|Q_{\alpha,n}|^2 - |Q_{\alpha,n-1}|^2 \right), \tag{4.7}$$

and with energy conservation, we have

$$\begin{aligned} \frac{\Delta a_n}{a_n} &= - \frac{\Delta E_{\mathrm{mode},n}}{E_{\mathrm{orb},n}} \\ &= -\mathcal{B}\left\{ 2\,\mathrm{Re}\left(\Delta Q_\alpha Q^*_{\alpha,n} e^{i\tilde{k}\pi} \right) + |\Delta Q_\alpha|^2 \right\}, \end{aligned} \tag{4.8}$$

where $a_n = a_{n-1} + \Delta a_{n-1}$.

The eccentricity is also updated iteratively under the assumption that the orbit's angular momentum remains constant:

$$a_n(1 - e_n^2) = a_{n-1}(1 - e_{n-1}^2), \tag{4.9}$$

which gives

$$\begin{aligned} \Delta e_n =& \frac{\Delta a_n}{a_n} \frac{1 - e_n^2}{2e_n} \\ =& -\mathcal{B} \frac{1 - e_n^2}{2e_n} \left[|\Delta Q_\alpha|^2 + 2\,\mathrm{Re}\left(\Delta Q_\alpha Q^*_{\alpha,n-1} e^{ik\pi} \right) \right], \end{aligned} \tag{4.10}$$

where $e_n = e_{n-1} + \Delta e_{n-1}$.

Equations (4.5), (4.6), (4.8), and (4.10) provide a method to estimate the evolution

of the orbital elements iteratively. One starts with computing the mode amplitude change, ΔQ_α, by the integral formula Eq. (4.6), and then uses it to update the values of the semi-major axis a_n, eccentricity e_n, and the mode amplitude $Q_{\alpha,n}$ for each orbit. As described below Eq. (4.6), ΔQ_α can be assumed fixed throughout the evolution in the high eccentricity limit.

4.2 Modified iterative mapping method

The influence of dynamical tide on the orbital evolution is governed by the Burns equations described in Sec. 2.3.2, i.e., Eqs. (2.22)-(2.25).

The tidal interaction force a_r and a_Φ are given in Eq. (2.42). We repeat it here to show the complete set of equations governing the orbital evolution under dynamical tide.

In principle, one can integrate Eqs. (2.22)-(2.25) numerically to determine its evolution. Nevertheless, direct integration is computationally costly and is subject to accumulation error for long evolution times. Hence, the iterative mapping method described in Sec. 4.1 provides an efficient way to approximate the solution over many orbits. To extend the iterative method to lower eccentricities, we utilize Eqs. (2.22)-(2.25) to derive an improved formalism in the following.

4.2.1 Change in semi-major axis

We first perform the variable transformation

$$\Omega t = u - e \sin u, \tag{4.11}$$

and integrate Eq. (2.22) from one pericenter to the next, while holding the other orbital elements fixed:

$$\frac{\Delta a}{a} = -\frac{\mathcal{B}}{\sqrt{1-e^2}} \int_{-\pi}^{\pi} du \left(\frac{1-e}{1-e\cos u}\right)^{\ell+1} e^{-im\Phi(u)} Q^*_\alpha(u) \times [(\ell+1)e\sin\Phi(u) + im(1+e\cos\Phi(u))] + c.c., \tag{4.12}$$

where the true anomaly and eccentric anomaly are related by

$$\tan\left(\frac{\Phi}{2}\right) = \sqrt{\frac{1+e}{1-e}} \tan\left(\frac{u}{2}\right). \tag{4.13}$$

The scaled mode amplitude $Q^*_\alpha(u)$ is obtained by integrating the equation of motion of the mode, Eq. (2.39), using the method of integrating factor

$$Q_\alpha(u) = e^{-i\omega_\alpha t(u)} \left[Q_\alpha(-\pi) e^{-i\tilde{k}\pi} + i\tilde{k}(1-e) \int_{-\pi}^{u} du' \left(\frac{1-e}{1-e\cos u'}\right)^{\ell} e^{i\omega_\alpha t(u') - im\Phi(u')} \right]. \tag{4.14}$$

Using Eqs. (4.12) and (4.14), we arrive at

$$\frac{\Delta a}{a} = -2\mathcal{B}\,\mathrm{Re}\left[\left(\Delta Q_\alpha - \Delta Q^{(\mathrm{eq})}_\alpha\right) \left(e^{i\tilde{k}\pi} Q^*_\alpha(-\pi) + \frac{\Delta Q^*_\alpha}{2} \right) \right]. \tag{4.15}$$

where

$$\Delta Q^{(\mathrm{eq})}_\alpha = \left(\frac{1-e}{1+e}\right)^{\ell+1} (-1)^m 2i \sin(\pi\tilde{k}). \tag{4.16}$$

The steps to obtain Eq. (4.15) is not trivial, as combining Eqs. (4.12) and (4.14) give us a double integral in u and u', while Eq. (4.15) only contains single integrals. In

Appendix C.1, we describe the derivation steps in detail.

Equation (4.15) is a useful result as it contains one single integral, the mode amplitude change ΔQ_α, which is obtained by numerically integrating Eq. (4.6). It does not require the numerical integration of a double integral.

We can compare Eq. (4.15) with the original method by [38], i.e., Eq. (4.8). In Eq. (4.15) there is an additional term $\Delta Q_\alpha^{(\rm eq)}$ that can be interpreted as the change in equilibrium tide amplitude evaluated at the apocenter passage. We note here that this difference comes from ignoring the tidal correction to the orbit binding energy in [38] (see Eq. (4.2) and the text below). This additional term goes as $(1-e)^{\ell+1}$ and is not important in the high eccentricity limit.

A numerical comparison of Eqs. (4.8) and (4.15) against the direct numerical integration of Eqs. (2.22)-(2.25) is provided in the left panel of Fig. 4.1. The results show that the original method agrees well with the exact results at high eccentricities $e \sim 0.9$, but starts to break down at lower eccentricities. Meanwhile, the improved method shows good agreements with the exact results even at $e = 0.3$.

4.2.2 Change in eccentricity

Similarly,

$$\Delta e = -\mathcal{B}\frac{\sqrt{1-e^2}}{2e}\int_{-\pi}^{\pi} du \left(\frac{1-e}{1-e\cos u}\right)^{\ell+1} e^{-im\Phi(u)} Q^*_\alpha(u) \times \left[(\ell+1)e\sin\Phi(u) + ime(\cos u + \cos\Phi(u))\right] + c.c. \tag{4.17}$$

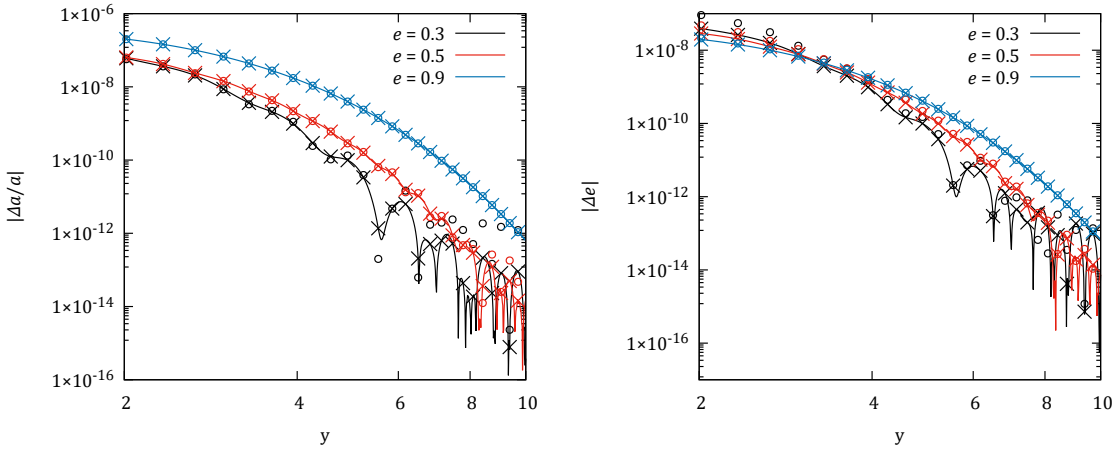

Figure 4.1: The values of $\Delta a/a$ (left panel) and Δe (right panel) computed using different methods against $y = \omega_\alpha/\Omega_{\rm peri}$ are shown for eccentricities $e = 0.3$, 0.5, and 0.9. The solid curves represent the direct integration of the Burns equations (Eqs. (2.22)-(2.25)) for one single orbit, treated as the exact results. The open circles correspond to the results from the original method that ignores the tidal interaction energy and tidal torque, and the crosses are the improved method in this work. The mode indices are $\ell = m = 2$ and the tidal overlap integral is set to 0.001 for ease of numerical integration of the Burns equations but can be scaled up easily for realistic values in the mapping methods.

Substituting Eq. (4.14) into Eq. (4.17) gives

$$\Delta e = -\mathcal{B}\frac{1-e^2}{2e}2\,\mathrm{Re}\left\{\left[\left(1-\frac{m}{\tilde{k}\sqrt{1-e^2}}\right)\Delta Q_\alpha - \Delta Q_\alpha^{(\mathrm{eq})}\right]\left[e^{i\tilde{k}\pi}Q_\alpha^*(-\pi)+\frac{\Delta Q_\alpha^*}{2}\right]\right\}. \tag{4.18}$$

The derivation procedure of Eq. (4.18) is very similar to that of Eq. (4.15), involving the parity of trigonometric functions and integration-by-part as described in Appendix C.1. One extra step is needed to deal with the term $ime\cos u$ in the square bracket of Eq. (4.17). This is done by writing it as $im(e\cos u - 1) + im$, and using it to cancel with the denominator of the first line of Eq. (4.17).

Again, Eq. (4.18) depends on the single integral ΔQ_α. We compare it with the original mapping method [38] (see Eq. (4.10)) and see that it contains the additional terms $\Delta Q_\alpha^{(\mathrm{eq})}$ and the term depending on the index m. The latter term goes as $1-e$ for a fixed pericenter distance. Therefore, Eq. (4.18) reduces to Eq. (4.10) in the high eccentricity limit.

A similar numerical comparison of the methods in calculating Δe is provided in the right panel of Fig. 4.1, verifying that the improved method works well at low eccentricities as in the case of Δa.

4.2.3 Changes in argument of pericenter and time of pericenter passage

The remaining orbital elements can also be integrated

$$\Delta\gamma = \frac{\sqrt{1-e^2}}{2e}\mathcal{B}\int_{-\pi}^{\pi} du\left(\frac{1-e}{1-e\cos u}\right)^{\ell+1} e^{-im\Phi(u)}Q_\alpha^*(u)$$

$$\times \left[(\ell+1)\cos\Phi - im\sin\Phi \left(\frac{2+e\cos\Phi}{1+e\cos\Phi} \right) \right] + c.c. \tag{4.19}$$

$$\begin{aligned}\Delta T = &- n\Delta P + \frac{\sqrt{1-e^2}}{\Omega}\Delta\gamma + \left\langle \frac{\mathcal{B}}{\Omega}\int_{-\pi}^{\pi} du \left(\frac{1-e}{1-e\cos u} \right)^{\ell+1} e^{-im\Phi(u)} Q_\alpha^*(u) \right. \\ &\times \left\{ \frac{3}{2\sqrt{1-e^2}}(u - e\sin u)\left[(\ell+1)e\sin\Phi + im(1+e\cos\Phi)\right] \right. \\ &\left. \left. - (\ell+1)(1+e)(1-e\cos u) \right\} + c.c. \right\rangle. \end{aligned} \tag{4.20}$$

The first term in Eq. (4.20) corresponds to the change in orbital period, ΔP, over n pericenter passages. It comes from the accumulative effect in the correction to T and scales with n. If we simply hold T fixed while integrating Eq. (2.25), we will miss this contribution which becomes large over many orbits. Hereafter we consider the contribution other than this term, denoted as $\Delta\mathcal{T}$:

$$\Delta\mathcal{T} = \Delta T + n\Delta P = \Delta T + n\frac{4\pi}{3}\sqrt{\frac{a}{m_1+m_2}}\Delta a. \tag{4.21}$$

For these two elements, the double integral involving the $Q_\alpha^*(u)$ term can no longer be written as the product of two single integrals with fixed integration limits.

$$\Delta\gamma = \frac{1-e^2}{2}\mathcal{B}\left(F_{\gamma 1}(e,y) Q_\alpha^*(-\pi) e^{i\tilde{k}\pi} + F_{\gamma 2}(e,y) \right) + c.c., \tag{4.22}$$

$$\Delta\mathcal{T} = \frac{\sqrt{1-e^2}}{2\Omega}\Delta\gamma + \mathcal{B}\frac{(1-e^2)^{5/2}}{\Omega}\left(F_{\mathcal{T}1}(e,y) Q_\alpha^*(-\pi) e^{i\tilde{k}\pi} + F_{\mathcal{T}2}(e,y) \right) + c.c.. \tag{4.23}$$

The functions $F_{\gamma 1}$, $F_{\gamma 2}$, $F_{\mathcal{T}1}$, and $F_{\mathcal{T}2}$ are obtained by simply substituting Eq. (4.14) into Eqs. (4.19) and (4.20). The explicit forms are given in Appendix C.2. The parameter $y = \tilde{k}(1-e)^{1.5}$ is discussed below Eq. (4.6). Since the numerical computation of these integrals for every orbit is slow, we can tabulate the integral as a two variable functions and obtain the values numerically.

4.3 The modified iterative mapping method

In this section, we summarize the method to construct the iterative algorithm to compute the orbital elements and the mode amplitude for any eccentricities. The code for the modified iterative method is still under development.

With the above expressions for ΔQ_α, Δa, Δe, $\Delta\gamma$, and ΔT, we proceed to derive the iterative formalism. Similar to Sec. 4.1, the orbital elements and the mode amplitude are discretized into the indexed values that correspond to the n-th orbit

$$\begin{aligned} Q_{\alpha,n} =& Q_{\alpha,n-1} + \Delta Q_{\alpha,n-1}, \qquad a_n = a_{n-1} + \Delta a_{n-1}, \qquad e_n = e_{n-1} + \Delta e_{n-1}, \\ \gamma_{\alpha,n} =& \gamma_{\alpha,n-1} + \Delta\gamma_{\alpha,n-1}, \qquad T_n = T_{n-1} - (n-1)\Delta P_{n-1} + \Delta\mathcal{T}_{n-1}, \end{aligned} \tag{4.24}$$

where $\Delta Q_{\alpha,n}$ is obtained Eq. (4.6), Δa_n and Δe_n can both be obtained from $\Delta Q_{\alpha,n}$ using Eqs. (4.15) and (4.18), $\Delta\gamma$ and $\Delta\mathcal{T}$ are obtained from Eqs. (4.22) and (4.23). For efficiency, the integrals ΔQ_α, $F_{\gamma 1}$, $F_{\gamma 2}$, $F_{\mathcal{T}1}$, $F_{\mathcal{T}2}$ can all be obtained through interpolation from a tabulated data file with the independent parameters e and y, where $y = \tilde{k}(1-e)^{1.5}$.

4.4 Chapter summary

To summarize, we have developed an iterative formalism to compute the orbital evolution of binary systems under the influence of dynamical tide. This method extends the formalism developed in [38] to the lower eccentricity region of the parameter space. We here point out the improvements from the previous method:

- Instead of just the semi-major axis a and the eccentricity e, the pericenter angle

γ and the time of pericenter passages T are updated in each orbit.

- The change in amplitude of the tidal deformation ΔQ_α needs to be updated in each orbit rather than staying constant.

- The change in a and e contains a contribution from the equilibrium tide component at apocenter $\Delta Q_\alpha^{(\mathrm{eq})}$ (as well as a torque component for e) that is neglected in the previous method (valid when $e \to 1$).

To construct the new method, we first look for the integral solutions to the Burns equation that governs the time evolution of the orbital elements a, e, γ, and T over a complete orbit, which corresponds to the secular change of these elements. We then use these orbital averaged changes to update the orbital elements at each pericenter passage, hence obtaining an iterative way to compute the orbital evolution for a long timescale.

We find that the secular changes Δa, Δe both have a simple dependence on the change in the (rescaled) mode amplitude ΔQ_α, a single integral over a complete orbit. Meanwhile, $\Delta\gamma$ and ΔT depend on $F_{\gamma 1}$, $F_{\gamma 2}$, $F_{\mathcal{T}1}$, $F_{\mathcal{T}2}$ beside ΔQ_α. All these integrals do not have closed-form expressions and have to be evaluated numerically. We are currently developing a code that implements the above iterative formalism by interpolation of the tabulated values of the integrals.

Chapter 5

Unstable pulsation modes of anisotropic neutron stars

This chapter focuses on the non-radial pulsation modes of NS models supported by anisotropic stress. We derive the formulation governing small oscillations of a spherically symmetric background star with anisotropy in GR and find that some of the modes are unstable. This instability does not exist in Newtonian theory or isotropic stars within GR.

In this chapter, we first describe how we construct static spherically symmetric anisotropic NS models (Sec. 5.1). Then, we describe the method we use to compute the non-radial pulsations in the anisotropic NSs (Sec. 5.2.1). We then show the numerical results in Sec. 5.3, which reveal some unexpected instabilities in the p-modes. In Sec. 5.4, we look into the p-mode instability using both a numerical analysis from Sec. 5.2.1 and an analytical approach similar to that presented in [151] for the isotropic case.

5.1 Anisotropic background models

The stress energy tensor of a spherical symmetric anisotropic NS is given by

$$T_{\alpha\beta} = \rho u_\alpha u_\beta + p_r h_{\alpha\beta} - \sigma\Omega_{\alpha\beta}, \tag{5.1}$$

where ρ is the energy density, $\sigma = p_r - p_t$ is the degree of anisotropy, p_r and p_t represent the pressures in the radial and tangential direction respectively, $h_{\alpha\beta} = g_{\alpha\beta} + u_\alpha u_\beta$ is the transverse metric on a 3D space, $\Omega_{\alpha\beta} = h_{\alpha\beta} - k_\alpha k_\beta$ is another transverse metric on a 2D sphere, u^α is the four-velocity vector of a fluid, and k^α is the unit normal vector in the radial direction orthogonal to u^α.

Note that with the typical Schwarzschild coordinates, namely (t, r, θ, ϕ), the vector k^α takes the form

$$k^\alpha = \left(k^t, k^r, 0, 0\right), \tag{5.2}$$

where k^t and k^r are determined from the orthonormality conditions:

$$k^\alpha u_\alpha = 0, \tag{5.3}$$

$$k^\alpha k_\alpha = 1. \tag{5.4}$$

In a static spherically NS model, the metric is the same as the isotropic case (see

Eq. (2.1)). The stress energy tensor in Eq. (5.1) in a static background is given by

$$T^{\alpha}{}_{\beta} = \begin{bmatrix} -\rho & 0 & 0 & 0 \\ 0 & p_r & 0 & 0 \\ 0 & 0 & p_r - \sigma & 0 \\ 0 & 0 & 0 & p_r - \sigma \end{bmatrix}. \tag{5.5}$$

The Einstein field equations of the anisotropic fluid background give (e.g., [63])

$$\nu' = 2\frac{m + 4\pi r^3 p_r}{r^2} e^{\lambda}, \tag{5.6}$$

$$p_r' = -(\rho + p_r)\frac{\nu'}{2} - \frac{2\sigma}{r}, \tag{5.7}$$

$$\lambda' = 2\frac{-m + 4\pi r^3 \rho}{r^2} e^{\lambda}, \tag{5.8}$$

$$e^{\lambda} = \left(1 - \frac{2m}{r}\right)^{-1}, \tag{5.9}$$

where the superscript prime denotes derivative with respect to r. From Eq. (5.7), we see that σ must at least go as r near the center in order for the solution to be regular (usually taken as r^2 to avoid a kink of the σ profile at the origin). The limit $\sigma \to 0$ reduces these equations back to the isotropic case (see Eqs. (2.3) to (2.6)).

5.1.1 Equations of state: Anisotropy ansatz

The anisotropy depends not only on the local variables, like the energy density, but also on the quasi-local variables, quantities that depend on the local spacetime geometry. In this study of anisotropic NS, we employ two different ansatzes for the

parameter σ:

$$\text{H-model:} \qquad \sigma = \beta p_r \mu^2, \tag{5.10}$$

$$\text{BL-model:} \qquad \sigma = \beta \frac{(\rho + p_r)(\rho + 3p_r)}{1 - \mu} r^2, \tag{5.11}$$

where $\mu = 2m/r$, m is the gravitational mass enclosed within a radius r, and β is a dimensionless parameter governing the degree of anisotropy.

The 'H-model' is modified from the model proposed by [68]. Note that compared to [68], σ here contains an extra factor of μ. Such an additional factor is introduced to satisfy the regularity conditions of the perturbations at $r = 0$ (see Sec. 5.2.2 for the expansion near the center). Due to the additional μ which is of the order ~ 0.1, we use the range $|\beta| \leq 10$ instead of $|\beta| \leq 2$ in the original model. Note that in the relativistic Cowling approximation used in [73], the original anisotropy model satisfies the regularity conditions automatically since there are no metric perturbations.

The 'BL-model' is proposed in [63], and the parameter range is taken to be $|\beta| \leq 0.5$ as in [72]. This anisotropy model permits an analytic solution to the stellar structure for incompressible stars. Unlike the H-model, we do not need to modify the BL-model as it satisfies the regularity conditions at the center.

5.1.2 Equations of state: Pressure-density relations

The relation between ρ and p_r is also provided by the EOS. We choose the polytropic EOS named 'EOS II' in [73], denoted by 'Poly' hereafter, and SLy4 [111] to demonstrate our major numerical results. With the EOSs and anisotropy ansatzes, we numerically integrate the structural equations (see, e.g., [63]) to construct the

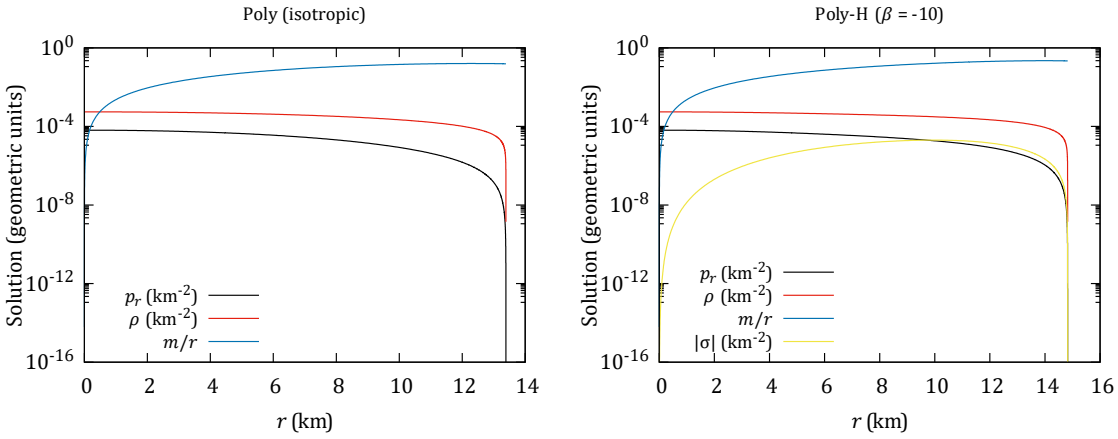

Figure 5.1: Static profiles of the isotropic Poly model and the Poly-H model with $\beta = -10$. The central densities are fixed at 7.455×10^{14}g cm^{-3} (5.539×10^{-4}km^{-2}).

anisotropic NS models at equilibrium. An example of the static background solution is shown in Fig. 5.1. We use the Poly EOS for the p_r-ρ relation with the H-model with $\beta = -10$, with the central density taken to be 7.455×10^{14} g cm^{-3} (5.539×10^{-4} km^{-2}). The absolute-valued σ profile starts from zero at the stellar center and grows to become comparable to p_r near the surface. The radial profiles of ρ, p_r, and m/r do not show significant differences, but the stellar radius differs by $\sim 10\%$.

The stress energy tensor of all models considered satisfies the dominant, weak, and strong energy conditions. Moreover, the speeds of sound in the radial and tangential directions within the stars (see, e.g., [152, 153]) both satisfy causality.

The mass-central-density relation and mass-radius relation of the Poly-H model are shown in 5.2. As the anisotropy parameter β increases towards a more positive value, the maximum mass and the corresponding radius decrease. Normally for isotropic NS, as the central density increases and passes the point of maximum mass, the star becomes radially unstable and will collapse when perturbed. This is not necessarily true for anisotropic NSs depending on the anisotropy ansatz.

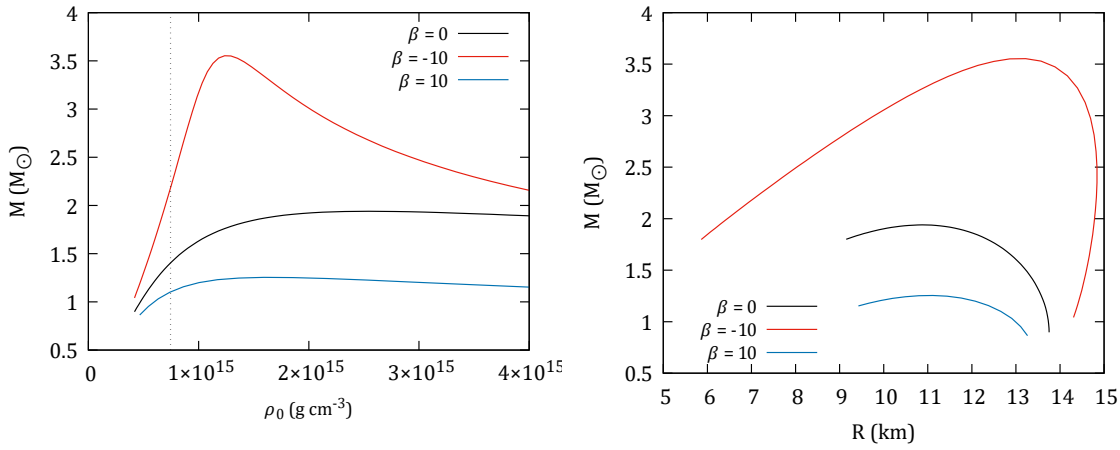

Figure 5.2: The mass-central-density relations (left panel) and mass-radius relations (right panel) of the isotropic Poly model and the Poly-H models. A vertical dotted is used to indicate the central density corresponding to 7.455×10^{14} g cm^{-3}, a fiducial value we employ in some of the following sections. This corresponds to a $1.4M_\odot$ NS when $\beta = 0$.

5.2 Solving for the non-radial modes

5.2.1 Pulsation equations and boundary conditions

Next, we consider the non-radial oscillations of anisotropic NSs. This breaks the spherical symmetry of the static background model. The oscillations are decomposed into a sum of modes on the basis formed by spherical harmonics. By focusing on the non-rotating case, each mode characterized by the spherical harmonics indices ℓ, m and an index corresponding to the radial eigenfunction, n, is decoupled from one another.

In the pulsating star, the metric and the matter dynamics are governed by the perturbed Einstein field equations and the stress-energy conservation:

$$\delta G_{\alpha\beta} = 8\pi\delta T_{\alpha\beta}, \tag{5.12}$$

$$\delta(\nabla_\alpha T^{\alpha\beta}) = 0, \tag{5.13}$$

where ∇_α denotes the covariant derivative, $G_{\alpha\beta}$ is the Einstein tensor and $T_{\alpha\beta}$ is the stress energy tensor. The prefix δ represents Eulerian perturbations and is related to the Lagrangian perturbations Δ through the Lie derivative [154], $\Delta = \delta + \mathcal{L}_\xi$, given the Lagrangian displacement vector ξ^α of the fluid.

We employ the same convention of the perturbed metric as in [40, 155], defined in the Regge-Wheeler gauge [124]:

$$\delta g_{\alpha\beta} dx^\alpha dx^\beta = -\sum_{\ell,m} \left[e^\nu r^\ell H_0 dt^2 + 2i\omega r^{\ell+1} H_1 dt dr + e^\lambda r^\ell H_2 dr^2 + r^{\ell+2} K d\Omega^2 \right] e^{i\omega t} Y_{\ell m}. \tag{5.14}$$

Here (H_0, H_1, H_2, K) are functions of r, and $Y_{\ell m}$ are the spherical harmonics. The radial parts of the expansion depend on the index ℓ, which is suppressed for conciseness in the following expressions. This applies to all the radial parts of the expansions in spherical harmonics.

The stress energy tensor takes the same form as [73]. One major assumption about the perturbed density and radial pressure is the adiabatic relation

$$\Delta p_r = \frac{\gamma p_r}{\rho + p_r} \Delta\rho, \tag{5.15}$$

where γ is the adiabatic index, and is assumed to be

$$\gamma = \frac{\rho + p_r}{p_r} \left(\frac{\partial p_r}{\partial \rho} \right)_s = \frac{\rho + p_r}{p_r} \left(\frac{\partial p_r}{\partial \rho} \right)_{\text{eq}}. \tag{5.16}$$

The subscript 's' represents an adiabatic derivative while the subscript 'eq' denotes

the derivative of the background p_r against ρ. This essentially means the EOS remains a single variable function in the dynamical timescale. The Lagrangian displacement vector is defined as

$$\xi^\alpha \partial_\alpha = \sum_{\ell,m} r^{\ell-1} e^{i\omega t} \Big[e^{-\lambda/2} W Y_{\ell m} \partial_r - \frac{V}{r} \left(\frac{\partial Y_{\ell m}}{\partial \theta} \partial_\theta + \csc^2\theta \frac{\partial Y_{\ell m}}{\partial \phi} \partial_\phi \right) \Big], \tag{5.17}$$

where V and W are functions of r.

Using Eqs. (5.12)–(5.17), we arrive at the set of equations governing the pulsations:

$$H_1' = \left[4\pi(\rho - p_r) e^\lambda r - \frac{2me^\lambda}{r^2} - \frac{\ell+1}{r} \right] H_1 + \frac{e^\lambda}{r} K + \frac{e^\lambda}{r} H_0 - \frac{16\pi(\rho+p_r)}{r} e^\lambda (1-\bar{\sigma}) V, \tag{5.18}$$

$$K' = \frac{\ell(\ell+1)}{2r} H_1 + \left(\frac{\nu'}{2} - \frac{\ell+1}{r} \right) K - 8\pi(\rho+p_r) \frac{e^{\lambda/2}}{r} W + \frac{1}{r} H_0, \tag{5.19}$$

$$W' = r e^{\lambda/2} (1-\bar{\sigma}) K + \left(-\frac{\ell+1}{r} + \frac{2\bar{\sigma}}{r} \right) W + \frac{r e^{(\lambda-\nu)/2}}{\gamma p_r} X + \frac{r e^{\lambda/2}}{2} H_0 - \frac{\ell(\ell+1)}{r} e^{\lambda/2} (1-\bar{\sigma}) V, \tag{5.20}$$

$$\begin{aligned} X' = & \frac{\rho+p_r}{2} e^{\nu/2} \left[r\omega^2 e^{-\nu} + \frac{\ell(\ell+1)}{2r} (1-2\bar{\sigma}) \right] H_1 + \frac{\rho+p_r}{2} e^{\nu/2} \Bigg[\left(\frac{3}{2} - 2\bar{\sigma} \right) \nu' \\ & - (1-6\bar{\sigma}) \frac{1}{r} - \frac{4\bar{\sigma}^2}{r} \Bigg] K - \frac{\rho+p_r}{r} e^{(\lambda+\nu)/2} \left[4\pi(\rho+p_r) + \omega^2 e^{-\nu} - F \right] W \\ & - \frac{1}{r} \left(\ell - 2\frac{\rho+p_r}{\gamma p_r} \bar{\sigma} \right) X + \frac{\rho+p_r}{2} e^{\nu/2} \left(\frac{1}{r} - \frac{\nu'}{2} \right) H_0 + \frac{\ell(\ell+1) e^{\nu/2} p_r'}{r^2} (1-\bar{\sigma}) V + \frac{2e^{\nu/2}}{r} S, \end{aligned} \tag{5.21}$$

where X is defined by $\sum_{\ell,m} r^\ell X Y_{\ell m} e^{i\omega t} = -e^{\nu/2} \Delta p_r$, the overbarred anisotropy parameter is defined by $\bar{\sigma} = \sigma/(\rho + p_r)$[1], the Eulerian perturbation of the anisotropy

[1]Note that $\bar{\sigma} \ll 1$ in the Newtonian limit.

parameter, S, is defined in

$$\sum_{\ell,m} r^{\ell} S Y_{\ell m} e^{i\omega t} = \delta\sigma, \tag{5.22}$$

and is related to other perturbation variables by

$$\begin{aligned} S =& -\left[\left(\frac{\partial\sigma}{\partial p_r}\right)_{\rm eq} + (\rho + p_r)\left(\frac{A}{p_r'} + \frac{1}{\gamma p_r}\right)\left(\frac{\partial\sigma}{\partial\rho}\right)_{\rm eq}\right]\frac{e^{-\lambda/2}p_r'}{r}W \\ &-\left[\left(\frac{\partial\sigma}{\partial p_r}\right)_{\rm eq} + \frac{\rho + p_r}{\gamma p_r}\left(\frac{\partial\sigma}{\partial\rho}\right)_{\rm eq}\right]e^{-\nu/2}X - \left(\frac{\partial\sigma}{\partial\mu}\right)_{\rm eq} e^{-\lambda}H_0, \end{aligned} \tag{5.23}$$

$$F = e^{-\lambda/2}\left\{\frac{r^2}{2}\left(\frac{e^{-\lambda/2}\nu'}{r^2}\right)' - e^{-\lambda/2}\left[\left(\frac{6}{r^2} - \frac{2\nu'}{r}\right)\bar{\sigma} - \frac{2}{r^2}\left(\frac{r\sigma'}{\rho + p_r}\right) - \frac{4}{r^2}\bar{\sigma}^2\right]\right\}. \tag{5.24}$$

Here, A is the relativistic Schwarzschild discriminant, which we take to be zero due to our assumption on γ (i.e., assuming the EOS is a single variable function of p_r), namely

$$A \equiv \frac{\rho'}{\rho + p_r} - \frac{p_r'}{\gamma p_r} = 0. \tag{5.25}$$

We further assume the partial derivatives on σ follow the equilibrium background [73], similar to the case of γ. In general, these derivatives should depend on the thermodynamic relations in the perturbation timescale [156]. The Einstein field equations also give $H_2 = H_0$ as in the isotropic case. The variables (H_0,V) are related to the dependent variables through the algebraic relations

$$\left[3m + \frac{(\ell - 1)(\ell + 2)}{2}r + 4\pi r^3 p_r\right]H_0 = 8\pi r^3 e^{-\nu/2}X - \left[\frac{\ell(\ell + 1)}{2}(m + 4\pi r^3 p_r) - \omega^2 r^3 e^{-\lambda-\nu}\right]H_1$$

$$+\left[\frac{(\ell-1)(\ell+2)}{2}r-\omega^2 r^3 e^{-\nu}-\frac{e^{\lambda}}{r}(m+4\pi r^3 p_r)(3m-r+4\pi r^3 p_r)\right]K-16\pi r e^{-\lambda/2}(\rho+p_r)\bar{\sigma}W, \tag{5.26}$$

$$X=\omega^2(\rho+p_r)e^{-\nu/2}(1-\bar{\sigma})V+\frac{\rho+p_r}{2}e^{\nu/2}H_0-\frac{p_r'}{r}e^{(\nu-\lambda)/2}W-e^{\nu/2}S. \tag{5.27}$$

To summarize how the equations are obtained, Eqs. (5.18) and (5.19) are the (t,θ)-component and the (t,r)-component of Eq. (5.12) (perturbed Einstein equations). Equation (5.20) can be obtained by combining the adiabatic relation Eq. (5.15) with the t-component of Eq. (5.13) (perturbed stress-energy conservation). An alternative way is also described in Sec. D.2. Equation (5.21) is obtained by eliminating the H_0', K' from the r-component of Eq. (5.13) using the (t,r) and (θ,r)-components of Eq. (5.12). The algebraic relation Eq. (5.26) is obtained by eliminating the H_0', K' terms with (t,r), (r,r), and (θ,r)-components of Eq. (5.12), and Eq. (5.27) is from the θ-component of Eq. (5.13). Equation (5.23) comes from the relation

$$\delta\sigma=\left(\frac{\partial\sigma}{\partial p_r}\right)_{\rm eq}\delta p_r+\left(\frac{\partial\sigma}{\partial\rho}\right)_{\rm eq}\delta\rho+\left(\frac{\partial\sigma}{\partial\mu}\right)_{\rm eq}\delta\mu. \tag{5.28}$$

See Appendix D.1 for the explicit forms of the perturbed Einstein equations and perturbed stress-energy conservation components. Also, pay attention that the perturbation variables in the appendix have been rescaled according to Eq. (D.10).

5.2.2 Solving the eigenvalue problem

To solve for the QNMs, we integrate Eqs. (5.18)–(5.21) numerically to obtain the perturbed solution of the NS interior with some trial complex frequency ω. We then continue the integration of the governing equations in the exterior region, namely Zerilli's equations [40] (also check [157] for amendments of several typos), after matching

the boundary conditions described below to a far-field region. We then match the numerical solutions with the purely outgoing condition, which is only satisfied by a discrete subset of ω's in the complex plane. To locate these eigenvalues, we employ a shooting method with the 'Mueller's method' as the root-finding scheme.

We begin the integration near the stellar center. Assuming the solutions are regular yields the following constraints:

$$H_1^{(0)} = \frac{16\pi}{\ell(\ell+1)}(\rho^{(0)} + p_r^{(0)})W^{(0)} + \frac{2}{\ell+1}K^{(0)}, \tag{5.29}$$

$$X^{(0)} = (\rho^{(0)} + p_r^{(0)})e^{\nu^{(0)}/2}\left\{\left[\frac{4\pi}{3}(\rho^{(0)} + 3p_r^{(0)}) + \frac{2\sigma^{(2)}}{\rho^{(0)} + p_r^{(0)}} - \frac{\omega^2 e^{-\nu^{(0)}}}{\ell}\right]W^{(0)} + \frac{K^{(0)}}{2}\right\}, \tag{5.30}$$

$$S^{(0)} = 0, \tag{5.31}$$

where the superscript (n) denotes the coefficient of the nth order expansion of the quantity in series of r about the stellar center. Note that in order to have a regular solution at the center, the EOS is restricted by $S^{(0)} = 0$. The second-order expansion is not necessary as long as we start the integration at a sufficiently small r. Nevertheless, we provide the explicit form of it for reference:

$$\begin{aligned} H_1^{(2)} = &\left[-\frac{\omega^2 e^{-\nu_0}}{14} + \frac{\pi}{63}(58\rho^{(0)} - 114p^{(0)}) + \frac{8\pi}{7}\frac{\sigma^{(2)}}{\omega^2 e^{-\nu_0}}\left(1 - \frac{1}{c_s^{(0)\,2}}\right)\right]K^{(0)} - \frac{48\pi}{7\omega^2 e^{-\nu_0}}S^{(2)} \\ &+ \left[-\frac{2\pi}{7}\omega^2 e^{-\nu_0} + \frac{16\pi^2}{63}(19\rho^{(0)} - 15p^{(0)}) - \frac{16\pi^2}{21}\frac{1}{c_s^{(0)\,2}}(\rho^{(0)} + 3p^{(0)})\right](\rho^{(0)} + p^{(0)})W^{(0)}, \end{aligned} \tag{5.32}$$

$$\begin{aligned} K^{(2)} = &\left[\frac{4\pi}{7}\left(\rho^{(0)} - 2p^{(0)}\right) - \frac{2\pi}{7}\frac{\left(\rho^{(0)} + p^{(0)}\right)}{c_s^{(0)\,2}} - \frac{2\omega^2 e^{-\nu_0}}{21}\right]K^{(0)} \\ &+ \omega^2 e^{-\nu_0}\left(\rho^{(0)} + p^{(0)}\right)\left(-\frac{8\pi}{21} + \frac{2\pi}{7c_s^{(0)\,2}}\right)W^{(0)}, \end{aligned} \tag{5.33}$$

$$W^{(2)} = \frac{1}{7}\left[1+\frac{1}{c_s^{(0)\,2}}+\frac{3}{\omega^2 e^{-\nu_0}}\frac{\sigma^{(2)}}{\rho^{(0)}+p^{(0)}}\left(1-\frac{1}{c_s^{(0)\,2}}\right)\right]K^{(0)} + \left[\frac{4\pi}{7}\left(2\rho^{(0)}+p^{(0)}\right)+\frac{8\pi}{21c_s^{(0)\,2}}\left(\rho^{(0)}+3p^{(0)}\right)-\frac{\omega^2 e^{-\nu_0}}{7c_s^{(0)\,2}}+\frac{\sigma^{(2)}}{\rho^{(0)}+p^{(0)}}\left(1+\frac{1}{c_s^{(0)\,2}}\right)\right]W^{(0)}, \tag{5.34}$$

$$X^{(2)} = C_1 K^{(0)} + C_2 W^{(0)} + C_3 S^{(2)}, \tag{5.35}$$

where

$$C_1 = e^{\nu_0/2}\left(\rho^{(0)}+p^{(0)}\right)\left\{\frac{\pi}{7}\left(\rho^{(0)}-7p^{(0)}\right)-\frac{\omega^2 e^{-\nu_0}}{28c_s^{(0)\,2}}-\frac{2\pi}{7c_s^{(0)\,2}}\left(\rho^{(0)}+2p^{(0)}\right) + \frac{\sigma^{(2)}}{\rho^{(0)}+p^{(0)}}\left(-\frac{4}{7}+\frac{1}{7c_s^{(0)\,2}}+\frac{4\pi}{7\omega^2 e^{-\nu_0}}\right)\left(1-\frac{1}{c_s^{(0)\,2}}\right)\left(\rho^{(0)}+3p^{(0)}\right) + \frac{6}{7\omega^2 e^{-\nu_0}}\left(\frac{\sigma^{(2)}}{\rho^{(0)}+p^{(0)}}\right)^2\left(1-\frac{1}{c_s^{(0)\,2}}\right)\right\}, \tag{5.36}$$

$$C_2 = \left(\rho^{(0)}+p^{(0)}\right)e^{\nu_0/2}\left\{\frac{40\pi^2}{63}\left[(\rho^{(0)})^2-9(p^{(0)})^2\right]-\frac{16\pi^2}{105c_s^{(0)\,2}}\left(6\rho^{(0)}+11p^{(0)}\right)\left(\rho^{(0)}+3p^{(0)}\right) - \frac{\pi\omega^2 e^{-\nu_0}}{7}\left(\rho^{(0)}-7p^{(0)}\right)+\frac{2\pi\,\omega^2 e^{-\nu_0}}{21c_s^{(0)\,2}}\left(2\rho^{(0)}+3p^{(0)}\right)+\frac{e^{-2\nu_0}\omega^4}{28c_s^{(0)\,2}} - \frac{\sigma^{(2)}}{\rho^{(0)}+p^{(0)}}\left[\frac{8\pi}{21}\left(8\rho^{(0)}-3p^{(0)}\right)+\frac{4\pi}{105c_s^{(0)\,2}}\left(\rho^{(0)}-39p^{(0)}\right)+\frac{2\omega^2 e^{-\nu_0}}{7c_s^{(0)\,2}}\right] + 2\left(\frac{\sigma^{(2)}}{\rho^{(0)}+p^{(0)}}\right)^2\left(1+\frac{1}{c_s^{(0)\,2}}\right)+\frac{2\sigma^{(4)}}{\rho^{(0)}+p^{(0)}}\right\} \tag{5.37}$$

$$C_3 = \frac{4e^{\nu_0/2}}{7}\left[2-\frac{6\pi}{\omega^2 e^{-\nu_0}}(\rho^{(0)}+3p^{(0)})-\frac{9}{\omega^2 e^{-\nu_0}}\frac{\sigma^{(2)}}{\rho^{(0)}+p^{(0)}}\right], \tag{5.38}$$

and $c_s^{(0)\,2} = \gamma p^{(0)}/(\rho^{(0)}+p^{(0)})$.

Note that Eq. (5.31) combined with Eq. (5.23) effectively places an extra constraint on σ:

$$\left(\frac{\partial\sigma}{\partial x}\right)_{\rm eq} = \mathcal{O}(r^2), \tag{5.39}$$

where x represents (p_r, ρ, μ). This is similar to how the background structure equation (Eq. (5.7)) restricts σ to go as r^2 at the center (at least r to avoid irregularity). The H anisotropy model in Eq. (5.10) is modified from the original form in [68] to satisfy the above condition.

At the surface, the vanishing Lagrangian pressure perturbation gives $X(R) = 0$. The interior solution is then matched with the metric perturbation in vacuum at the stellar surface. The exterior region is solved by Zerilli's method described in [40, 157].

5.3 Numerical results

In this section, we provide additional numerical data of the QNMs computed for the EOSs and anisotropy models shown in the main text. We demonstrate that the anisotropy has a small effect on the real part of the frequency, even though it changes the stability of the mode.

In Fig. 5.3, we show the real and imaginary parts of the QNM frequencies for the first six $\ell = 2$ modes of the Poly-H model. The real part of the frequencies of the isotropic and the anisotropic case is of similar values for all the modes. For the isotropic case, the imaginary part of the modes is all above zero and decreases with the mode order. Meanwhile, that of the anisotropic case does not show a monotonic behavior and can become negative.

We also show the frequencies obtained by the Cowling approximation in the same figure (see Appendix D.3 the procedure for reducing to this limit). The f-mode frequencies show $20-30\%$ deviations from the full GR real frequencies. The percentage deviation decreases if we go to higher radial order p-modes. In the case of the

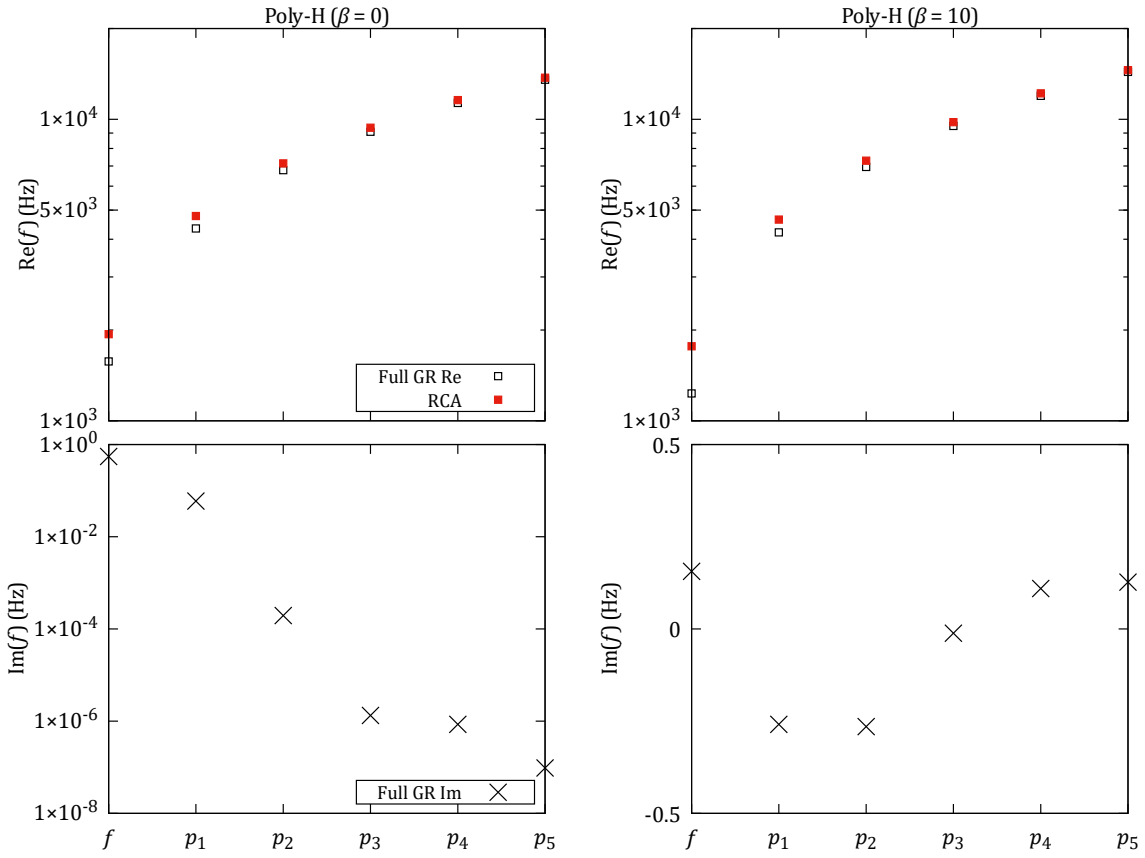

Figure 5.3: The real (top panel) and imaginary (bottom panel) frequencies of the first six $\ell = 2$ QNMs of the Poly-H model with central density 7.455×10^{14} g cm^{-3}. The left panel has $\beta = 0$ and the right panel has $\beta = 10$. We also present the normal mode frequencies computed using the relativistic Cowling approximation (RCA) described in [73].

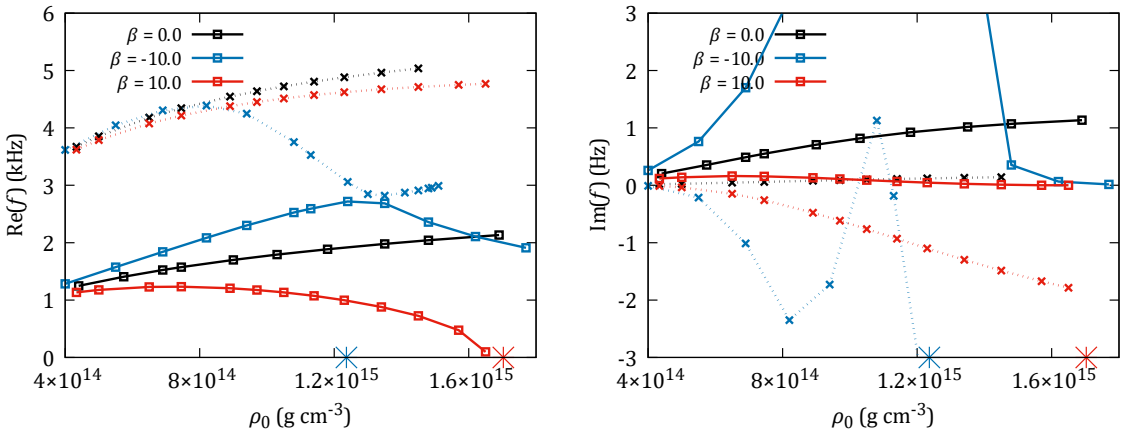

Figure 5.4: The real part (left panel) and imaginary part (right panel) of the first two $\ell = 2$ QNM frequencies of Poly-H model at different central densities. The solid lines with open squares represent the f-modes and the dotted lines with crosses are the p_1-modes. The asterisk symbols are used to indicate the central density corresponding to the maximum mass. For the $\beta = 0$ case, the central density corresponding to the maximum mass is 2.545×10^{15} g cm^{-3}, which is outside the plotting range.

p_5-modes, the deviation is down to a 1% level.

In Fig. 5.4, we further provide the $\ell = 2$ QNM frequencies of the Poly-H model at different central densities. We consider the f-modes and p_1-modes with $\beta = -10, 0, 10$. Focusing on the real part (left panel), the frequency increases with central densities in the isotropic case, while the two anisotropic cases do not show monotonic behavior. For $\beta = -10$, both the f-mode and p_1-mode real frequencies increase with central density initially and drop after a certain central density. In particular, the turning point of the f-modes encounters the minimum of the p_1-mode, which is a clear feature of avoided crossings [158]. For the imaginary part, the f-mode frequencies are all positive, with a rise initially and a steep drop after the central density passes the avoided crossing. On the other hand, the p_1-mode crosses zero and becomes negative in certain ranges of central densities.

In the case with $\beta = 10$, the real part of the f-mode and p_1-mode frequencies decrease

Table 5.1: Numerical data of the first three $\ell = 2$ QNM frequencies of the anisotropic NS models. The central densities of the Poly models and the SLy4 models are set at 7.455×10^{14}g cm^{-3} and 9.88×10^{14}g cm^{-3} respectively.

Model	β	M ($M_\odot$)	Re(ω) (kHz)			Im(ω) (Hz)		
			f	p_1	p_2	f	p_1	p_2
Poly	0	1.40	1.574	4.344	6.784	0.550	5.93×10^{-2}	1.95×10^{-4}
Poly-H	-10.0	2.18	1.945	4.364	6.104	2.262	-1.573	1.212
Poly-H	10.0	1.10	1.233	4.215	6.948	0.156	-0.259	-0.265
Poly-BL	-0.5	1.74	1.791	4.347	6.561	1.231	0.351	7.80×10^{-3}
Poly-BL	0.5	1.16	1.325	4.324	6.931	0.221	-2.01×10^{-2}	-3.59×10^{-3}
SLy4	0	1.40	1.934	6.304	9.348	0.830	3.77×10^{-2}	2.25×10^{-5}
SLy4-H	-10.0	2.52	2.527	5.715	7.672	5.561	13.24	-11.78
SLy4-H	10.0	1.06	1.322	6.147	8.877	0.129	-1.082	-0.361
SLy4-BL	-0.5	1.75	2.226	6.070	9.029	2.046	0.186	0.121
SLy4-BL	0.5	1.16	1.556	6.437	9.109	0.274	-3.90×10^{-2}	-1.24×10^{-2}

for high central density stars. Again, the p_1-mode imaginary frequency becomes negative in a wide range of central densities. The f-mode real frequency approaches zero when the star is near the maximum mass, indicated by the red asterisk symbol. The imaginary part of the f-mode stays positive but tends to decrease towards zero. This suggests that the f-mode is moving towards the origin in the complex plane as the central density increases towards the value corresponding to the maximum mass. Understanding how general this phenomenon requires more data on the QNM frequencies versus central densities with different EOSs, which is some planned future work.

More numerical data are provided in Table. 5.1, including the real and imaginary frequencies of the first three $\ell = 2$ QNMs. The $\beta = 0$ case of the SLy4 EOS has been checked against numerical data available (e.g., [159]), and attains good agreement. We see that with the same ρ–p_r relation, the real part of the frequencies is not very sensitive to the change in β, while the imaginary part can change by orders of magnitude and even change the sign.

5.4 Unstable quasinormal modes

Here we show the results of the $\ell = 2$ QNMs of anisotropic NS models where the p-mode frequencies can have a negative imaginary part for a certain range of anisotropic parameters. These modes are interpreted as unstable QNMs. We performed our calculations using two independent numerical codes and found consistent results with a difference of $\sim 1\%$.

In Fig. 5.5, we present the imaginary parts of the QNM frequencies of the f-mode, p_1-mode, and the p_2-mode against β for various combinations of the ρ–p_r EOS (Poly and SLy4) and the anisotropy EOS (H and BL models). First, we see that the f-modes all have positive imaginary frequencies. Next, the imaginary part of all modes in the isotropic limit ($\beta = 0$) is also positive, which serves as a sanity check of the numerical results, as the governing equations readily reduce to the isotropic case given in [155, 157]. As β varies away from 0, the imaginary parts of the p-modes cross zero and become negative in a certain range of β. For the p_2-modes of the Poly-H model, it even crosses zero 3 times within the range of β we consider. Similar zero-crossing behaviors are also found in higher radial order p-modes. This illustrates that there are multiple unstable p-modes within the anisotropic NSs. For a particular value of β, even the lowest order modes being stable does not necessarily mean the star is stable. In principle, one needs to solve for an infinite number of p-modes to check for stability.

We further illustrate the instability in contrast to the isotropic case, in which a smooth sequence of QNMs is forbidden to cross the real axis [151, 160]. We focus on the p_1-mode frequencies and present in Fig. 5.6 a set of anisotropic NS models with different β in the complex frequency plane. We start increasing β from the corresponding lower

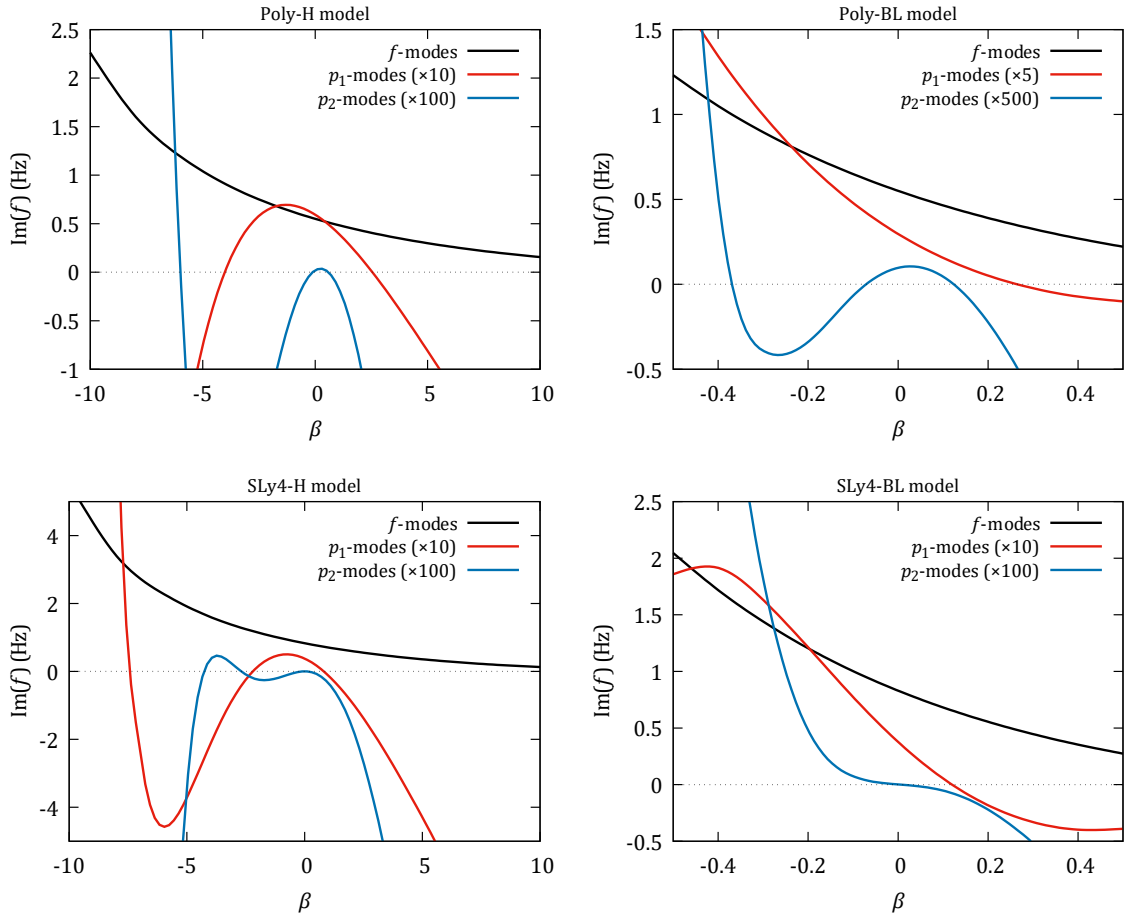

Figure 5.5: The imaginary part of the first three $\ell = 2$ QNM frequencies, $f = \omega/(2\pi)$, against the anisotropy parameter β for different combinations of the EOS (Poly vs SLy4) and the anisotropic model (H vs BL). The p-mode frequencies are scaled up by the constant factors specified in the legend to provide better visualization of the zero-crossings. The central densities of the Poly models and the SLy4 models are set at 7.455×10^{14}g cm^{-3} and 9.88×10^{14}g cm^{-3} respectively, such that the isotropic ($\beta = 0$) model has a mass of 1.40 $M_\odot$.

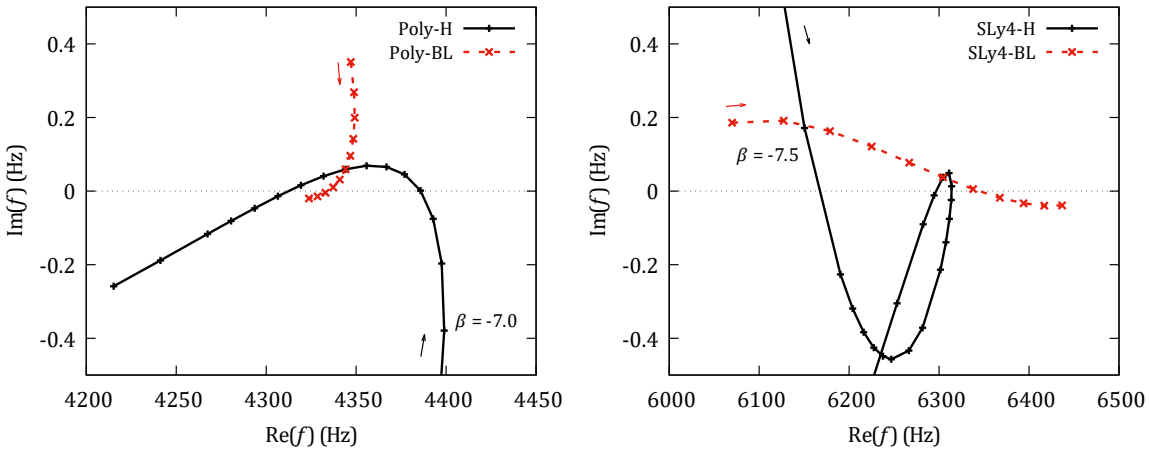

Figure 5.6: The $\ell = 2$ p_1-modes in the complex frequency plane of the models in Fig. 5.5 for Poly (left) and SLy4 (right) EOSs. The arrow indicates the direction of increasing β, in which the absolute values are chosen to be $|\beta| \leq 10$ and $|\beta| \leq 0.5$ for the H-model and the BL-model respectively. The value of β corresponding to the first point within the plotting range is shown for the SLy4-H model. Note that the curves intersect in the isotropic case (the intersection with $\mathrm{Re}(f) = 6304$Hz for the right panel).

bound value in the direction indicated by the arrow in each sequence of models. The frequency crosses the real axis for a number of times depending on the EOSs. In the case of isotropic stars, these crossings are forbidden by the equation of motion [151] as we describe in more detail in the subsequent paragraphs.

We next perform a further analytic study by following [151] that was devised for variational principle. They showed, in the isotropic case, that the QNM frequency can be related to the eigenfunctions as an integral formula consisting of pairs of the perturbation variables, schematically written in the form

$$\omega^2 \int_0^\infty I_1 dr = \int_0^\infty I_2 dr + I_3(R) + I_4(\infty), \tag{5.40}$$

where ω is the QNM frequency and I_1 to I_4 are sums of pairs of the perturbation variable eigenfunctions, which are in general complex. The term I_3 is evaluated at

the stellar radius R while I_4 is evaluated at infinity. In I_1 to I_3, the perturbation variables are expressed in complex conjugate pairs such that they are guaranteed to be real. That is, any pair of complex variables, a and b, are either paired as a^*a, b^*b, or $ab^* + a^*b$, where the asterisk sign denotes complex conjugation. For I_4, the outgoing wave condition for QNMs makes its imaginary part non-zero, except when ω is purely imaginary. As a result, ω cannot be real unless there is no outgoing wave at infinity, meaning that the QNM frequencies cannot cross the real axis in the complex frequency plane except at the origin. For the anisotropic case, we find the following extra terms on the right-hand-side of Eq. (5.40):

$$-\omega^2 \int_0^R J_1 dr + \int_0^R J_2 dr + J_3(R), \tag{5.41}$$

where J_1 and J_3 are real functions formed by paired perturbation variables similar to I_1, while J_2 is in general complex. All the terms J_1 to J_3 scale with β (see Appendix D.4 for the explicit forms of these terms). Note that the boundary term, $J_3(R)$, is zero in the anisotropy models we consider. As a result, ω^2 is allowed to cross the real axis for $\beta \neq 0$.

5.4.1 Implications of the instability

The implication of the instability still requires further analysis. We can expect the nonlinear effects will become important as the unstable mode amplitude grows exponentially with time, causing the linearized theories to eventually break down. A feedback mechanism is expected to explain the source of energy for the growth of QNMs while gravitational waves carry away the energy. This should cause some permanent changes in the stellar background and/or the anisotropy model while ex-

tracting the energy for the growth.

We can draw some insights from the Chandrasekhar-Friedman-Schutz (CFS) instability of a rotating star [130, 161], in which a QNM is seen as a prograde mode in the inertial frame, but retrograde in the co-rotating frame, thus having opposite angular momenta (see e.g., [13]). When it loses positive angular momentum through gravitational wave emission, it is driven to even larger amplitudes since the mode carries a negative angular momentum. In this case, the energy source that drives the instability comes from the rotation of the background star. Such an effect cannot be captured without considering the feedback on the background rotation.

In the setup of this study, there is no background rotation to source the growth in the mode amplitude. However, some permanent changes to the background star are expected for the mode to spontaneously increase its amplitude. One possibility is that the anisotropy will decay in a short time due to certain feedback mechanisms from the unstable mode, which can only be obtained through calculations beyond linearized perturbation theories. This may restrict the form of the anisotropy models that can be sustained in a NS.

5.5 Chapter Summary

In this chapter, we discuss the modeling of spherically symmetric NSs with anisotropic pressure. We consider the H-model modified from Horvat *et al.* [68] and the BL-model by Bowers and Liang [63] for the anisotropy parameter σ, and the Poly model [73] and SLy4 model [111] for the relation between radial pressure and energy density. With that, we can construct the static equilibrium background stars by solving the Einstein field equations.

Then, we proceed to consider the non-radial time-dependent perturbations of the background models. We first provide a formulation derived from the perturbed Einstein field equations and perturbed stress-energy conservation that is consistent with the existing formulas in the Cowling limit in [73]. We numerically solve the equations and discover a new instability in the QNMs found within some anisotropic models: the p-mode frequencies with a negative imaginary part. This means that the amplitude of those modes grows over time, while they are dissipating energy via the emission of GWs.

We next look into the unstable p-modes by considering the integral relation between the eigenfrequencies and the eigenfunctions, which we derive based on the isotropic case in [151]. We demonstrate that while the integral relation suggests that these pulsating unstable QNMs cannot exist in the isotropic case, they are allowed when there is non-zero anisotropy.

An extension of this study is to derive the feedback mechanism associated with the growth of the mode on the background quantities. We anticipate that the background has to evolve as energy is taken to cause the pulsation mode to grow. This requires us to find the work used to drive the instability, which is expected to be derived from a variational principle beginning with perturbing the integral formula relating the eigenfunctions and eigenfrequencies [151] (i.e., Eqs. (5.40) and (5.41)).

Another future direction is to study a wider variety of anisotropic models to assess the stability of the f-modes. So far in our models, the f-modes are always stable for all β. It is worth exploring whether there are any underlying reasons that this mode cannot have a negative imaginary frequency. Or if it is simply because our models do not cover enough parameter range.

Chapter 6

Testing gravity with white dwarf binaries

This chapter discusses the prospects of testing gravity theory with DWD binaries within the Milky Way with LISA. GW signals from galactic DWDs have the potential to place stringent bounds on certain theories that deviate from GR in less compact binaries, such as through scalar radiation. Nevertheless, the orbital evolution of these systems is also affected by various astrophysical effects, such as self-rotations, tidal interactions, and magnetic interactions, which add complexity to the gravity tests. In this work, we employ the parametrized post-Einsteinian (ppE) model to capture the leading beyond-GR effect on the signal and estimate the measurement uncertainties using the Fisher information matrix. We then focus on the astrophysical effects that can be confused with the deviation from predictions due to alternative gravity theories. These effects include the tidal deformation, and the spin of the WDs, as well as the magnetic field. We demonstrate that if these astrophysical effects are not properly modeled, they will cause significant systematic errors in our measurements and affect the ability to constrain alternative theories.

In the following, we first discuss the various factors that can affect the orbital evolution of DWD systems in Sec. 6.1. We also introduce the ppE model for the non-GR effects on the orbital phase evolution. Next, we go through the method we construct the

GW waveforms and analysis the measurement error in Sec. 6.2. Lastly, we apply the analysis with the ppE model on the specific class of non-GR theory known as screened modified gravity in Sec. 6.3.

6.1 Factors affecting orbital evolution

The theory of GR predicts the orbital frequency of a binary system evolves at the 2.5PN order in the leading order, effectively meaning that the effective orbital interaction force has a dependence of $D^{-4.5}$ ($D^{-2.5}$ higher than the Newtonian gravitational force for point masses), where D is the orbital separation. Deviations from GR can cause the orbital evolution rate to differ from the GR predictions and can be captured by the change of frequency in the GW signal. One can then measure the non-GR effects from the signal.

The GW frequency evolves over time due to various factors. In detached DWD systems, GR predicts that the leading point-mass contribution to the radiation reaction effect goes as

$$\dot{f}_{\rm GR} = \frac{96}{5\pi\mathcal{M}^2}\nu^{11/2}, \tag{6.1}$$

$$\ddot{f}_{\rm GR} = \frac{33792}{25\pi\mathcal{M}^3}\nu^{19/2}, \tag{6.2}$$

where $\mathcal{M} = (m_1 m_2)^{3/5}/(m1 + m_2)^{1/5}$ is the chirp mass, and $\nu = (\pi\mathcal{M}f_0)^{2/3}$ is the PN parameter proportional to the square of the ratio between the relative velocity of a binary and the speed of light. The GW frequency f_0 is taken to be the initial value at the start of the observation.

For theories beyond GR, the frequency evolves at a different rate. Testing GR involves

treating GR as the "null hypothesis" and looking for deviations from its predictions. The ppE waveform is used to model the deviations due to the leading non-GR effect. In this model, we write the (initial) time derivatives of the GW frequency as

$$\dot{f}_0 = \dot{f}_{\rm GR}(1+\gamma\nu^n), \tag{6.3}$$

$$\ddot{f}_0 = \ddot{f}_{\rm GR}\left[1+\left(1+\frac{2n}{11}\right)\gamma\nu^n\right], \tag{6.4}$$

where γ is a dimensionless parameter that characterizes the magnitude of the non-GR effect, and n is the post-Newtonian (PN) order relative to the GR effect. The relation between γ and the ppE parameter β entering in the gravitational wave phase is given by Eq. (20) of [162] while the expressions for β in example non-GR theories can be found in Table I of [162].

As mentioned above, the astrophysical effects also contribute to the frequency evolution. Up to the leading order of each astrophysical effect, the true waveform would then have the derivatives of the initial frequency

$$\dot{f}_0^{(\rm tr)} = \dot{f}_{\rm GR}(1+\gamma\nu^n+\Delta), \tag{6.5}$$

$$\ddot{f}_0^{(\rm tr)} = \ddot{f}_{\rm GR}\left[1+\left(1+\frac{2n}{11}\right)\gamma\nu^n+\left(1+\frac{2k}{11}\right)\Delta\right], \tag{6.6}$$

where Δ denote the astrophysical contributions as described below, and k is the PN order of Δ with respect to the point-mass contribution, namely $\Delta \propto \nu^k$. We describe below several examples of the astrophysical effects.

1. *moment of inertia*:

   The rotation of the WDs can affect the frequency evolution by providing a channel for orbital energy to dissipate as rotational energy. Following [163],

assuming that the binary remains synchronous, this effect is given by

$$\Delta_I = \frac{3I}{\mathcal{M}^3}\nu^2, \tag{6.7}$$

where $I = I_1 + I_2$, is the sum of the moment of inertia of the two WDs, estimated using Eq. (23) in [164], which provides a fit of the moment of inertia factor as a function of the mass of the cold WDs. This contributes to a 2PN correction to the frequency evolution.

2. *quadrupole moment*:

For DWD systems with synchronized spins, the spin-induced quadrupole moment Q_s can be shown to contribute at 5PN order [76, 163] [1]:

$$\Delta_{Q_s} = \frac{8\alpha\eta^{2/5}}{\mathcal{M}^4}\nu^5, \tag{6.8}$$

where $\eta = m_1 m_2/(m_1+m_2)^2$, $\alpha = (Q_{s1}/m_1 + Q_{s2}/m_2)/(\pi f_0)^2$. Through the I-Q_s universal relation (originally discovered for neutron stars [165–167]) for WDs [168], it can be written as

$$\bar{Q}_{s,i} = a\bar{I}_i^b, \tag{6.9}$$

where $\bar{Q}_{s,i} = m_i Q_{s,i}/(\pi I_i f_0)^2$ and $\bar{I}_i = I_i/m_i^3$ for $i = 1, 2$, and $a = 5.255$, $b = 0.4982$. The constants a and b are determined by fitting the numerical values of I_i and $Q_{s,i}$ of a set of cold WD models within the Newtonian framework. The formalism for determining $Q_{s,i}$ follows [168, 169].

[1] The numerical factor here differs from these references as Q_s is assumed to be constant, while it goes as Ω^2 in our derivation under the assumption that the spin remains synchronous all time, where Ω is the orbital frequency.

3. *tidal deformability*:

Another astrophysical contribution comes from the tidal deformation of the WDs. Similar to the spin-induced quadrupole moment, the tidally induced quadrupole moment provides an extra sink of orbital energy to dissipate into, causing a 5PN correction as derived in [170, 171]:

$$\Delta_\Lambda = \frac{39\tilde{\Lambda}}{8\eta^2}\nu^5, \tag{6.10}$$

where $\tilde{\Lambda}$ is a weighted average of the individual tidal deformability defined as [11]

$$\begin{aligned}\tilde{\Lambda} =& \frac{8}{13}\Big[[(1+7\eta-31\eta^2)(\Lambda_1+\Lambda_2) \\ &+ \sqrt{1-4\eta}(1+9\eta-11\eta^2)(\Lambda_1-\Lambda_2)\Big],\end{aligned} \tag{6.11}$$

and $\Lambda_i = \lambda_i/m_i^5$, with $i = 1, 2$, are the dimensionless tidal deformability of the WDs. The tidal deformability λ_i serves as the proportionality constant of the linear relation between the tidally induced quadrupole moment and the external tidal field from its binary companion (see Sec. 2.4.1). Note that the tidal effect enters at the same PN order as the spin-induced quadrupole moment due to the assumption that both WDs are synchronized. The tidal deformability parameter also enjoys EOS-independent relations with the moment of inertia and the spin-induced quadrupole moment [168].

4. *magnetic field*:

The magnetic dipole interaction between magnetized WDs also induces a change in the orbital decay rate through the magnetic force and the electromagnetic

radiation [172, 173]. The effect enters at 2PN order, assuming the two WDs are bare magnetic dipoles. However, in a realistic situation, the plasma around the WDs will form a magnetosphere under the magnetic field, and the interaction between the magnetic dipole moment and the magnetosphere will play an important role. Assuming the presence of the magnetosphere, the binary system can form a close electric circuit with finite resistivity. This effect can be described by the DC circuit model, which was first introduced to describe the magnetic interaction between Jupiter and its satellite Io [174] and has been applied to various binary systems including DWDs and neutron star binaries.

To briefly describe the model, an electromotive force is generated by the orbital motion of the WDs within the magnetosphere and drives a DC current in the system. The orbital energy is dissipated through the resistivity within the circuit. Assuming WD1 is magnetized with a surface magnetic field B_1, the model gives [77]

$$\Delta_B = \frac{5}{64}\eta\zeta_\phi \frac{\Delta\Omega}{\Omega}\frac{\mu_1^2 R_2^2}{\mathcal{M}^6}\nu^{3/2}, \tag{6.12}$$

where ζ_ϕ is the azimuthal twist parameter, ranging from 0 to 1, Ω is the orbital frequency, $\Delta\Omega$ is the difference between the spin frequency and the orbital frequency, and the magnetic moment follows $\mu_1 = B_1 R_1^3$ with R_A representing the radius of the Ath WD. The above effect enters at 1.5PN order.

The above effects enter at different PN orders and therefore scale differently with the frequency of the source. In Fig. 6.1, we show the sizes of these effects for two DWD systems of masses $(0.6, 0.2)M_\odot$ and $(0.4, 0.4)M_\odot$. Among Δ_I, Δ_Λ, Δ_{Q_s}, the moment-of-inertia effect dominates at low frequency due to its 2PN dependence, while

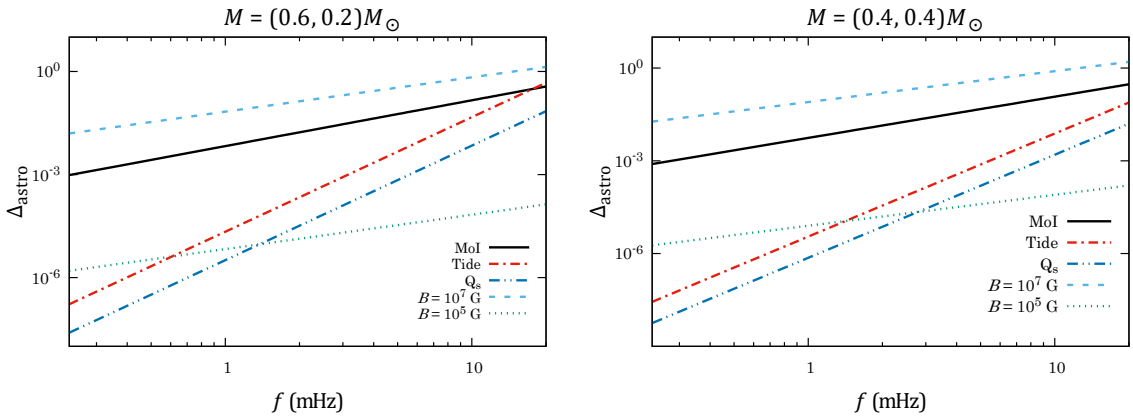

Figure 6.1: Fractional difference of astrophysical effects relative to the point-particle contribution on the frequency evolution rate against the gravitational wave frequency of DWD systems of masses $(0.6,\ 0.2)M_\odot$ (left) and $(0.4,\ 0.4)M_\odot$ (right) respectively. The effects from moment of inertia (MoI), tidal deformation (Tide), spin-induced quadrupole moment (Q_s), and magnetic field ($B = 10^5, 10^7$G) are included.

the tidal effect becomes more important for very close orbits. The effect from spin-induced quadrupole moment has the same power law dependence as the tidal effect but is about an order of magnitude smaller. The dissipative effect from unipolar induction enters at 1.5PN order and has a B_1^2 dependence. For WDs with a strong magnetic field above 10^5G, it is comparable to or even exceeds that of the rotation effect. In Fig. 6.1, we also illustrate the potential of this effect in the strong field case with $B_1 = 10^7$G. The parameters $\Delta\Omega/\Omega$ and ζ_ϕ are both taken to be 1, denoting maximal asynchronous rate and twist. As discussed in [77] and references therein, $\zeta_\phi \gtrsim 1$ would cause the flux tube connecting the circuit to break up. This leads to more complicated situations that are beyond the scope of this study.

Other possible astrophysical effects include the disturbance due to the external bodies, e.g., the Kozai-Lidov oscillations [175, 176] in a hierarchical triple system, or mass transfer between the binary [137, 164, 177]. The former can affect the orbital elements other than the orbital decay rate, like the eccentricity and inclination, and the latter

has a significant impact on the orbital evolution and may cause an out-spiral. Other than that, GR contributions to the orbital motion, like the 1PN effect or the spin-spin interaction [178], can also lead to deviations from $\dot{f}_{\rm GR}$. These effects have a different origin from the astrophysical effects mentioned above but can still cause a systematic error if not properly included. However, these effects are not expected to play an important role except for very massive WDs [170]. For simplicity, we ignore these effects.

6.2 Parameter inference

In this section, we quantify the statistical error caused by the detector noise on the measurement of the non-GR parameter of the ppE model, γ, as well as the systematic error due to astrophysical mismodeling of the waveform. We use a Fisher analysis that has been proven to agree well with results from Bayesian Markov-chain Monte-Carlo analyses for tests of GR with DWDs [74].

6.2.1 Statistical error

We start by introducing the time-domain waveform model for quasi-monochromatic sources. The strain of the nearly monochromatic GW signal from DWD systems can be described as

$$h(t) = \mathcal{A}(t)\cos\Phi(t), \tag{6.13}$$

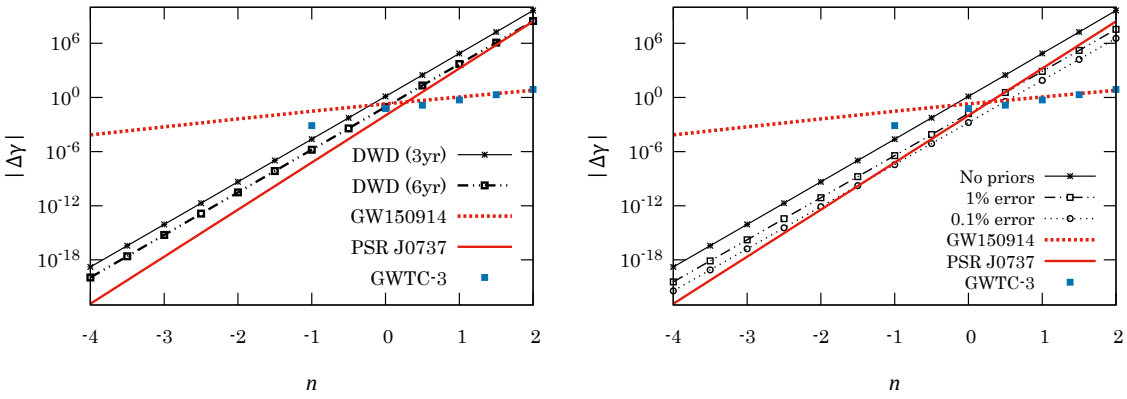

Figure 6.2: (Left) Statistical error on γ for non-GR effects at different PN order n in the ppE waveform model using the DWD listed in the first row of Table E.1. For comparison, we also present constraints set by the binary BH coalescence event GW150914, the double pulsar binary PSR J0737-3039, and the GWTC-3 data. (Right) Similar to the left panel but with different priors on the mass estimate for a 3-year observation.

where $\mathcal{A}(t)$ and $\Phi(t)$ are given by

$$\mathcal{A}(t) = \sqrt{(F_+(t)A_+)^2 + (F_\times(t)A_\times)^2}, \tag{6.14}$$

$$\Phi(t) = \Phi_{\rm LISA}(t) + \phi_0 + 2\pi f_0 t + \pi \dot{f}_0 t^2 + \pi \ddot{f}_0 t^3/3, \tag{6.15}$$

$$\Phi_{\rm LISA}(t) = \Phi_D(t) + \Phi_P(t), \tag{6.16}$$

where $F_+(t)$, $F_\times(t)$ are the LISA antenna pattern functions (see, e.g., [179], for the explicit form) while ϕ_0 and f_0 are the phase and frequency at $t = 0$. The plus- and cross-polarization amplitudes are $A_+ = A_0(1+\cos^2\iota)/2$, $A_\times = A_0\cos\iota$, where ι is the inclination angle while $A_0 = 4\mathcal{M}^{5/3}(\pi f_0)^{2/3}/D$ is the dimensionless amplitude that depends on the luminosity distance from the source, D, and the chirp mass of the binary. In our analysis, A_0 is fixed by the signal-to-noise ratio (SNR) of the source.

The Doppler modulation and polarization phases are given by

$$\Phi_D(t) = 2\pi f L \sin\theta \cos\left(2\pi f_m t - \phi\right), \tag{6.17}$$

$$\Phi_P(t) = \tan^{-1}\left(\frac{-F_\times(t)A_\times}{F_+(t)A_+}\right), \tag{6.18}$$

where $f_m = 1\text{yr}^{-1}$, $L = 1\text{AU}$. The angles, θ and ϕ, are the ecliptic colatitude and longitude respectively. The functions $F_+(t)$, $F_\times(t)$ depend on θ, ϕ and the polarization angle ψ.

For these quasi-monochromatic signals, we can approximate the Fisher matrix using a time-domain integration [33, 144, 148, 180]:

$$\begin{aligned}\Gamma_{ij} =& 4\text{Re}\left[\int_0^\infty df \frac{(\partial_i \tilde{h})^* \partial_j \tilde{h}}{S_n(f)}\right], \\ \approx& \frac{2}{S_n(f_0)} \int_0^{T_{\text{obs}}} dt \left(\partial_i h \partial_j h\right),\end{aligned} \tag{6.19}$$

where the inner product $\langle .. | .. \rangle$ is introduced in Sec. 2.6.1, $\tilde{h}$ represents the Fourier transform of the signal h, and ∂_i represents the partial derivative with respect to the waveform parameter θ^i. The power spectral density, $S_n(f)$, of LISA follows from [181]. Here, the ppE model contains 9 parameters in total: $\boldsymbol{\theta} = \{A_0, \phi_0, \psi, \iota, \theta, \phi, f_0, \mathcal{M}, \gamma\}$. For signals with long integration time, we can further separate the fast-oscillating part from the slow-evolving part to reduce the computation time [144]:

$$\Gamma_{ij} \approx \frac{1}{S_n(f_0)} \int_0^{T_{\text{obs}}} dt \left(\partial_i \mathcal{A} \partial_j \mathcal{A} + \mathcal{A}^2 \partial_i \Phi \partial_j \Phi\right). \tag{6.20}$$

To make this approximation, we have assumed that the fast oscillating parts $\cos\Phi(t) \approx \cos\left(2\pi f_0 t + \phi_0\right)$ and $\sin\Phi(t) \approx \sin\left(2\pi f_0 t + \phi_0\right)$ can be integrated separately from the slowly evolving parts. We further assume that $\int_0^{T_{\text{obs}}} dt \cos^2\Phi(t) = \int_0^{T_{\text{obs}}} dt \sin^2\Phi(t) =$

$1/2$ and $\int_0^{T_{\rm obs}} dt \cos\Phi(t)\sin\Phi(t) = 0$. Similarly, the SNR is given by

$$||h|| \approx \sqrt{\frac{1}{S_n(f_0)}\int_0^{T_{\rm obs}} dt \mathcal{A}^2}. \tag{6.21}$$

Using the ppE waveform, we compute the statistical uncertainties of γ by first ignoring the astrophysical effects. For each chosen value of n, we estimate the 1-σ uncertainty as the diagonal component of the inverse of the Fisher matrix as described in Sec. 2.6.3.

In Fig. 6.2, we show the statistical uncertainties of γ for theories with different n for one simulated detached close DWD systems used in [74] whose parameters are listed in Table E.1 while the fiducial value of γ has been set to 0. The left panel shows results for $T_{\rm obs}$ of 3 and 6 years respectively. The statistical uncertainties have scaling of $T_{\rm obs}^D$, where D lies between -3.5 and -5 (see Appendix E.1), and hence 6 years of observation provides better constraint by an order of magnitude. The constraints on γ by some other observations are included for comparison. The first detected binary BH merger event, GW150914, gives a tighter bound on γ for positive n due to the higher frequency of the signal. Meanwhile, the binary pulsar constraint from PSR J0737-3039 provides better bounds than DWDs at almost all PN orders, especially for more negative n. The updated bounds on γ from the third gravitational wave transient catalog (GWTC-3) [182] for $n = -1$ and 0 to 2 are also shown. The mapping between the measured bounds in [182] and the ppE parameter β is given in Eqs. (10) and (11) of [183], while that between β and γ is described in Sec. 6.1 (below Eq. (6.4)). From the figure, the GWTC-3 provides a better bound at $n = -1$ and similar bounds for other values compared to GW150914.

Among the detached DWD systems in the LISA verification binaries [184], the indi-

vidual masses of the WDs have been measured up to ∼3% (e.g., J0651+2844 [185]). Assuming we have electromagnetic counterparts or other means of measurement (e.g., GW measurements in other frequency bands [186]), the GW signal can provide better bounds on γ. In the right panel of Fig. 6.2, we place priors of different r.m.s. width on the chirp mass (1%, 0.1% of the fiducial value respectively) following [74]. Because we are using a Fisher analysis, we impose Gaussian priors through the replacement $\Gamma_{ij} \to \Gamma_{ij} + \delta_{ij}/\sigma_i^2$ [187, 188] (see also Sec. 2.6.3), where δ_{ij} is the Kronecker delta function and σ_i is the r.m.s. width of the ith parameter. Note that the repeated indices are not summed over. We then computed the statistical error of γ for an observation time of 3 years. We find that, as expected, imposing tighter priors can improve the bounds on γ. In particular, a precise measurement of the chirp mass up to 0.1% would result in more stringent constraints than the pulsar for some n. This result is similar to that in [74] for the constraints on the coupling parameters of a specific class of scalar-tensor theories.

6.2.2 Systematic error

The astrophysical effects introduced in Sec. 6.1 causes deviation of $\dot{f}_0^{(\mathrm{tr})}$ and $\ddot{f}_0^{(\mathrm{tr})}$ (Eqs. (6.5) and (6.6)) from the approximate model used in Sec. 6.2.1. In this subsection, we focus on estimating the systematic errors on γ caused by neglecting these effects in the waveform model following [189]. We first briefly review the formalism and apply it to each astrophysical contribution to the waveform.

We assume that the true waveform signal that includes all contributions from the astrophysical effects, as well as the non-GR effects, is given by

$$h_0(t) = \mathcal{A}_0(t) \cos \Phi_0(t), \tag{6.22}$$

while the approximate waveform model we use for parameter estimation is

$$h_{\rm A}(t) = \mathcal{A}_{\rm A}(t)\cos\Phi_{\rm A}(t). \tag{6.23}$$

The true waveform parameters are denoted by $\boldsymbol{\theta}_0$. In particular, $\Phi_0(t)$ is expressed as Eq. (6.15) with $\dot{f}_0$ and $\ddot{f}_0$ replaced with $\dot{f}_0^{(\rm tr)}$ and $\ddot{f}_0^{(\rm tr)}$ while the approximate waveform is described in Eq. (6.13). Using the latter waveform model, the measured parameters, denoted by $\boldsymbol{\theta}_{\rm A}$, would then have a systematic shift from the true values estimated by the formula[2]

$$\Delta\theta^i_{\rm sys} = \left(\Gamma^{-1}\right)^{ij}\langle\partial_j h|\Delta\mathcal{A}\cos(\Phi) - \mathcal{A}\Delta\Phi\sin(\Phi)\rangle|_{\boldsymbol{\theta}=\boldsymbol{\theta}_{\rm A}}, \tag{6.24}$$

where $\Delta A = A_0(t;\boldsymbol{\theta}_{\rm A}) - A_{\rm A}(t;\boldsymbol{\theta}_{\rm A})$ and $\Delta\Phi = \Phi_0(t;\boldsymbol{\theta}_{\rm A}) - \Phi_{\rm A}(t;\boldsymbol{\theta}_{\rm A})$. Notice that all the amplitudes and phases are evaluated at the parameter values estimated by the approximate waveform. As mentioned in [189], this formula is valid for $\Delta\theta^i_{\rm sys}\Delta\theta^j_{\rm sys}\partial_{ij}\Phi \ll 1$.

Using the source parameters of "sim." in Table E.1, we compute systematic errors caused by the astrophysical effects listed in Sec. 6.1 and show the results in Fig. 6.3. Since the astrophysical effects depend on the individual masses while we only give the chirp mass in the table, we vary the binary's mass ratio, q [3], and fix $n = -1$. Without priors on $\mathcal{M}$, the statistical error dominates over the systematic error contribution from the astrophysical effects we consider. To impose better constraints on γ, priors on $\mathcal{M}$ can be imposed, assuming that we are given independent measurements on the masses of the binary constituents, as described in Sec. 6.2.1. For systems with a large mass ratio, the systematic error becomes significant enough to affect the

[2]The original formula in [189] is in frequency domain while we extended it to time domain.

[3]Note that the original simulated source has a fixed mass ratio. Here, we show how the astrophysical effects depend on it by varying its value between 0 and 1.

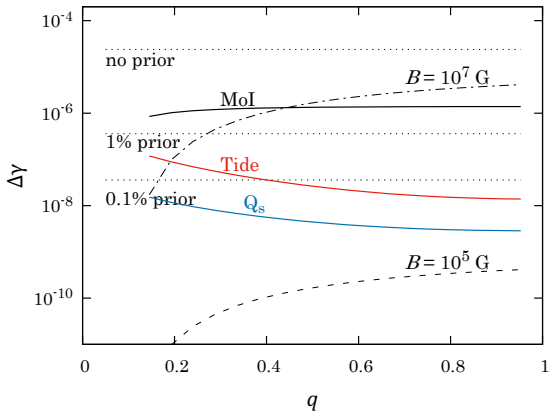

Figure 6.3: The statistical and systematic errors on γ of the DWD system in Table E.1 for $n = -1$ at different mass ratios. Different priors are imposed on the chirp mass when estimating the statistical errors (dotted lines) as described in the right panel of Fig. 6.2

.

constraints on γ if the chirp mass is independently measured up to 1% level or below, and therefore should not be ignored in the waveform model.

6.2.3 Parameter estimation with astrophysical effects

As shown above, the astrophysical effects can affect our ability to constrain γ. To place accurate bounds, we need to perform parameter estimation that accounts for these additional effects. In this subsection, we briefly discuss how $\Delta\gamma$ gets affected when we include the additional astrophysical parameters to the search parameter set.

The information about the orbital evolution is contained in the frequency evolution of the signal, i.e., within $\dot{f}_0$ and $\ddot{f}_0$. In the approximate model, we relate $(\dot{f}_0, \ddot{f}_0)$ to $(\mathcal{M}, \gamma)$ through Eqs. (6.3) and (6.4). When we include the astrophysical contributions, the waveform model depends on additional parameters like the moment of inertia or the magnetic field. In principle, higher-order derivatives of the frequency need to be measured in order to determine those. However, that can be challenging

given the limited observation time and sensitivity of the detector. We are then prone to having strong degeneracies between the parameters.

On the other hand, some of the astrophysical parameters have scaling relations with the WD masses. We can therefore impose priors on these additional parameters to break the degeneracies. As an example, we consider the statistical error on γ, denoted by $\Delta\gamma_I$, with a waveform model containing the original 9 parameters and the total moment of inertia of the WDs through a 10×10 Fisher information matrix. For different n, the fractional difference $(\Delta\gamma_I - \Delta\gamma)/\Delta\gamma$ (where $\Delta\gamma$ is the statistical error on γ for 9 parameters without the total moment of inertia) ranges from 15% to 40% if we assume a Gaussian prior of 50% of the fiducial value of I (see Fig. 6.4). The result converges to values slightly smaller than $\Delta\gamma$ as we impose tighter priors. This difference is due to the change in the phase of the signal by including Δ_I, which causes a change in the Fisher matrix elements. This causes a non-vanishing difference between $\Delta\gamma_I$ and $\Delta\gamma$ even if we use an extremely tight prior. Still, the result shows that if we have a certain knowledge of the astrophysical parameters, the constraints on γ are expected to be close to the 9-parameter case.

6.3 Application to screened modified gravity

The SMG is a class of scalar-tensor theories that has a screening mechanism forcing deviations from GR significant only on a large scale, allowing them to pass some of the most stringent constraints from solar system tests while being able to explain cosmological scale observations [190, 191]. Since the screening mechanism works less efficiently for WDs than NSs or BHs, WD binaries may place more stringent bounds on the theory than binary neutron stars or BHs.

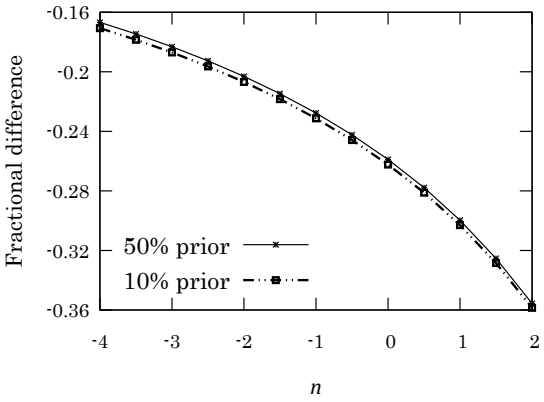

Figure 6.4: The fractional difference on the statistical error $\Delta\gamma$ with and without the total moment of inertia of the binary in the search parameter set. Gaussian priors with r.m.s. width of either 10% or 50% of the fiducial value of the total moment of inertia I is imposed.

The action of a scalar-tensor theory in the Einstein frame is written as

$$S = \int d^4x\sqrt{-g}\left[\frac{M_{\rm Pl}^2}{2}R - \frac{1}{2}(\nabla\tilde{\Phi})^2 - V(\tilde{\Phi})\right] + S_{\rm M}, \tag{6.25}$$

where $M_{\rm Pl} = \sqrt{\hbar/(8\pi)}$ is the reduced Planck mass, R is the Ricci scalar, $V(\tilde{\Phi})$ is the bare potential for the scalar field $\tilde{\Phi}$, and $S_{\rm M}$ is the matter action. Note that the matter fields are minimally coupled to the Jordan frame metric, $\bar{g}_{\alpha\beta}$, which is related to the Einstein frame metric $g_{\alpha\beta}$ through a conformal coupling $\bar{g}_{\alpha\beta} = A^2(\tilde{\Phi})g_{\alpha\beta}$.

The scalar field follows the Klein-Gordon equation

$$\Box\tilde{\Phi} = \frac{\partial V_{\rm eff}}{\partial\tilde{\Phi}}, \tag{6.26}$$

where $\Box$ is the Einstein frame d'Alembertian, $V_{\rm eff}$ is the effective potential that depends on the bare potential and the conformal coupling $A^2(\tilde{\Phi})$ (see [190] for details). The minimum of $V_{\rm eff}$ represents the physical vacuum and gives the vacuum expectation value of the field $\Phi_{\rm VEV}$. Within SMG theories, this $V_{\rm eff}$ has density dependence

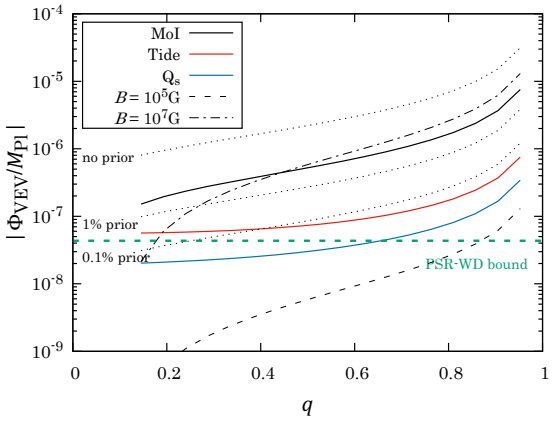

Figure 6.5: Statistical and systematic error on the non-GR parameter of SMG for systems with different mass ratios. The statistical error with different priors on the chirp mass as shown with dotted lines.

such that the field around the vacuum acquires an effective mass that increases with density.

At the leading PN order (-1PN), these theories introduce a non-GR effect scaling inversely as the compactness of the stars [190]:

$$\gamma = \frac{5}{192}\eta^{2/5}\left(\frac{\Phi_{\rm VEV}}{M_{\rm Pl}}\right)^2\left(\frac{1}{C_1}-\frac{1}{C_2}\right)^2, \tag{6.27}$$

where $C_A = m_A/R_A$ is the compactness of the Ath WD. Using Eq. (6.27), we can convert the measurement errors of γ into bounds on the SMG non-GR parameter. We show the results for systems with orbital parameters given in Table E.1, but of various mass ratios, $q = m_1/m_2$, in Fig. 6.5. Due to the dependence on compactness, both the statistical error and systematic error increase with q. Similar to the results in Sec. 6.2.2, the statistical error reaches the level of the current observation bounds set by the pulsar-WD binary PSR J1738+0333 [192, 193] for tight priors on the chirp mass of $\sim$0.1%. If the DWD system has $q < 0.3$, the GW signal can potentially improve the bound on $\Phi_{\rm VEV}/M_{\rm Pl}$. Even in those optimal cases, the astrophysical

effects still need to be accounted for in the waveform model.

6.4 Chapter summary

In this chapter, we study the possibility of testing GR with GW signals from galactic DWD systems using LISA in the presence of various astrophysical effects. We employ the ppE waveform model to parameterize the non-GR effect with γ at different PN order n. First, we illustrate the ability of LISA to constrain γ with the ppE waveform without the astrophysical effects by computing the Fisher matrix. Compared to GW signals from binary BH coalescence, the DWD signal can provide more stringent bounds at negative PN order like that of pulsar observations. However, it requires a tight prior on the chirp mass of the system in order to reach the same level as the most stringent binary pulsar bounds.

We then consider the astrophysical effects on the parameter estimation, namely the rotation effect, tidal effect, spin-induced deformation, and dissipation through the unipolar induction within the magnetosphere. Assuming that the waveform model is missing these effects, we estimate the systematic shift of the measured γ and show that it becomes significant when the required accuracy of γ is near that of the binary pulsar constraint. In other words, one cannot leave out these effects in the waveform model.

Lastly, we apply the results of ppE model to constrain the SMG theory. The non-GR parameter, $\Phi_{\rm VEV}/M_{\rm Pl}$ has inverse dependence on the compactness of the stars of the binary, making DWDs a good type of source to test this theory. Our results however show that using DWD to pose better constraints than the current bound from PSR-WD binaries is challenging as it requires a tight prior and accurate modelling of

several astrophysical effects involved.

Regarding future work, we plan to extend the study of testing GR with other potential LISA GW sources with smaller spacetime curvature (see Appendix E.2) that are also promising in testing theories with screening mechanisms like the SMG. However, the population of some of these sources is still poorly known. Further studies on the population models and the orbital dynamics are required for such systems.

Chapter 7

Probing crystalline quark matter within the neutron star core

This chapter is based on the results reported in [21]. We study the prospects of using the resonance effect of dynamical tide on the GW signals to probe the crystalline QM inside the NS core. We focus on the i-mode of an HS with a CCS phase core [22, 28, 44]. This i-mode originates from the density and the shear modulus discontinuity between the QM core and HM envelope. We demonstrate that this mode can be resonantly excited during the inspiral phase of a binary NS merger, leaving a shift in the GW phase and time before coalescence in the GW signal [18, 194].

We then use a Fisher analysis to estimate the detectability of the shift for various HS models and find that the mode can be detected even with the current generation of GW detectors, if the CCS phase shear modulus is large enough and the phase transition happens at low pressure. Since the i-mode depends strongly on the properties of the quark-hadronic matter interface, detection of such a mode would provide strong evidence of deconfinement within the HSs.

In the following, we first introduce the EOS of the HS models in Sec. 7.1. Next, we study the effects of the i-mode on the GW signal in Sec. 7.2. We then describe the details of the Fisher analysis in Sec. 7.3. We provide the numerical results of the i-mode properties and the Fisher analysis in Sec. 7.4. Lastly, we comment on the

numerical method we use

7.1 Equation of state

We start by describing the construction of the EOSs used in our analysis.

7.1.1 Quark matter EOS: Modified Bag Model

The QM core is assumed to be described by the phenomenological modified MIT bag model. In addition to the ρ-p relation given in Eqs. (2.14) and (2.15) of Sec. 2.2.2, we also need the shear modulus of the CCS phase. Ref. [97] performed the study of the elastic properties and gave the formula for the shear modulus:

$$\mu = \nu_0 \left(\frac{\Delta}{10 \text{ MeV}}\right)^2 \left(\frac{\mu_q}{400 \text{ MeV}}\right)^2, \tag{7.1}$$

where the constant ν_0 has a value of 2.47 MeV/fm^3. Δ is the gap parameter of the CCS phase with a range between 5 MeV and 25 MeV [97].

7.1.2 Hadronic matter EOS

Next, we explain hadronic EOSs (HEOSs) for constructing HSs. It is expected that the EOS gets softened as quark matter appears inside the core. To ensure that the HS EOSs have the maximum stable mass beyond the 2 $M_\odot$ constraint from observations, we do not consider HEOSs that are too soft. The models we classify as intermediate in terms of stiffness are: MPa1 [195], DDHδ [196], Hebeler2; and those with high stiffness are: MS1 [197], NL3 [113], TM1 [198], Hebeler3. The models

Hebeler2 and Hebeler3 are taken from the subtables labelled as “intermediate” and “stiff” respectively in Table 5 of [199]. They are the representative HEOSs with the low-density part satisfying the results derived from CFT. The sub- and supranuclear density parts satisfy the constraints from massive pulsars. For simplicity, we do not include detailed crust models containing additional phase transitions and possible density gaps in the outer crust region that can give rise to additional i-modes or g-modes in the low-frequency region (10-100 Hz) [44].

7.1.3 Hybrid star models

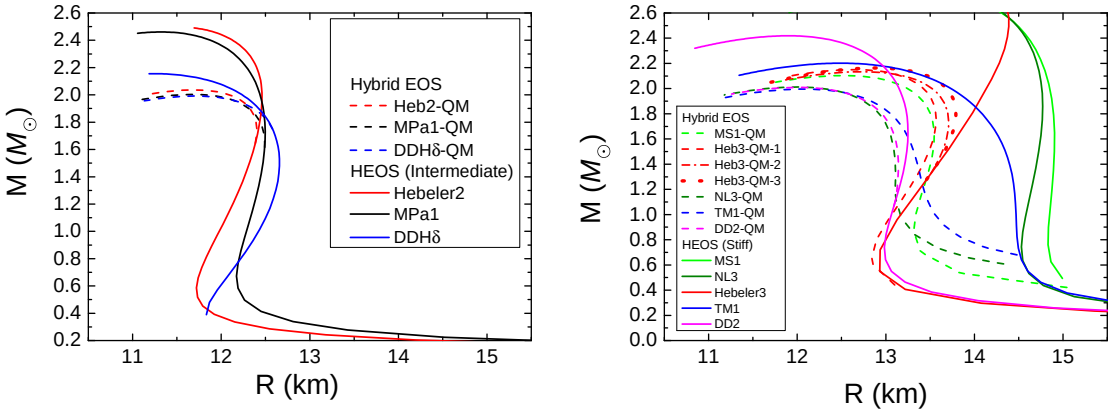

Figure 7.1: M-R relations of the HS models (dashed lines) and hadronic matter models (solid lines) constructed with intermediate (left) and stiff (right) HEOSs.

We now use the quark and hadronic matter EOSs explained in the previous subsections to construct HS models. The first-order phase transition from hadronic matter to quark matter is modeled with Maxwell construction, which requires the continuity of pressure and the baryon chemical potential, assuming local charge neutrality. The density is discontinuous at the transition point. The procedure of the construction is presented in Appendix F.2.

We construct HS models with different combinations of a_4, a_2, $B_{\rm eff}$, Δ and nuclear matter EOSs, requiring the HS EOSs to satisfy the observational constraints on the maximum mass ($M_{\rm TOV} > 2\ M_\odot$), radius ($R_{1.4M_\odot} \in [8.9, 13.5]$ km from various multi-messenger observations; see Table 1 of [200]) and tidal deformability ($\bar{\Lambda} < 800$). The EOS parameters of the HS models constructed are listed in Table 7.1.

EOS	a_4	$a_2^{1/2}$ (MeV)	$B_{\rm eff}^{1/4}$ (MeV)	HEOS	P_t (dyn cm^{-2})	$\rho_t^{\rm QM}$ (g cm^{-3})	$\rho_t^{\rm HM}$ (g cm^{-3})
MS1-QM	0.52	108	135	MS1	6.21E33	3.73E14	2.26E14
Heb3-QM-1	0.5	102	134	Hebeler3	1.14E34	3.78E14	3.52E14
NL3-QM	0.53	90	140	NL3	1.04E34	4.23E14	2.86E14
TM1-QM	0.55	105	140	TM1	1.32E34	4.45E14	3.18E14
Heb3-QM-2	0.53	143	128	Hebeler3	5.02E34	5.13E14	4.78E14
Heb3-QM-3	0.53	156	123	Hebeler3	4.75E34	4.84E14	4.83E14
DD2-QM	0.55	100	140	DD2	4.32E34	5.46E14	5.29E14
MPa1-QM	0.57	90	140	MPa1	1.23E35	8.13E14	7.94E14
Heb2-QM	0.55	70	140	Hebeler2	1.26E35	8.04E14	7.78E14
DDHδ-QM	0.57	87	142	DDHδ	1.53E35	9.22E14	9.17E14

Table 7.1: HS EOSs with the quark matter EOS parameters, the HEOSs and P_t for the envelope listed. The EOSs are divided into 3 sections characterized by the transition pressures: low P_t (top), intermediate P_t (middle), high P_t (bottom). The transition densities (ρ_t) are also shown, with superscripts "QM" denoting the quark matter phase and "HM" denoting hadronic phase.

In Fig. 7.1, we show the mass-radius relations of the HS models and the HEOSs. We classify the EOSs into "intermediate" and "stiff" EOSs based on their radius within the mass range between 1–2 $M_\odot$. We do not consider HEOSs that are too soft, since the appearance of quark matter softens the EOSs further for densities beyond the quark-hadron transition point compared to the corresponding HEOSs, which leads to a maximum stable mass below the current bound of 2 $M_\odot$. The quark matter EOS parameters are also restricted within a certain range due to this maximum mass constraint.

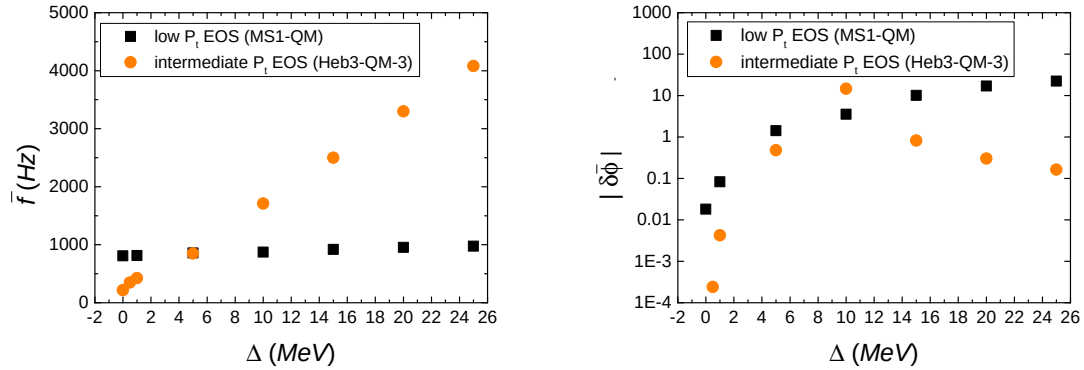

Figure 7.2: (Left) The weight-averaged i-mode frequency of (1.4,1.4) $M_\odot$ HS binary models against Δ. A low P_t EOS (MS1-QM; in black squares) and an intermediate P_t EOS (Heb3-QM-3; in orange dots) are chosen to construct the models. (Right) Similar to the left panel but for the total overall phase shift. The phase shift of Heb3-QM-3 near $\Delta = 10$ MeV exceeds over 10 due to the avoided crossing between the i-mode and the f-mode (not shown in this figure). Near this region, the phase shift of the two modes comes close to each other and the resonant frequencies repel to avoid a degeneracy.

Putting the observational constraints into consideration, we expect that the transition pressure P_t of the HS EOSs in Table 7.1 is loosely correlated with the stiffness of the HEOSs in order to produce models that are stiff enough to support 2 $M_\odot$, but cannot be too stiff not to exceed the upper bound set on the tidal deformability and radius measurements. Roughly speaking, the maximum mass observations constrain the EOS stiffness from below while the upper bound set on radius and tidal deformability measurements constrain from above. Since the appearance of quark matter softens the EOSs and generally lowers the maximum mass, soft HEOSs that barely meet the constraints on maximum mass cannot be used to construct valid HS EOSs. Also, an HS EOS with a hadronic part of intermediate stiffness must have a high P_t, which in turn gives a transition point at relatively high mass on the M-R curve (see the left panel of Fig. 7.1), to satisfy the 2 $M_\odot$ lower bound on the maximum mass. Meanwhile, those with a stiff HEOS cannot have a high P_t, or else it would exceed the 13.5 km

upper bound on the radius (see the right panel of Fig. 7.1).

In the following analysis, we classify the HS EOSs according to P_t. The models with HEOSs of intermediate stiffness will have a high P_t in order to meet the observational constraints. For those with a stiff HEOS, we can construct a wider range of P_t covering intermediate P_t and low P_t as indicated in Table 7.1, while the HS models still satisfy the observation bounds.

7.2 Mode contribution to waveforms

In this section, we first explain how to compute the i-mode oscillations of HSs via a hybrid method. We next describe how such oscillation modes affect the GW waveforms from binary HS inspiral.

7.2.1 Non-radial pulsation modes in a hybrid formalism

To calculate the effects of the i-modes on the GW signal, we need to first solve for the i-mode frequencies and eigenfunctions for a given EOS and use this to find the tidal overlap integral which will be introduced in Sec 7.2.2. The formulation within the Newtonian framework is described in [194], which requires one to use the Newtonian equations to construct the background solution and the perturbed, pulsating solution. In this study, we take a different approach called a hybrid formulation (see, e.g., [15, 18]), where we include fully relativistic effects for the background but keep the perturbation to a Newtonian level. We also assume that the shear stress from the solid component enters at the perturbative level, i.e. the background is unsheared for the crystalline structure, such that the background is isotropic unlike in Chapter 5.

For the background non-rotating, radially-symmetric solution, we solve the TOV equations explained in Sec. 2.1. The formulae governing the pulsation in Newtonian theory can be found in various literature. We employ a formulation consistent with that of [201, 202]. The formulation and the corresponding derivation are briefly discussed in Appendix F.1. By numerically solving the set of pulsation equations, we can obtain the eigenfrequencies and eigenfunctions of a set of non-radial modes for each spherical degree ℓ. This hybrid method of using a relativistic background and Newtonian perturbation is expected to deviate from a fully consistent approach. In Appendix F.3, we perform a numerical check to quantify the difference.

7.2.2 Tidal coupling and phase shift in the waveform

During a HS-HS inspiral, the i-modes resonate as the orbital frequency sweeps through the resonant frequency and causes a phase shift in the GW waveform. Here we first focus on the mode excitation of one of the HS in the binary, for which the physical quantities are indicated with the subscript 1. Following Lai [194], the overall phase shift for an $\ell = 2$ mode is given by the equation

$$\delta\phi_\alpha = -\frac{5\pi^2}{4096}\left(\frac{R_1}{m_1}\right)^5 \frac{2q}{(1+q)}\frac{1}{\Omega_{n2m}^2}\left|I_{n2m}\right|^2, \tag{7.2}$$

where m_1 and R_1 are the stellar mass and radius of the pulsating HS, q is the ratio of the companion mass to that of the pulsating HS, Ω_{n2m} is the normalized resonant frequency for the $\ell = 2$ mode defined by

$$\Omega_{n\ell m}^2 = \frac{R_1^3\omega_{n\ell m}^2}{m_1}, \tag{7.3}$$

with $\omega_{n\ell m}$ representing the mode angular frequency, $I_{n\ell m} = I_\alpha$ is the tidal coupling coefficient defined in Sec. 2.4.2. Here we use the set of subscripts $\alpha = (n, \ell, m)$[1] to specify an eigenmode with a radial quantum number n, spherical harmonics degree ℓ and order m. The quantum number n is an index that labels all the non-radial modes with the same ℓ and m, ranked in ascending order of resonant frequencies. For a typical NS with a solid crust, this includes the f-mode, the i-mode and the gravity (g_1, g_2, ...) modes, etc.[2] [28]. The eigenvectors are normalized by

$$\int d^3x\rho \left|\boldsymbol{\xi}_\alpha\right|^2 = m_1 R_1^2. \tag{7.4}$$

Note the slight difference in normalization constant compared to Eq. (2.38) in Sec. 2.4.2. We use this normalization throughout this chapter for consistent leading coefficients in our formulas with [194].

We investigate only the $(\ell, m) = (2, \pm 2)$ i-mode contribution on the GW phase, which dominates the phase shift. From Eq. (2.41), we can easily see that $I_{n22} = I_{n2-2}$. Hence, we have the i-mode overall phase shift given by

$$\delta\phi_{\alpha_i} = -\frac{5\pi^2}{2048}\left(\frac{R}{M}\right)^5 \frac{2q}{(1+q)}\frac{1}{\Omega^2_{n_i 22}}\left|I_{n_i 22}\right|^2, \tag{7.5}$$

where n_i is the radial quantum number corresponding to the i-mode, and α_i is the index representing the combined contributions from the $\ell = 2$ i-modes, i.e., the sum of $(n_i, 2, 2)$ and $(n_i, 2, -2)$ modes.

[1] In Sec. 2.4.2, we have an additional index s to specify the sign of the frequency, which is needed in general for a rotating star. Here, we can combine the positive frequency mode and the negative frequency mode into one and drop the index s as they are identical if we consider only non-rotating stars.

[2] f and i do not have any subscripts since for each (ℓ,m) there is only one f-mode and one i-mode per interface.

The contribution from a pulsation mode on a binary inspiral waveform appears as a shift in the phase and time when the binary sweeps through the resonant frequency. The resulting correction to the phase in the frequency domain is given by [9, 18, 203]

$$\Delta\Psi_{\alpha_i}(f) = -\sum_{A=1,2} \delta\phi^{(A)}_{\alpha_i} \left(1 - \frac{f}{f^{(A)}_{\alpha_i}}\right) \theta(f - f^{(A)}_{\alpha_i}), \tag{7.6}$$

where $\Delta\Psi_{\alpha_i}(f)$ is the phase correction in frequency domain, $\delta\phi^{(A)}_{\alpha_i}$ and $f^{(A)}_{\alpha_i}$ are the overall phase shift and the resonant frequency due to the i-mode of the Ath body, and f is the GW frequency from the inspiral. $\theta(f - f_{\alpha_i})$ is the Heaviside step function. To reduce the number of parameters, we follow [204] and rewrite the above phase shift as

$$\Delta\Psi_{\alpha_i}(f) \approx -\delta\bar{\phi}_{\alpha_i} \left(1 - \frac{f}{\bar{f}_{\alpha_i}}\right) \theta(f - \bar{f}_{\alpha_i}), \tag{7.7}$$

where the total phase shift $\delta\bar{\phi}_{\alpha_i}$ and the weight-averaged mode frequency $\bar{f}_{\alpha_i}$ are given by

$$\delta\bar{\phi}_{\alpha_i} = \delta\phi^{(1)}_{\alpha_i} + \delta\phi^{(2)}_{\alpha_i}, \tag{7.8}$$

$$\bar{f}_{\alpha_i} = \delta\bar{\phi}_{\alpha_i} \left(\frac{\delta\phi^{(1)}_{\alpha_i}}{f^{(1)}_{\alpha_i}} + \frac{\delta\phi^{(2)}_{\alpha_i}}{f^{(2)}_{\alpha_i}}\right)^{-1}. \tag{7.9}$$

In the following, we drop the subscript α_i on the mode frequency and phase shift to simplify the expressions.

7.3 Waveform analysis

To estimate the statistical uncertainties in measuring the waveform parameters, we employ the Fisher matrix approach described in Sec. 2.6.3. The Fisher matrix Γ_{ij} is

constructed from the phenomenological waveform model denoted as "IMRPhenomD" with tidal and resonance contributions.

The GW waveform has the form

$$h(f) = A(f)e^{-i\Psi(f)}. \tag{7.10}$$

The functional forms of the amplitude $A(f)$ and phase $\Psi(f)$ contain the point particle contributions described in [205, 206] (the IMRPhenomD model). In addition, the 5PN and 6PN tidal contributions in [10, 207], and the effect of mode resonance given in Eq. (7.7) are added to the phase. The elements of the parameter set θ^i are given by

$$\theta^i = \left\{\ln \mathcal{A}, \phi_c, t_c, \ln \mathcal{M}_z, \ln \eta, \chi_s, \chi_a, \bar{\Lambda}, \delta\bar{\Lambda}, \bar{f}, \delta\bar{\phi}\right\}. \tag{7.11}$$

The meaning of each element is as follows: the sky-averaged normalized amplitude

$$\mathcal{A} = \frac{\mathcal{M}_z^{5/6}}{\sqrt{30}\pi^{2/3}d_L}; \tag{7.12}$$

with the luminosity distance from the source d_L; the redshifted chirp mass $\mathcal{M}_z = \mathcal{M}(1+z)$, where

$$\mathcal{M} = \frac{(m_1 m_2)^{3/5}}{(m_1+m_2)^{1/5}} \tag{7.13}$$

is the chirp mass; the symmetric mass ratio

$$\eta = \frac{m_1 m_2}{(m_1+m_2)^2}; \tag{7.14}$$

the symmetric and asymmetric spin parameters $\chi_{s,a} = (\chi_1 \pm \chi_2)/2$, where $\chi_{1,2}$ are the dimensionless spins of the individual stars; the reparametrization of the mass

weighted tidal deformabilities (see e.g. [207])

$$\begin{aligned}\bar{\Lambda} =& \frac{8}{13}\Big[\left(1+7\eta-31\eta^2\right)(\Lambda_1+\Lambda_2) \\ &+\sqrt{1-4\eta}\left(1+9\eta-11\eta^2\right)(\Lambda_1-\Lambda_2)\Big], \qquad (7.15)\\ \delta\bar{\Lambda} =& \frac{1}{2}\Big[\sqrt{1-4\eta}\left(1-\frac{13272}{1319}\eta+\frac{8944}{1319}\eta^2\right)(\Lambda_1+\Lambda_2), \\ &+\left(1-\frac{15910}{1319}\eta+\frac{32850}{1319}\eta^2+\frac{3380}{1319}\eta^3\right)(\Lambda_1-\Lambda_2)\Big], \qquad (7.16)\end{aligned}$$

where Λ_j are the individual $\ell = 2$ tidal deformabilities normalized by m_j^5, i.e., $\Lambda_j = \lambda_j/m_i^5$, for $j = 1, 2$ (also see Sec. 2.4.1 for the method of determining λ_2); the phase-shift-weighted i-mode frequency $\bar{f}$ and the overall phase shift due to the i-mode $\delta\bar{\phi}$. Note that if we consider binaries of identical stars, we have $\bar{\Lambda} = \Lambda_1 = \Lambda_2$ and $\delta\bar{\Lambda} = 0$.

At high frequencies, the tidal part of the waveform that we use becomes less accurate as the HSs will eventually come to contact. Following [133], we only consider the inspiral waveform, which terminates at a separation of $6(m_1+m_2)$, which is equivalent to the radius of the innermost stable circular orbit (ISCO) of an object orbiting around a non-spinning central object with mass $(m_1 + m_2)$. This corresponds to a cutoff frequency $f_{\rm ISCO} = \left[6^{3/2}\pi(m_1+m_2)\right]^{-1}$ in the Fisher estimate[3].

In the following analysis, we pick the fiducial values for (ϕ_c, t_c, χ_s, χ_a) to be (0, 0, 0, 0). The tidal deformability parameters ($\bar{\Lambda}$, $\delta\bar{\Lambda}$) are set as (800, 0) for identical HS binaries [4] and are specified otherwise in asymmetric cases. We use the spin priors of

[3]For stiff EOSs, the HSs may come to contact before reaching the separation of $6(m_1 + m_2)$, i.e., $R_1 + R_2 > 6(m_1 + m_2)$, where R_1 and R_2 are the radii of the HSs. In these cases, the actual cutoff frequency should be set lower than $f_{\rm ISCO}$. However, since the spectral noise density increases quickly in the high-density region, the uncertainty estimates using the Fisher matrix is not significantly affected as long as the actual cutoff frequency does not differ too much from $f_{\rm ISCO}$ and the i-mode resonant frequencies are not too close to the cutoff frequency.

[4]In reality, $\bar{\Lambda}$ varies for different EOSs. However, we have checked that $\Delta\delta\bar{\phi}$ is insensitive to the choice of $\bar{\Lambda}$ and thus in this study, we fix its value to be 800 for simplicity . Same applies to $\delta\bar{\Lambda}$ with its value fixed to be 0.

$|\chi_{s,a}| < 1$ and tidal priors of $0 < \bar{\Lambda} < 3000$ and $|\delta\bar{\Lambda}| < 500$ [207]. The values of $\bar{f}$ and $\delta\bar{\phi}$ depend on the HS models and are calculated with the method described in Sec. 7.2.

7.4 Numerical results

Let us now present all the numerical results. We first show how the i-mode frequency and phase shift depend on the quark parameters, in particular Δ. We next present the detectability of such modes with current and future GW observations, including the existing GW events of GW170817 and GW190425.

7.4.1 i-mode dependence on the properties of the phase transition

The frequency and phase shift of the i-mode depend strongly on both the density gap and shear modulus gap at the interface. Each EOS listed in Table 7.1 has a specific value of density gap, while the shear modulus for each model can still vary with Δ according to Eq. (7.1). To get an idea of how the elastic properties affect the i-mode, we consider HSs with quark matter in the CCS phase with different Δs.

In Fig. 7.2, we show the i-mode frequency and phase shift against Δ of two representative HS models with 1.4 $M_\odot$. MS1-QM, denoted by the black squares, is a HS model with a low P_t, while Heb3-QM-3, denoted by orange dots, is a model with intermediate P_t.

The Δ dependence of $\bar{f}$ and $\delta\bar{\phi}$ are found to be much stronger for the intermediate P_t model. Besides, the Δ dependence for $\delta\bar{\phi}$ for this model is not monotonic in contrast

to the low P_t models. This is because $\delta\bar{\phi}$ varies as the square of the tidal coupling coefficient, $I_{n\ell m}$, and inversely with the square of the mode frequency (see Eq. (7.5)). For small Δ, the rate of increase in $|I_{n\ell m}|$ outweighs that of the mode frequency, while the opposite happens at large Δ. This causes $\delta\bar{\phi}$ to increase initially and fall off for large Δ.

The peak of $|\delta\bar{\phi}|$ with a value of ~ 40 near $\Delta = 10$ MeV is a consequence of mode repulsion. When the frequency of the i-mode is close to another mode, such as a spheroidal shear mode, the mode frequencies repel with each other without crossing while the phase shift of the two modes comes close to each other. This phenomenon is the avoided crossing and is commonly observed in stellar pulsation problems (see e.g., Ch.17 of [27]) as well as other eigenvalue problems. The avoided crossing near $\Delta = 10$ MeV in Fig. 7.2 happens between the i-mode and the f-mode. To further demonstrate this phenomenon, we show in Fig. 7.3 both the i-mode and f-mode for Δ between 7 and 11 MeV with the EOS Heb3-QM-3. Observe that there is a repulsion in mode frequencies around $\Delta = 9.5$ MeV, while $|\delta\bar{\phi}|$ of the two modes cross each other.

As mentioned in Sec. 7.2, the i-mode results are obtained from a hybrid method which we solve the TOV equation to construct the accurate HS background models and the Newtonian pulsation equations to obtain the i-mode frequencies and overlap integrals. In Appendix F.3, we perform a numerical check to evaluate the validity of this hybrid method. Since there is no consistent full relativistic approach to simultaneously compute the background, the i-mode and the resonant effects on the GW phase, we only compare the difference between our hybrid method and a fully Newtonian approach. The result shows that the two approach predict frequencies differ by $\sim$25% and phase shifts by a factor of two.

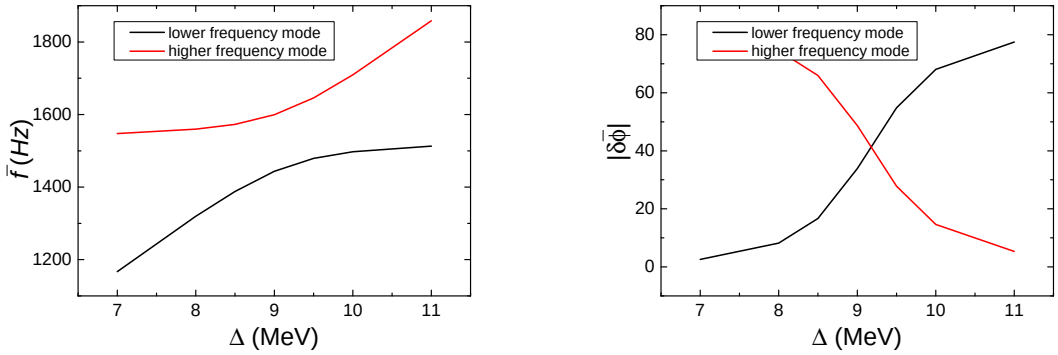

Figure 7.3: The avoided crossing of the i-mode and f-mode as Δ changes from 7 to 11 MeV of a 1.4 $M_\odot$ HS model with the EOS Heb3-QM-3. The left panel shows the repulsion of the frequencies of the higher frequency mode and the lower frequency mode. The right panel shows the exchange in $|\delta\phi|$ between the two modes.

Before we discuss the detectability of the i-mode of HSs, it is worth pointing out its difference from the typical i-modes associated with the interface(s) inside a NS (such as the one between the hadronic fluid envelope and the solid crust or phase transitions inside the crust). The i-mode frequency of HSs typically ranges between 300 and 1500 Hz, while that of a NS is generally lower. Krüger *et al.* [44] computed the $\ell = 2$ i-modes of a NS with the SLy4 EOS and a crust model with multiple first-order phase transitions using a general relativistic formalism. All of the i-modes have frequencies below 121 Hz. From the difference in mode frequencies, the i-mode of a HS can be clearly distinguished from that of a NS.

7.4.2 i-mode detectability with gravitational waves

Upon the observation of a GW signal, one can estimate the parameters that "best fit" the waveform to the measured signal buried inside the noise. Due to this, the estimated parameters always come with uncertainties. In Sec. 7.3, we have briefly discussed how the parameter estimation errors can be found using the Fisher matrix

for a large SNR. In particular, the statistical uncertainties of $\bar{f}$ and $\delta\bar{\phi}$ in the parameter estimation determine whether they are measurable from the signal. As our numerical result shows that the relative uncertainty in $\delta\bar{\phi}$ is always larger than that of $\bar{f}$, the detection criterion of the i-mode can therefore be set as $\Delta(\delta\bar{\phi}) < \left|\delta\bar{\phi}\right|$.

Equal-mass systems

Let us first analyze the detectability of the phase shift due to the excitation of the i-mode during the inspiral of a *symmetric* (equal-mass, non-spinning) HS-HS merger, which consists of identical HSs. With this assumption, $\bar{f}$ is identical to the i-mode resonant frequency, and $\delta\bar{\phi}$ is twice the phase shift of the individual HS. If we fix the mass of our models and assume no spin, there are 4 parameters that depend on the EOSs: the tidal deformability parameters $\bar{\Lambda}$ and $\delta\bar{\Lambda}$, the (weighted-averaged) i-mode resonant frequency $\bar{f}$, and the overall orbital phase shift $\delta\bar{\phi}$. One might expect the detectability of the i-mode to depend on all of the parameters. However, we found that the correlation between the tidal deformability parameters and the i-mode parameters is small. For example, the correlation coefficient $C_{\bar{\Lambda}\,\delta\bar{\phi}}$ defined in Eq. (2.61) is about 0.001–0.03 and similar for other combinations between the tidal deformability and i-mode parameters, which is much lower than that for the correlation between $\bar{f}$ and $\delta\bar{\phi}$ ($C_{\bar{f}\,\delta\bar{\phi}} \sim 0.3 - 0.8$). Hence, we can estimate the detectability by varying fiducial values of $\bar{f}$ and $\delta\bar{\phi}$ only, keeping those of $\bar{\Lambda}$ and $\delta\bar{\Lambda}$ fixed.

In the left panel of Fig. 7.4, we show $|\delta\bar{\phi}|$ and the corresponding $\bar{f}$ for each of the HS models from Table 7.1 with mass fixed at 1.4 $M_\odot$, together with the minimum $|\delta\bar{\phi}|$ required for detection based on the Fisher analysis using the Advanced LIGO (aLIGO) [208] with its design sensitivity and the Cosmic Explorer (CE) [2]. As discussed above, we set the minimum required $|\delta\bar{\phi}|$ to be its root-mean-square error

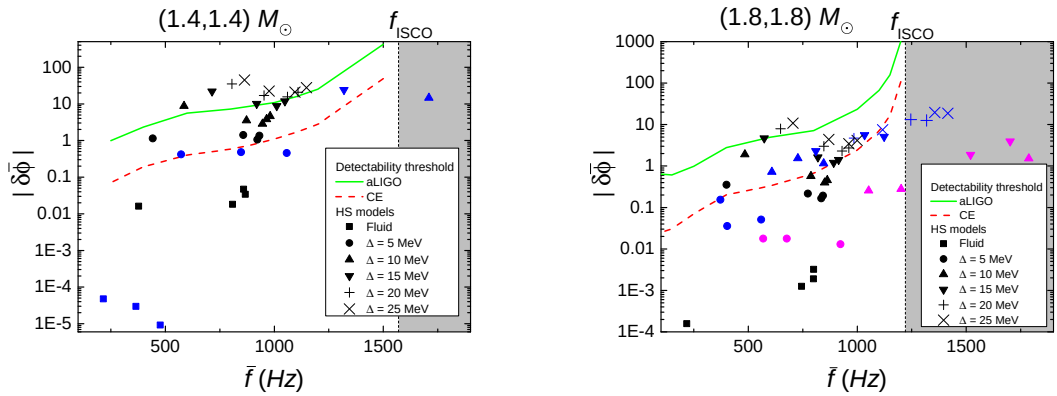

Figure 7.4: (Left) The magnitude of the i-mode's total overall phase shift $|\delta\bar{\phi}|$ and the corresponding weight-averaged resonant frequency $\bar{f}$ for each HS EOS from Table 7.1, together with the detectability threshold with aLIGO (green solid) and CE (red dashed). If a point is above these curves, such an effect is detectable with the corresponding detector. Here we have assumed an equal-mass HS system with an individual mass of 1.4 $M_\odot$. We consider intermediate P_t models (Heb3-QM-3, Heb3-QM-2, DD2-QM in blue) and low P_t models (MS1-QM, Heb3-QM-1, NL3-QM, TM1-QM in black). The i-mode becomes undetectable if the frequency $\bar{f}$ is higher than the inspiral cutoff frequency (shaded region) that we choose to be at ISCO ($f_{\rm ISCO}$). (Right) Similar to Fig. 7.4 but for individual masses of 1.8 $M_\odot$. We also present the high P_t models (MPa1-QM, Heb2-QM, DDHδ-QM) in magenta symbols. The SNR for the 1.4 $M_\odot$ system is 20 for aLIGO and 620 for CE, and that of the 1.8 $M_\odot$ system is 24 for aLIGO and 760 for CE respectively.

$\Delta(\delta\bar{\phi})$, obtained from Eq. (2.62). We have assumed the luminosity distance, d_L, to be 100 Mpc. This corresponds to a signal-to-noise (SNR) ratio of 20 for aLIGO and 620 for CE. To account for the number of interferometers, we set $N = 2$ for aLIGO and $N = 1$ for CE[5]. The detection threshold for $|\delta\bar{\phi}|$ increases with $\bar{f}$ because the detector sensitivity deteriorates at higher f and the i-mode contributes to the phase only for $f \geq \bar{f}$ (see Eq. (7.7)) and thus its contribution becomes smaller for higher $\bar{f}$.

Based on our results, the i-mode of some of the low P_t models with large Δ causes a large $|\delta\bar{\phi}|$ (~ 10) in the waveform, making its phase shift above the minimal threshold required for detection with aLIGO. Models with lower Δ are still above the detectability threshold of CE except for those with zero or very small Δ. As for the intermediate P_t EOSs, the i-mode of all the models cannot be detected with the aLIGO detector. With CE, the i-mode of a few models within a narrow range of Δ are detectable. The cutoff frequency, $f_{\rm ISCO}$ (see Sec. 7.3), is also indicated in the figure with a vertical dashed line. The i-modes with resonant frequency above this limit cannot be detected from the inspiral signal alone. Since the i-mode frequency of the intermediate P_t models depends strongly on Δ as illustrated in Fig. 7.2, models with Δ larger than 15 MeV are beyond this cutoff frequency. Hence, only a few models with Δ between 5 to 15 MeV have the i-mode detectable with CE. For high P_t EOSs, since the central pressure is below P_t for models with 1.4 $M_\odot$, there is no i-mode being excited and therefore are not present in the figure.

We also consider the HS binaries consisting of two 1.8 $M_\odot$ HSs with the results shown in the right panel of Fig. 7.4. Compared to the 1.4 $M_\odot$ case, the low P_t models have lower $|\delta\bar{\phi}|$ in general, while that of the intermediate P_t models are within the same order of magnitude. Most of the HS models are below the detectability threshold of

[5]The amplitude of GWs is effectively enhanced by $\sqrt{N}$.

the aLIGO detectors except for a few low P_t models with large Δ, while there is still a considerable portion of the low P_t and intermediate P_t models within the detectable region of CE.

The 1.8 $M_\odot$ models with high P_t EOSs have a phase transition at the core, unlike the 1.4 $M_\odot$ models. These models, represented by magenta symbols in the right panel of Fig. 7.4, have low $|\delta\bar{\phi}|$ and are below the detectability threshold of both detectors. The points of the intermediate P_t models are less scattered than the 1.4 $M_\odot$ case, indicating a weaker dependence of $\bar{f}$ and $|\delta\bar{\phi}|$ on Δ. In contrast, the high P_t models show a widespread along $\bar{f}$, which is similar to the case with the 1.4 $M_\odot$ intermediate P_t models.

From the above discussion, we see that Δ affects the detectability in different ways depending on P_t. As Δ increases, the models in Fig. 7.4 shift towards larger values of $\bar{f}$ and $|\delta\bar{\phi}|$ in general. For the low P_t models, the i-mode frequency is generally below $f_{\rm ISCO}$ for the range of Δ corresponding to the CCS phase. Hence, the large Δ models would be more detectable due to their larger phase shift magnitude. On the other hand, the i-mode frequency of the high P_t models is more sensitive to Δ. Some models with large Δ have the i-mode frequency higher than $f_{\rm ISCO}$, which means the mode is not excited during the inspiral stage. As a result, the models with large Δ have a higher chance of being detected for the low P_t EOSs, while those with intermediate Δ are the most detectable ones for the intermediate P_t EOSs. This is similar to the case with 1.4 $M_\odot$ HSs.

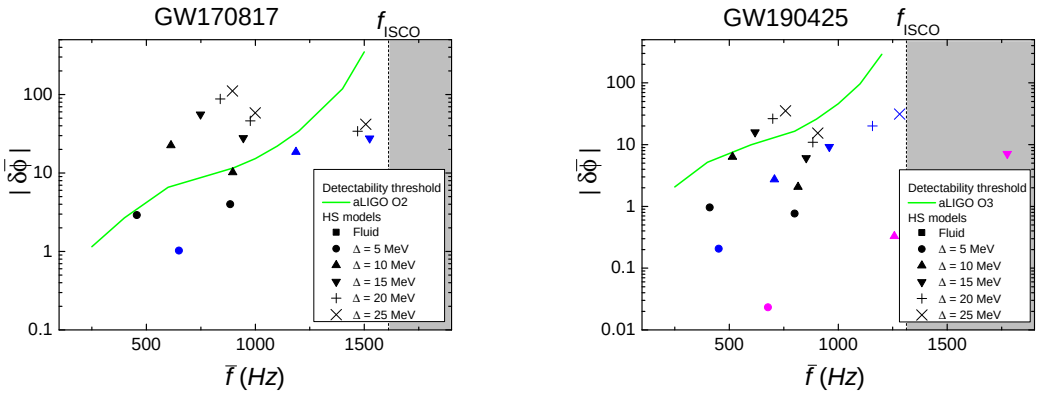

Figure 7.5: (Left) Similar to Fig. 7.4 but for parameters consistent with GW170817. The detection threshold curve is computed with the noise curve of aLIGO O2 run. We present the intermediate P_t models (Heb3-QM-3 in blue) and low P_t models (MS1-QM, Heb3-QM-1 in black). (Right) Similar to the left panel but for parameters consistent with GW190425. The detection threshold curve is computed with the noise curve of the aLIGO O3 run. We present the high P_t models (MPa1-QM in magenta), the intermediate P_t models (Heb3-QM-3 in blue) and low P_t models (MS1-QM, Heb3-QM-1 in black).

GW170817 and GW190425

Let us now study the GW events that have been detected, in particular GW170817 and GW190425 that are considered as binary NS mergers. If at least one of the stars in these events has a quark-hadron phase transition, the excitation of the i-mode will be encoded in the phase of the inspiral signal. We can apply the method from the previous subsection to analyze its detectability with the corresponding aLIGO run. In our Fisher analysis which gives us the threshold values of $|\delta\bar{\phi}|$, the parameters of the signal (m_1, m_2, d_L) are taken to be (1.46 $M_\odot$, 1.27 $M_\odot$, 40 Mpc) for GW170817 and (1.60 $M_\odot$, 1.75 $M_\odot$, 159 Mpc) for GW190425. The tidal deformability parameters $\bar{\Lambda}$ and $\delta\bar{\Lambda}$ are also adjusted accordingly. We take ($\bar{\Lambda}$, $\delta\bar{\Lambda}$) to be (588, 94) for GW170817 and (160, -20) for GW190425, which are computed with the formulation described in [120], assuming the Heb3-QM-1 EOS with a fluid core. Nevertheless, due to their negligible correlations with the i-mode parameters, fiducial values of the

tidal parameters should not have any significant impact on the numerical results. The noise spectral density data corresponding to the aLIGO second Observing run (O2) for GW170817 and the third Observing run (O3) for GW190425 respectively are obtained from [209]. We select the high P_t model MPa1-QM, intermediate P_t model Heb3-QM-3 and low P_t models M09m, Heb3-QM-1 from Table 7.1 for the analysis.

The left panel of Fig. 7.5 presents the detectability of HS models for GW170817 with the i-mode excitation during the inspiral. Part of the low P_t models with large Δ have $|\delta\bar{\phi}|$ above the detectability threshold. Certain models, even having a large Δ, are below the threshold due to the high resonant frequency. It is worth noting that the values of $|\delta\bar{\phi}|$ can go as high as $\sim$100 for large Δ, which is comparable to that of the f-mode (see, e.g., [41, 194], for values of $|I_{n\ell m}|$). The large value of the phase shift mainly comes from the secondary (1.27 $M_\odot$) HS in the binary. The intermediate P_t models have a smaller i-mode phase shift in general, and are below the threshold. The strong Δ dependence of the i-mode frequency for the intermediate P_t models makes the frequency go beyond $f_{\rm ISCO}$ when Δ is larger than 15 MeV.

Meanwhile, the models with the high P_t EOSs do not excite an i-mode during inspiral as they consist only of hadronic matter. These findings mean that if GW170817 consists of HSs with a low P_t EOS, it might be possible detect such a feature by performing a data analysis on the GW170817 data similar to that in [204, 210–212], given that the CCS Δ has a value larger than 10 MeV. On the other hand, if such an effect is absent, one should be able to constrain the parameter space of P_t and Δ of the HS EOSs provided we have reasonably good knowledge on the other EOS parameters.

In comparison, the right panel of Fig. 7.5 presents the results for GW190425. Observe that the detection threshold curve for this case is higher due to the increased luminos-

ity distance (and smaller SNR). The low P_t models also have smaller $|\delta\bar{\phi}|$, and some of the models are only marginally above the threshold. The intermediate P_t models and high P_t models are both below the threshold curve. This agrees with our finding in the previous subsection, that $|\delta\bar{\phi}|$ decreases for larger P_t in general. Besides, the secondary star with 1.60 $M_\odot$ with the high P_t EOS have a central pressure lower than P_t and therefore does not have a quark matter core. Therefore, only the primary star with a higher mass (1.75 $M_\odot$) in the binary contributes to the i-mode phase shift. This further lowers the value of $|\delta\bar{\phi}|$ of the high P_t models. Moreover, the higher mass of HSs in the binary leads to a smaller $f_{\rm ISCO}$, which makes the detection of the i-mode challenging for high resonant frequencies.

7.5 Chapter summary

In this chapter, we considered the i-mode of HSs with a CCS quark matter core and a hadronic matter envelope, which features an extremely rigid solid core and a fluid envelope. The phase transition is assumed to be first order with a density discontinuity. We studied the resonant excitation of the i-mode in HS-HS binary mergers during the inspiral and the corresponding phase shift on the emitted GW waveforms. We then estimated its detectability using a Fisher analysis.

We found that the i-mode resonant frequency and the phase shift are rather sensitive to change in the shear modulus of the CCS phase as well as P_t, the pressure corresponding to the first-order phase transition. We also found that the chance of detecting the i-mode is higher for EOSs with low P_t. For such low P_t models, the phase shift of the i-mode can be above the detection threshold limit if Δ is large enough, even for GW170817 (Fig. 7.5).

For the intermediate P_t EOSs, we showed that the sensitivity of aLIGO was insufficient to detect the i-mode due to the smaller magnitude of the phase shift. With the third-generation detectors like the CE, a portion of the models with intermediate values of Δ can be detected. However, those with a large Δ have high i-mode frequencies above the cutoff frequency for inspiral phase and therefore the mode is not excited. For the high P_t EOSs, quark matter appears inside the core only when the model has a high central pressure, namely the low mass models are simply hadronic NSs without a quark-hadron transition. Focusing on the high mass HSs with a high P_t phase transition, we found that the i-mode phase shift of such models is below the detectability threshold of the CE.

As explained in Appendix F.3, we find that the hybrid method in calculating the i-mode by combining a GR background model with Newtonian pulsation equations and Newtonian tidal coupling equations can potentially cause a factor of 2 difference in the GW phase shift predicted. A fully consistent GR method is required to accurately determine the detectability of the i-mode in HSs, which we leave for future work.

Chapter 8

Summary

In this thesis, we discuss several research topics in astrophysics, gravitation, and nuclear physics related to compact stars.

We begin with studying the measurability of tidal interactions in eccentric DWD binaries using LISA (Chapter 3). We demonstrate that the periastron precession rate causes amplitude modulation in the GW signal and allows us to measure not only the equilibrium tide, but also the dynamical component. This effect is found to be more measurable in higher mass systems as the radiation reaction effect due to GW emission helps constrain the eccentricity of the system.

We then discuss an improved iterative mapping method to compute the long-timescale binary orbit evolution under the influence of dynamical tide (Chapter 4). Compared to the previous formalism that focuses on highly eccentric orbits ($1-e \ll 1$), the new method is valid even for low eccentricities. This method is not restricted to compact star binaries but can be applied to generic binary stellar systems with tides.

In Chapter 5, we study the non-radial stellar pulsation modes of anisotropic NSs in full GR. We provide the formalism for the first time and check its consistency in the Cowling limit. By numerically solving these equations, we find $\ell = 2$ QNMs with complex frequencies as in the isotropic NSs. However, some of the p-modes have frequencies with negative imaginary parts when there is anisotropy, denoting

an unstable mode that grows with time. This instability leads to interesting further discussions as this implies at least the anisotropy models we study here cannot be long-lasting.

In Chapter 6, we present a study on testing GR using the theory-agnostic ppE waveform model with the GW signals from DWD binaries. We demonstrate that LISA can constrain the non-GR theories well with negative PN orders, which is consistent with previous literature. However, it requires prior constraints on the mass of the system to reach the same level as the most stringent bounds from pulsar observations. Furthermore, the astrophysical factors, like the magnetic interactions of the WDs, that affect the DWD orbital motion have a significant impact on the measurement of the non-GR parameters. Mismodelling of these effects can pose large systematic errors and invalidate the constraints on GR.

Lastly, we investigate the state of matter inside the NS core in Chapter 7. We focus on the HS models with an HM envelope and a QM core. We further assume the QM is in the crystalline phase known as the CCS phase. We propose using the i-mode resonance as a probe of the transition between the hadronic phase and quark phase, which causes a shift in the phase and time to coalescence in the GW signal. Through a Fisher analysis, we show that for models with low phase transition pressure P_t, the phase shift is detectable even with the current GW detectors if the shear modulus of the core is large enough.

There are multiple directions to extend the work presented in this thesis. Aside from the ones discussed in the individual chapter summaries, we can also consider applying the i-mode study on DWD systems to see how the resonance can affect the GW signals detected by LISA. Crystallized cores are expected to exist within WDs with a long cooling history [213]. Similar to the case of HSs, these i-modes are

expected to resonate at lower frequencies than the f-modes. Other than that, we can apply the new iterative method to studying the long-term evolution of eccentric DWD binaries. These systems are believed to form from dynamical channels within dense stellar clusters or through multiple body interactions. The dynamical tidal interactions can have an important impact on the formation and survival rates of these eccentric binaries, affecting the results of the population simulations.

Bibliography

[1] B. P. Abbott et al. (LIGO Scientific Collaboration and Virgo Collaboration), Phys. Rev. Lett. **116**, 061102 (2016).

[2] B. P. Abbott, R. Abbott, T. D. Abbott, M. R. Abernathy, K. Ackley, C. Adams, P. Addesso, R. X. Adhikari, V. B. Adya, C. Affeldt, et al., Class. Quantum Gravity **34**, 044001 (2017).

[3] M. Pitkin, S. Reid, S. Rowan, and J. Hough, Living Rev. Relativ. **14**, 10.12942/lrr-2011-5 (2011).

[4] *Lsc - ligo scientific collaboration*, https://www.ligo.org/index.php, [Online; accessed 25-Feburary-2024].

[5] P. Amaro-Seoane et al., *Laser interferometer space antenna*.

[6] S. Kawamura, M. Ando, T. Nakamura, K. Tsubono, T. Tanaka, I. Funaki, N. Seto, K. Numata, S. Sato, K. Ioka, et al., J. Phys. Conf. Ser. **122**, 012006 (2008).

[7] J. Gair, M. Hewitson, A. Petiteau, and G. Mueller, "Space-based gravitational wave observatories", in *Handbook of gravitational wave astronomy* (Springer Singapore, 2021), pp. 1–71.

[8] C. J. Moore, R. H. Cole, and C. P. L. Berry, Class. and Quantum Gravity **32**, 015014 (2014).

[9] E. E. Flanagan and T. Hinderer, Phys. Rev. D **77**, 021502 (2008).

[10] J. Vines, É. É. Flanagan, and T. Hinderer, Phys. Rev. D **83**, 084051 (2011).

[11] L. Wade, J. D. E. Creighton, E. Ochsner, B. D. Lackey, B. F. Farr, T. B. Littenberg, and V. Raymond, Phys. Rev. D **89**, 103012 (2014).

[12] E. Poisson and C. M. Will, *Gravity: newtonian, post-newtonian, relativistic* (Cambridge University Press, 2014).

[13] M. Maggiore, *Gravitational Waves. Vol. 2: Astrophysics and Cosmology* (Oxford University Press, Mar. 2018).

[14] J. S. Read, L. Baiotti, J. D. E. Creighton, J. L. Friedman, B. Giacomazzo, K. Kyutoku, C. Markakis, L. Rezzolla, M. Shibata, and K. Taniguchi, Phys. Rev. D **88**, 044042 (2013).

[15] D. Tsang, J. S. Read, T. Hinderer, A. L. Piro, and R. Bondarescu, Phys. Rev. Lett. **108**, 011102 (2012).

[16] Z. Pan, Z. Lyu, B. Bonga, N. Ortiz, and H. Yang, Phys. Rev. Lett. **125**, 201102 (2020).

[17] C. Chirenti, R. Gold, and M. C. Miller, Astrophys. J. **837**, 67 (2017).

[18] H. Yu and N. N. Weinberg, Mon. Not. R. Astron. Soc. **470**, 350 (2017).

[19] G. Pratten, P. Schmidt, and T. Hinderer, Nat. Commun. **11**, 10.1038/s41467-020-15984-5 (2020).

[20] H. H.-Y. Ng, P. C.-K. Cheong, L.-M. Lin, and T. G. F. Li, Astrophys. J. **915**, 108 (2021).

[21] S. Y. Lau and K. Yagi, Phys. Rev. D **103**, 063015 (2021).

[22] A. Passamonti, N. Andersson, and P. Pnigouras, Mon. Not. R. Astron. Soc. **504**, 1273 (2021).

[23] D. O. Gough, J. W. Leibacher, P. H. Scherrer, and J. Toomre, Science **272**, 1281 (1996).

[24] T. G. Cowling, Mon. Not. R. Astron. Soc. **101**, 367 (1941).

[25] M. Gabriel and R. Scuflaire, Acta Astron. **29**, 135 (1979).

[26] W. Unno, Y. Osaki, H. Ando, H. Saio, and H. Shibahashi, *Nonradial oscillations of stars* (University of Tokyo Press, 1989).

[27] J. P. Cox, *Theory of stellar pulsation* (Princeton University Press, 1980).

[28] P. N. McDermott, H. M. van Horn, and C. J. Hansen, Astrophys. J. **325**, 725 (1988).

[29] H. M. Lai, P. T. Leung, K. Young, P. W. Barber, and S. C. Hill, Phys. Rev. A **41**, 5187 (1990).

[30] P. T. Leung and K. M. Pang, J. Opt. Soc. Am. B: Opt. Phys. **13**, 805 (1996).

[31] C. Sauvan, T. Wu, R. Zarouf, E. A. Muljarov, and P. Lalanne, Opt. Express **30**, 6846 (2022).

[32] K. D. Kokkotas and B. G. Schmidt, Living Rev. Relativ. **2**, 10.12942/lrr-1999-2 (1999).

[33] Shah, S., van der Sluys, M., and Nelemans, G., A&A **544**, A153 (2012).

[34] B. Willems, A. Vecchio, and V. Kalogera, Phys. Rev. Lett. **100**, 041102 (2008).

[35] R. A. Mardling, Astrophys. J. **450**, 732 (1995).

[36] R. A. Mardling and S. J. Aarseth, Mon. Not. R. Astron. Soc. **321**, 398 (2001).

[37] P. B. Ivanov and J. C. B. Papaloizou, Mon. Not. R. Astron. Soc. **347**, 437 (2004).

[38] M. Vick and D. Lai, Mon. Not. R. Astron. Soc. **476**, 482 (2018).

[39] K. S. Thorne and A. Campolattaro, Astrophys. J. **149**, 591 (1967).

[40] L. Lindblom and S. L. Detweiler, Astrophys. J., Suppl. Ser. **53**, 73 (1983).

[41] K. D. Kokkotas and G. Schäfer, Mon. Not. R. Astron. Soc. **275**, 301 (1995).

[42] H. Sotani and T. Harada, Phys. Rev. D **68**, 024019 (2003).

[43] L. S. Finn, Mon. Notices Royal Astron. Soc. **245**, 82 (1990).

[44] C. J. Krüger, W. C. G. Ho, and N. Andersson, Phys. Rev. D **92**, 063009 (2015).

[45] S. Y. Lau, *Physical properties of compact stars containing crystalline color superconductors*, 2017.

[46] H. Heintzmann and W. Hillebrandt, Astron. Astrophys. **38**, 51 (1975).

[47] M. Karlovini and L. Samuelsson, Class. Quantum Gravity **20**, 3613 (2003).

[48] S. Nelmes and B. M. A. G. Piette, Phys. Rev. D **85**, 123004 (2012).

[49] P. S. Letelier, Phys. Rev. D **22**, 807 (1980).

[50] L. Herrera, Phys. Rep. **286**, 53 (1997).

[51] R. F. Sawyer and D. J. Scalapino, Phys. Rev. D **7**, 953 (1973).

[52] C. Y. Cardall, M. Prakash, and J. M. Lattimer, Astrophys. J. **554**, 322 (2001).

[53] S. S. Yazadjiev, Phys. Rev. D **85**, 044030 (2012).

[54] W. Barreto and S. Rojas, Astrophys. Space Sci. **193**, 201 (1992).

[55] D. J. Kaup, Phys. Rev. **172**, 1331 (1968).

[56] F. E. Schunck and E. W. Mielke, Class. Quantum Gravity **20**, R301 (2003).

[57] M. Alcubierre, J. Barranco, A. Bernal, J. C. Degollado, A. Diez-Tejedor, V. Jaramillo, M. Megevand, D. Núñez, and O. Sarbach, Class. Quantum Gravity **39**, 094001 (2022).

[58] D. Deb, S. R. Chowdhury, S. Ray, F. Rahaman, and B. Guha, Ann. Phys. (N. Y.) **387**, 239 (2017).

[59] A. Errehymy, M. Daoud, and E. H. Sayouty, Eur. Phys. J. C **79**, 10.1140/epjc/s10052-019-6862-9 (2019).

[60] P. H. R. S. Moraes, G. Panotopoulos, and I. Lopes, Phys. Rev. D **103**, 084023 (2021).

[61] C. Cattoen, T. Faber, and M. Visser, Class. Quantum Gravity **22**, 4189 (2005).

[62] C. B. M. H. Chirenti and L. Rezzolla, Class. Quantum Gravity **24**, 4191 (2007).

[63] R. L. Bowers and E. P. T. Liang, Astrophys. J. **188**, 657 (1974).

[64] S. Ş. Ş. Bayin, Phys. Rev. D **26**, 1262 (1982).

[65] W. Hillebrandt and K. O. Steinmetz, Astron. Astrophys. **53**, 283 (1976).

[66] K. Dev and M. Gleiser, Gen. Relativ. Gravit. **35**, 1435 (2003).

[67] M. Karlovini, L. Samuelsson, and M. Zarroug, Class. Quantum Gravity **21**, 1559 (2004).

[68] D. Horvat, S. Ilijić, and A. Marunović, Class. Quantum Gravity **28**, 025009 (2010).

[69] D. Horvat, S. Ilijić, and A. Marunović, Class. Quantum Gravity **28**, 195008 (2011).

[70] J. D. Arbañil and M. Malheiro, J. Cosmol. Astropart. Phys. **2016**, 012 (2016).

[71] A. A. Isayev, Phys. Rev. D **96**, 083007 (2017).

[72] J. M. Z. Pretel, Eur. Phys. J. C **80**, 10.1140/epjc/s10052-020-8301-3 (2020).

[73] D. D. Doneva and S. S. Yazadjiev, Phys. Rev. D **85**, 124023 (2012).

[74] T. B. Littenberg and N. Yunes, Class. Quantum Gravity **36**, 095017, 095017 (2019).

[75] R. Barbieri, S. Savastano, L. Speri, A. Antonelli, L. Sberna, O. Burke, J. Gair, and N. Tamanini, Phys. Rev. D **107**, 064073 (2023).

[76] E. Poisson, Phys. Rev. D **57**, 5287 (1998).

[77] D. Lai, Astrophys. J. Lett. **757**, L3 (2012).

[78] H. T. Cromartie, E. Fonseca, S. M. Ransom, P. B. Demorest, Z. Arzoumanian, H. Blumer, P. R. Brook, M. E. DeCesar, T. Dolch, J. A. Ellis, R. D. Ferdman, E. C. Ferrara, N. Garver-Daniels, P. A. Gentile, M. L. Jones, M. T. Lam, D. R. Lorimer, R. S. Lynch, M. A. McLaughlin, C. Ng, D. J. Nice, T. T. Pennucci, R. Spiewak, I. H. Stairs, K. Stovall, J. K. Swiggum, and W. W. Zhu, Nat. Astron. **4**, 72 (2019).

[79] M. C. Miller and F. K. Lamb and A. J. Dittmann and S. Bogdanov and Z. Arzoumanian and K. C. Gendreau and S. Guillot and A. K. Harding and W. C. G. Ho and J. M. Lattimer and R. M. Ludlam and S. Mahmoodifar and S. M. Morsink and P. S. Ray and T. E. Strohmayer and K. S. Wood and T. Enoto and R. Foster and T. Okajima and G. Prigozhin and Y. Soong, Astrophys. J. Lett. **887**, L24 (2019).

[80] T. E. Riley et al., Astrophys. J. Lett. **887**, L21 (2019).

[81] B. P. Abbott et al. (Virgo and LIGO Scientific Collaborations), Phys. Rev. Lett. **119**, 161101 (2017).

[82] B. P. Abbott et al., Astrophys. J. **892**, L3 (2020).

[83] E. Annala, T. Gorda, A. Kurkela, J. Nättilä, and A. Vuorinen, Nat. Phys. **16**, 907 (2020).

[84] U. H. Gerlach, Phys. Rev. **172**, 1325 (1968).

[85] K. Schertler, C. Greiner, J. Schaffner-Bielich, and M. Thoma, Nucl. Phys. A **677**, 463 (2000).

[86] V. Paschalidis, K. Yagi, D. Alvarez-Castillo, D. B. Blaschke, and A. Sedrakian, Phys. Rev. D **97**, 084038 (2018).

[87] K. Yagi and N. Yunes, Phys. Rev. D **88**, 023009 (2013).

[88] K. Yagi and N. Yunes, Science **341**, 365 (2013).

[89] K. Yagi and N. Yunes, Phys. Rep. **681**, Approximate Universal Relations for Neutron Stars and Quark Stars, 1 (2017).

[90] B. P. Abbott et al. (LIGO Scientific Collaboration and Virgo Collaboration), Phys. Rev. Lett. **119**, 161101 (2017).

[91] Z. Carson, K. Chatziioannou, C.-J. Haster, K. Yagi, and N. Yunes, Phys. Rev. D **99**, 083016 (2019).

[92] J. Kundu and K. Rajagopal, Phys. Rev. D **65**, 094022 (2002).

[93] M. Alford, J. A. Bowers, and K. Rajagopal, Phys. Rev. D **63**, 074016 (2001).

[94] R. Casalbuoni, R. Gatto, M. Mannarelli, and G. Nardulli, Phys. Rev. D **66**, 014006 (2002).

[95] M. Mannarelli, K. Rajagopal, and R. Sharma, Phys. Rev. D **73**, 114012 (2006).

[96] K. Rajagopal and R. Sharma, Phys. Rev. D **74**, 094019 (2006).

[97] M. Mannarelli, K. Rajagopal, and R. Sharma, Phys. Rev. D **76**, 074026 (2007).

[98] B. Haskell, N. Andersson, D. I. Jones, and L. Samuelsson, Phys. Rev. Lett. **99**, 231101 (2007).

[99] L.-M. Lin, Phys. Rev. D **76**, 081502 (2007).

[100] N. D. Ippolito, M. Ruggieri, D. H. Rischke, A. Sedrakian, and F. Weber, Phys. Rev. D **77**, 023004 (2008).

[101] B. Knippel and A. Sedrakian, Phys. Rev. D **79**, 083007 (2009).

[102] L.-M. Lin, Phys. Rev. D **88**, 124002 (2013).

[103] M. Mannarelli, G. Pagliaroli, A. Parisi, and L. Pilo, Phys. Rev. D **89**, 103014 (2014).

[104] S. Y. Lau, P. T. Leung, and L.-M. Lin, Phys. Rev. D **95**, 101302 (2017).

[105] J. P. Pereira, M. Bejger, L. Tonetto, G. Lugones, P. Haensel, J. L. Zdunik, and M. Sieniawska, Astrophys. J. **910**, 145 (2021).

[106] A. L. Piro and L. Bildsten, Astrophys. J. **619**, 1054 (2005).

[107] S. L. Shapiro and S. A. Teukolsky, *Black holes, white dwarfs, and neutron stars: the physics of compact objects* (Wiley, July 1983).

[108] S. Carroll, *Spacetime and geometry*, en (Pearson Education, Philadelphia, PA, Sept. 2003).

[109] K. S. Thorne, in High energy astrophysics, volume 3, Vol. 3, edited by C. Dewitt, E. Schatzman, and P. Véron (Jan. 1967), p. V.

[110] *Compose - compstar online supernovae equation of state*, `https://compose.obspm.fr/home`, [Online; accessed 25-Feburary-2024].

[111] F. Douchin and P. Haensel, Astron. Astrophys. **380**, 151 (2001).

[112] E. Chabanat, P. Bonche, P. Haensel, J. Meyer, and R. Schaeffer, Nucl. Phys. A **627**, 710 (1997).

[113] G. A. Lalazissis, J. König, and P. Ring, Phys. Rev. C **55**, 540 (1997).

[114] M. Alford, M. Braby, M. Paris, and S. Reddy, Astrophys. J. **629**, 969 (2005).

[115] P. Haensel, A. Y. Potekhin, and D. G. Yakovlev, *Neutron Stars 1 : Equation of State and Structure* (Springer-Verlag New York, 2007).

[116] J. A. Burns, Am. J. Phys. **44**, 944 (1976).

[117] C. D. Murray and S. F. Dermott, *Solar system dynamics*, en (Cambridge University Press, Cambridge, England, Feb. 2000).

[118] T. Pitre and E. Poisson, Phys. Rev. D **109**, 064004 (2024).

[119] A. H. K. R., J. L. Ripley, and N. Yunes, *Dynamical tidal response of non-rotating relativistic stars*, 2024.

[120] T. Hinderer, Astrophys. J. **677**, 1216 (2008).

[121] T. Damour and A. Nagar, Phys. Rev. D **80**, 084035 (2009).

[122] T. Binnington and E. Poisson, Phys. Rev. D **80**, 084018 (2009).

[123] T. K. Chan, A. P. O. Chan, and P. T. Leung, Phys. Rev. D **91**, 044017 (2015).

[124] T. Regge and J. A. Wheeler, Phys. Rev. **108**, 1063 (1957).

[125] A. K. Schenk, P. Arras, É. É. Flanagan, S. A. Teukolsky, and I. Wasserman, Phys. Rev. D **65**, 024001 (2001).

[126] N. N. Weinberg, P. Arras, E. Quataert, and J. Burkart, Astrophys. J. **751**, 136 (2012).

[127] D. Lynden-Bell and J. P. Ostriker, Mon. Not. R. Astron. Soc. **136**, 293 (1967).

[128] J. L. Friedman and B. F. Schutz, Astrophys. J. **221**, 937 (1978).

[129] W. A. Dziembowski, Acta Astron. **21**, 289 (1971).

[130] J. L. Friedman and B. F. Schutz, Astrophys. J. **222**, 281 (1978).

[131] L. Landau and E. Lifshits, *Theory of elasticity* (Pergamon, 1959).

[132] M. Maggiore, *Gravitational waves* (Oxford University Press, London, England, Oct. 2007).

[133] C. Cutler and E. E. Flanagan, Phys. Rev. **D49**, 2658 (1994).

[134] S. Y. Lau, K. Yagi, and P. Arras, Phys. Rev. D **106**, 103038 (2022).

[135] F. Valsecchi, W. M. Farr, B. Willems, C. J. Deloye, and V. Kalogera, Astrophys. J. **745**, 137 (2012).

[136] P. P. Eggleton, Astrophys. J. **268**, 368 (1983).

[137] F. Verbunt and S. Rappaport, Astrophys. J. **332**, 193 (1988).

[138] J. Papaloizou and J. E. Pringle, Mon. Not. R. Astron. Soc. **182**, 423 (1978).

[139] D. Lai, Astrophys. J. **490**, 847 (1997).

[140] P. Pnigouras, F. Gittins, A. Nanda, N. Andersson, and D. I. Jones, Mon. Not. R. Astron. Soc. **527**, 8409 (2023).

[141] P. Hut, Astron. Astrophys. **99**, 126 (1981).

[142] P. C. Peters and J. Mathews, Phys. Rev. **131**, 435 (1963).

[143] C. Moreno-Garrido, E. Mediavilla, and J. Buitrago, Mon. Not. R. Astron. Soc. **274**, 115 (1995).

[144] C. Cutler, Phys. Rev. D **57**, 7089 (1998).

[145] L. Lindblom, B. J. Owen, and D. A. Brown, Phys. Rev. D **78**, 124020 (2008).

[146] J. S. Read, C. Markakis, M. Shibata, K. ō. Ury ū, J. D. E. Creighton, and J. L. Friedman, Phys. Rev. D **79**, 124033 (2009).

[147] I. MacDonald, S. Nissanke, and H. P. Pfeiffer, Class. Quantum Gravity **28**, 134002 (2011).

[148] L. Barack and C. Cutler, Phys. Rev. D **69**, 082005 (2004).

[149] W. Junker and G. Schäfer, **254**, 146 (1992).

[150] W. H. Press and S. A. Teukolsky, Astrophys. J. **213**, 183 (1977).

[151] S. L. Detweiler and J. R. Ipser, Astrophys. J. **185**, 685 (1973).

[152] L. M. Becerra, E. A. Becerra-Vergara, and F. D. Lora-Clavijo, *Realistic anisotropic neutron stars: pressure effects*, 2024.

[153] S. R. Mohanty, S. Ghosh, P. Routaray, H. C. Das, and B. Kumar, *The impact of anisotropy on neutron star properties: insights from i-f-c universal relations*, 2023.

[154] J. L. Friedman and B. F. Schutz, Astrophys. J. **200**, 204 (1975).

[155] S. Detweiler and L. Lindblom, Astrophys. J. **292**, 12 (1985).

[156] K. S. Thorne, in High energy astrophysics, volume 3, Vol. 3, edited by C. Dewitt, E. Schatzman, and P. Véron (Jan. 1967), p. V.

[157] J.-L. Lü and W.-M. Suen, Chin. Phys. B **20**, 040401 (2011).

[158] M. Aizenman, P. Smeyers, and A. Weigert, Astron. Astrophys. **58**, 41 (1977).

[159] A. Kunjipurayil, T. Zhao, B. Kumar, B. K. Agrawal, and M. Prakash, Phys. Rev. D **106**, 063005 (2022).

[160] J. R. Ipser, Astrophys. J. **199**, 220 (1975).

[161] S. Chandrasekhar, Phys. Rev. Lett. **24**, 611 (1970).

[162] S. Tahura and K. Yagi, Phys. Rev. D **98**, [Erratum: Phys.Rev.D 101, 109902 (2020)], 084042 (2018).

[163] M. J. Benacquista, Astrophys. J. **740**, L54 (2011).

[164] T. R. Marsh, G. Nelemans, and D. Steeghs, Mon. Not. R. Astron. Soc. **350**, 113 (2004).

[165] K. Yagi and N. Yunes, Science **341**, 365 (2013).

[166] K. Yagi and N. Yunes, Phys. Rev. D **88**, 023009 (2013).

[167] K. Yagi and N. Yunes, Phys. Rept. **681**, 1 (2017).

[168] K. Boshkayev, H. Quevedo, and B. Zhami, Mon. Not. R. Astron. Soc. **464**, 4349 (2016).

[169] K. Boshkayev, H. Quevedo, Z. Kalymova, and B. Zhami, arXiv e-prints, 10.48550/arXiv.1409.2472 (2014).

[170] A. Wolz, K. Yagi, N. Anderson, and A. J. Taylor, Mon. Not. R. Astron. Soc.: Lett. **500**, L52 (2020).

[171] É. É. Flanagan and T. Hinderer, Phys. Rev. D **77**, 021502 (2008).

[172] K. Ioka and K. Taniguchi, Astrophys. J. **537**, 327 (2000).

[173] Z. Keresztes, B. Mikóczi, and L. Á. Gergely, Phys. Rev. D **72**, 104022 (2005).

[174] P. Goldreich and D. Lynden-Bell, Astrophys. J. **156**, 59 (1969).

[175] M. Lidov, Planet. Space Sci. **9**, 719 (1962).

[176] Y. Kozai, Astrophys. J. **67**, 591 (1962).

[177] S. Biscoveanu, K. Kremer, and E. Thrane, Astrophys. J. **949**, 95, 95 (2023).

[178] L. E. Kidder, C. M. Will, and A. G. Wiseman, Phys. Rev. D **47**, R4183 (1993).

[179] N. J. Cornish and L. J. Rubbo, Phys. Rev. D **67**, 022001 (2003).

[180] R. Takahashi and N. Seto, Astrophys. J. **575**, 1030 (2002).

[181] T. Robson, N. J. Cornish, and C. Liu, Class. Quantum Gravity **36**, 105011 (2019).

[182] R. Abbott et al. (LIGO Scientific, VIRGO, KAGRA), (2021).

[183] N. Yunes, K. Yagi, and F. Pretorius, Phys. Rev. D **94**, 084002 (2016).

[184] K. B. Burdge, T. A. Prince, J. Fuller, D. L. Kaplan, T. R. Marsh, P.-E. Tremblay, Z. Zhuang, E. C. Bellm, I. Caiazzo, M. W. Coughlin, et al., Astrophys. J. **905**, 32 (2020).

[185] J. J. Hermes, M. Kilic, W. R. Brown, D. E. Winget, C. A. Prieto, A. Gianninas, A. S. Mukadam, A. Cabrera-Lavers, and S. J. Kenyon, Astrophys. J. Lett. **757**, L21 (2012).

[186] T. Kinugawa, H. Takeda, A. Tanikawa, and H. Yamaguchi, Astrophys. J. **938**, 52 (2022).

[187] E. Poisson and C. M. Will, Phys. Rev. D **52**, 848 (1995).

[188] E. Berti, A. Buonanno, and C. M. Will, Phys. Rev. D **71**, 084025 (2005).

[189] C. Cutler and M. Vallisneri, Phys. Rev. D **76**, 104018 (2007).

[190] X. Zhang, T. Liu, and W. Zhao, Phys. Rev. D **95**, 104027 (2017).

[191] X. Zhang, W. Zhao, T. Liu, K. Lin, C. Zhang, X. Zhao, S. Zhang, T. Zhu, and A. Wang, Astrophys. J. **874**, 121 (2019).

[192] P. C. C. Freire, N. Wex, G. Esposito-Farèse, J. P. W. Verbiest, M. Bailes, B. A. Jacoby, M. Kramer, I. H. Stairs, J. Antoniadis, and G. H. Janssen, Mon. Not. R. Astron. Soc. **423**, 3328 (2012).

[193] X. Zhang, W. Zhao, T. Liu, K. Lin, C. Zhang, S. Zhang, X. Zhao, T. Zhu, and A. Wang,

[194] D. Lai, Mon. Not. R. Astron. Soc. **270**, 611 (1994).

[195] H. Müther, M. Prakash, and T. Ainsworth, Phys. Lett. B **199**, 469 (1987).

[196] T. Gaitanos, M. Di Toro, S. Typel, V. Baran, C. Fuchs, V. Greco, and H. Wolter, Nucl. Phys. A **732**, 24 (2004).

[197] H. Müller and B. D. Serot, Nucl. Phys. A **606**, 508 (1996).

[198] Y. Sugahara and H. Toki, Nucl. Phys. A **579**, 557 (1994).

[199] K. Hebeler, J. M. Lattimer, C. J. Pethick, and A. Schwenk, Astrophys. J. **773**, 11 (2013).

[200] T. Dietrich, M. W. Coughlin, P. T. H. Pang, M. Bulla, J. Heinzel, L. Issa, I. Tews, and S. Antier, Science **370**, 1450 (2020).

[201] Z. Alterman, H. Jarosch, and C. L. Pekeris, Proc. R. Soc. A: Math. Phys. Eng. Sci. **252**, 80 (1959).

[202] D. J. Crossley, Geophys. J. Int. **41**, 153 (1975).

[203] H. Yu and N. N. Weinberg, Mon. Not. R. Astron. Soc. **464**, 2622 (2016).

[204] Z. Pan, Z. Lyu, B. Bonga, N. Ortiz, and H. Yang, (2020).

[205] S. Husa, S. Khan, M. Hannam, M. Pürrer, F. Ohme, X. J. Forteza, and A. Bohé, Phys. Rev. D **93**, 044006 (2016).

[206] S. Khan, S. Husa, M. Hannam, F. Ohme, M. Pürrer, X. J. Forteza, and A. Bohé, Phys. Rev. D **93**, 044007 (2016).

[207] L. Wade, J. D. E. Creighton, E. Ochsner, B. D. Lackey, B. F. Farr, T. B. Littenberg, and V. Raymond, Phys. Rev. D **89**, 103012 (2014).

[208] J. Aasi, B. P. Abbott, R. Abbott, T. Abbott, M. R. Abernathy, K. Ackley, C. Adams, T. Adams, P. Addesso, R. X. Adhikari, et al., Class. Quantum Gravity **32** (2015).

[209] *Noise*, `https://dcc.ligo.org/LIGO-P1900011/public`.

[210] B. P. Abbott et al. (LIGO Scientific, Virgo), Phys. Rev. Lett. **122**, 061104 (2019).

[211] R. Essick and N. N. Weinberg, (2018).

[212] S. Reyes and D. A. Brown, Astrophys. J. **894**, 41 (2020).

[213] P.-E. Tremblay, G. Fontaine, N. P. G. Fusillo, B. H. Dunlap, B. T. Gänsicke, M. A. Hollands, J. J. Hermes, T. R. Marsh, E. Cukanovaite, and T. Cunningham, Nature **565**, 202 (2019).

[214] A. Einstein, L. Infeld, and B. Hoffmann, Ann. Math. **39**, 65 (1938).

[215] N. Seto, Phys. Rev. Lett. **87**, 251101 (2001).

[216] G. Giampieri, Mon. Not. R. Astron. Soc. **289**, 185 (1997).

[217] L. Barack and C. Cutler, Phys. Rev. D **69**, 082005 (2004).

[218] B. Carter and H. Quintana, Proc. R. Soc. A **331**, 57 (1972).

[219] L. Lindblom and R. J. Splinter, Astrophys. J. **348**, 198 (1990).

[220] T. Zhao, C. Constantinou, P. Jaikumar, and M. Prakash, Phys. Rev. D **105**, 103025 (2022).

[221] L. S. Finn, Mon. Not. R. Astron. Soc. **232**, 259 (1988).

[222] P. N. McDermott, H. M. van Horn, and J. F. Scholl, Astrophys. J. **268**, 837 (1983).

[223] R. Price and K. S. Thorne, Astrophys. J. **155**, 163 (1969).

[224] P. Amaro-Seoane, Phys. Rev. D **99**, 123025 (2019).

[225] K. B. Burdge, M. W. Coughlin, J. Fuller, T. Kupfer, E. C. Bellm, L. Bildsten, M. J. Graham, D. L. Kaplan, J. v. Roestel, R. G. Dekany, D. A. Duev, M. Feeney, M. Giomi, G. Helou, S. Kaye, R. R. Laher, A. A. Mahabal, F. J. Masci, R. Riddle, D. L. Shupe, M. T. Soumagnac, R. M. Smith, P. Szkody, R. Walters, S. R. Kulkarni, and T. A. Prince, Nature **571**, 528 (2019).

[226] A. Hook and J. Huang, J. High Energy Phys. **06**, 036 (2018).

[227] J. Huang, M. C. Johnson, L. Sagunski, M. Sakellariadou, and J. Zhang, Phys. Rev. D **99**, 063013 (2019).

[228] J. Huang, M. C. Johnson, L. Sagunski, M. Sakellariadou, and J. Zhang, Phys. Rev. D **99**, 063013 (2019).

[229] R. D. Peccei and H. R. Quinn, Phys. Rev. Lett. **38**, 1440 (1977).

[230] S. Weinberg, Phys. Rev. Lett. **40**, 223 (1978).

[231] F. Wilczek, Phys. Rev. Lett. **40**, 279 (1978).

[232] D. J. Marsh, Phys. Rep. **643**, 1 (2016).

[233] J. Preskill, M. B. Wise, and F. Wilczek, Phys. Lett. B **120**, 127 (1983).

[234] M. Arik et al. (CAST Collaboration), Phys. Rev. Lett. **107**, 261302 (2011).

[235] S. J. Asztalos, R. F. Bradley, L. Duffy, C. Hagmann, D. Kinion, D. M. Moltz, L. J. Rosenberg, P. Sikivie, W. Stoeffl, N. S. Sullivan, D. B. Tanner, K. van Bibber, and D. B. Yu, Phys. Rev. D **69**, 011101 (2004).

[236] D. Budker, P. W. Graham, M. Ledbetter, S. Rajendran, and A. O. Sushkov, Phys. Rev. X **4**, 021030 (2014).

[237] G. G. Raffelt, Phys. Rev. D **33**, 897 (1986).

[238] J. Ellis and K. Olive, Phys. Lett. B **193**, 525 (1987).

[239] H.-T. Janka, W. Keil, G. Raffelt, and D. Seckel, Phys. Rev. Lett. **76**, 2621 (1996).

[240] T. K. Poddar, S. Mohanty, and S. Jana, Phys. Rev. D **101**, 083007 (2020).

[241] J. Antoniadis, P. C. C. Freire, N. Wex, T. M. Tauris, R. S. Lynch, M. H. van Kerkwijk, M. Kramer, C. Bassa, V. S. Dhillon, T. Driebe, J. W. T. Hessels, V. M. Kaspi, V. I. Kondratiev, N. Langer, T. R. Marsh, M. A. McLaughlin, T. T. Pennucci, S. M. Ransom, I. H. Stairs, J. van Leeuwen, J. P. W. Verbiest, and D. G. Whelan, Science **340**, 1233232 (2013).

[242] J. P. Pereira, C. V. Flores, and G. Lugones, Astrophys. J. **860**, 12 (2018).

[243] N. K. Glendenning, Phys. Rev. D **46**, 1274 (1992).

[244] A. Bhattacharyya, I. N. Mishustin, and W. Greiner, J. Phys. G **37**, 025201 (2010).

Appendices

Appendix A

A.1 Abbreviations dictionary

Table A.1: Abbreviations used in the thesis.

WD	White dwarf
DWD	Double white dwarf
NS	Neutron star
HS	Hybrid star
GW	Gravitational wave
EOS	Equation of state
QCD	Quantum chromodynamics
QM	Quark matter
HM	Hadronic matter
HEOS	Hadronic equation of state
GR	General relativity
BH	Black hole
aLIGO	advanced Laser Interferometer Gravitational-Wave Observatory
KAGRA	Kamioka Gravitational Wave Detector
CE	Cosmic Explorer
ET	Einstein Telescope
LISA	Laser Interferometer Space Antenna
DECIGO	Deci-hertz Interferometer Gravitational-Wave Observatory
PN	Post-Newtonian
EM	Electromagnetic
g-mode	Gravity mode
f-mode	Fundamental mode
p-mode	Pressure mode
i-mode	Interfacial mode
QNM	Quasi-normal mode
RCA	Relativistic Cowling approximation
TOV equations	Tolman-Oppenheimer-Volkoff equations
ppE formalism	parametrized Post-Einsteinian formalism
SMG	Screened modified gravity
XMRI	Extreme-mass-ratio-inspiral
ISCO	Innermost stable circular orbit

A.2 Units and constants

We mainly use the geometrized unit system with $G = c = 1$. Another commonly used unit system is the cgs units. The masses of stars are usually expressed in terms of solar mass. The conversion of some of the constants are given below:

Constant	Symbol	Value (in cgs units)
Gravitational constant	G	6.67430×10^{-8} $\mathrm{cm^3 g^{-1} s^{-2}}$
Speed of light	c	2.99792458×10^{10} cm $\mathrm{s^{-1}}$
Solar mass	$M_\odot$	1.98855×10^{33} g
Astronomical unit	AU	1.495978707×10^{13} cm
Parsec	pc	3.08567758×10^{18} cm
Reduced Planck's constant	$\hbar$	1.0545718×10^{-27} erg s

Table A.2: The numerical values of the constants used in the following computations or unit conversions.

Appendix B

Measuring tides in eccentric double white dwarf binaries with gravitational waves

B.1 The numerical waveform

The far-field metric perturbation from the leading order GW emission is given by the quadrupole formula

$$h_{ij} = \frac{2\ddot{Q}_{ij}}{d}, \tag{B.1}$$

where Q_{ij} is the quadrupole moment of the source while d is the distance between the source and the point of observation. We consider only the quadrupole moment of the orbit and ignore the effects from the non-radial deformations of the individual WDs.

The orbit is governed by the equation

$$\mathbf{a} = -\frac{m_1 + m_2}{D^2}\mathbf{n} + \mathbf{a}_{\rm 1PN} + \mathbf{a}_{\rm tide}, \tag{B.2}$$

where $\mathbf{a}_{\rm 1PN}$ is the acceleration due to the 1PN effect while the tidal acceleration term $\mathbf{a}_{\rm tide}$ is given in Eq. (2.42). The dissipative effects like radiation reaction are ignored here. The 1PN effect is given by the Einstein-Infeld-Hoffmann equation [214]:

$$\begin{aligned}\mathbf{a}_{\rm 1PN} =& -\frac{m_1+m_2}{D^2}\Bigg\{\Bigg[(1+3\eta)\,\boldsymbol{v}\cdot\boldsymbol{v} - \frac{3}{2}\eta\,(\mathbf{n}\cdot\boldsymbol{v})^2 \\ & - 2\,(2+\eta)\,\frac{m_1+m_2}{D}\Bigg]\mathbf{n} - 2\,(2-\eta)\,(\mathbf{n}\cdot\boldsymbol{v})\,\boldsymbol{v}\Bigg\},\end{aligned} \tag{B.3}$$

where $\eta = m_1 m_2/(m_1+m_2)^2$ is the symmetric mass ratio and $\boldsymbol{v}$ is the relative velocity.

Equation (B.2) is numerically integrated and the result is substituted into Eq. (B.1) to obtain the quadrupolar waveform of the plus and cross polarizations, h_+ and $h_\times$ in the transverse-traceless gauge. The strain signal detected is written as

$$h_j(t) = F_+^j(t)h_+(t) + F_\times^j(t)h_\times(t), \tag{B.4}$$

where $j = I, II$, and F_+^j, $F_\times^j$ are the antenna pattern functions (see [144, 215–217]). The functions F_+^j and $F_\times^j$ depend on the source's angular position (θ_S, ϕ_S) and its orientation (θ_L, ϕ_L) in the ecliptic coordinate system. For simplicity, we set $\theta_L = \pi/4$ and the rest as zero here.

B.2 Peters and Mathews waveform

The Peters and Mathews waveform [142, 217] describes the leading order gravitational radiation emitted from a binary system in an eccentric Keplerian orbit. In this section, we write down the formulation of the waveform used in [142], without including the full evolution equations of the orbital elements.

Choosing the orbital plane as the x-y plane of the coordinate system, with the pericenter lying on the positive x-axis initially, the plus and cross polarizations are written as a sum of harmonics

$$h_+ = \frac{1}{d}\sum_k \Bigg\{ \left(1+\cos^2\iota\right)\Big[C_a^{(k)}\cos\left(k\Phi\right)\cos(2\gamma) - C_b^{(k)}\sin\left(k\Phi\right)\sin(2\gamma)\Big] + C_c^{(k)}\cos\left(k\Phi\right)\sin^2\iota\Bigg\}, \tag{B.5}$$

$$h_\times = \frac{2\cos\iota}{d}\sum_k \Big[C_a^{(k)}\cos\left(k\Phi\right)\sin(2\gamma) + C_b^{(k)}\sin\left(k\Phi\right)\cos(2\gamma)\Big], \tag{B.6}$$

where ι is the inclination angle of the source, given by

$$\cos\iota = \cos\theta_L\cos\theta_S + \sin\theta_L\sin\theta_S\cos\left(\phi_L-\phi_S\right), \tag{B.7}$$

and the precession is given by $\gamma = \dot{\gamma}t$ and $C_i^{(k)}$, with $i = a$, b, or c, are the Fourier coefficients of the quadrupole moment components:

$$\frac{1}{2}\left(\ddot{Q}_{11}-\ddot{Q}_{22}\right) = \sum_{k\neq 0} C_a^{(k)}\cos k\Phi(t), \tag{B.8}$$

$$\ddot{Q}_{12} = \sum_{k\neq 0} C_b^{(k)}\sin k\Phi(t), \tag{B.9}$$

$$\frac{1}{2}\left(\ddot{Q}_{11}+\ddot{Q}_{22}\right) = \sum_{k\neq 0} C_c^{(k)}\cos k\Phi(t). \tag{B.10}$$

In the Keplerian orbits, the coefficients can be written in terms of the Bessel functions:

$$C_a^{(k)} = -\frac{k}{2}\mu\left[(m_1+m_2)\Omega\right]^{2/3}\Big[J_{k-2}(ke) - 2eJ_{k-1}(ke) + \frac{2}{k}J_k(ke) + 2eJ_{k+1}(ke) - J_{k+2}(ke)\Big], \tag{B.11}$$

$$C_b^{(k)} = -\frac{k}{2}\mu\left[(m_1+m_2)\Omega\right]^{2/3}\sqrt{1-e^2}\Big[J_{k-2}(ke) - 2J_k(ke) + J_{k+2}(ke)\Big], \tag{B.12}$$

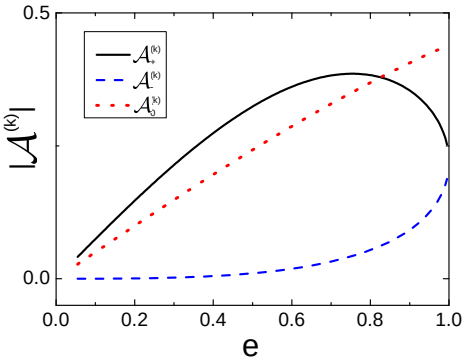

Figure B.1: The waveform amplitudes $\mathcal{A}_+^{(k)}$, $\mathcal{A}_-^{(k)}$ and $\mathcal{A}_0^{(k)}$ at different eccentricities for the $k = 1$ harmonic.

$$C_c^{(k)} = \mu \left[(m_1 + m_2)\Omega\right]^{2/3} J_k(ke), \tag{B.13}$$

where μ is the reduced mass of the binary. The effect of the tide and 1PN correction are included only through $\dot{\gamma}$. The amplitude corrections are not included as they are expected to be small within the parameter range of interest. The waveform model serves as a good approximation as long as $\dot{\gamma}$ is much smaller than Ω [143].

Without chirping, the precession effect splits each harmonic of the waveform into three distinct frequencies at $k\Omega$ and $k\Omega \pm 2\dot{\gamma}$. This can be illustrated by re-expressing Eqs. (B.5) and (B.6) in terms of $\mathcal{A}_\pm^{(k)} \cos\left(k\Omega t \pm 2\gamma\right)$ and $\mathcal{A}_0^{(k)} \cos\left(k\Omega t\right)$ as in [143, 215], where the amplitudes $\mathcal{A}_\pm^{(k)}$ and $\mathcal{A}_0^{(k)}$ are $(C_a^{(k)} \pm C_b^{(k)})/2$ and $C_c^{(k)}$ without the prefactor $\mu \left[(m_1 + m_2)\Omega\right]^{2/3}$. Using the series expansion of the Bessel functions, these amplitude terms can be shown to scale as $\mathcal{A}_+^{(k)} \sim e^{k-2}$ for $k \neq 1$ and $\mathcal{A}_+^{(k)} \sim e$ for $k = 1$, $\mathcal{A}_-^{(k)} \sim e^{k+2}$, and $\mathcal{A}_0^{(k)} \sim e^k$. Therefore, $\mathcal{A}_+^{(k)}$ has the largest amplitude while $\mathcal{A}_-^{(k)}$ is the smallest out of the three harmonics for low to intermediate eccentricities. The amplitude functions for the $k = 1$ harmonic at different eccentricities are shown in Fig. B.1. Except for large eccentricities ($e \gtrsim 0.5$), the relation $|\mathcal{A}_+^{(k)}| > |\mathcal{A}_0^{(k)}| > |\mathcal{A}_-^{(k)}|$

holds for all harmonics [34].

The chirping can be included through expanding the phase of each harmonic as $\Phi(t) = \Omega t + \dot{\Omega} t^2/2$, where $\dot{\Omega}$ contains the 2.5PN radiation reaction effect [142] given by

$$\dot{\Omega} = \frac{96}{5} \frac{\mu}{(m_1 + m_2)^3} (1 - e^2)^{-7/2} \left[(m_1 + m_2)\Omega\right]^{11/3} \left(1 + \frac{73}{24} e^2 + \frac{37}{96} e^4\right). \tag{B.14}$$

The Doppler phase term due to LISA's motion (see [144]) is not included in $\Phi(t)$ since we set $\theta_S = 0$.

Appendix C

An improved mapping method for the dynamical tide contributions to binary evolution

C.1 Derivation of the orbital element changes in the modified iterative mapping method

We first consider the term with the double integral after substituting Eq. (4.14) into Eq. (4.12), written as

$$\frac{\Delta a}{a} = \int_{-\pi}^{\pi} du f(u) \left(Q_\alpha^*(-\pi) e^{ik\pi} + \int_{-\pi}^{u} du' g(u') \right) + c.c. \tag{C.1}$$

where f and g are given by

$$f(u) = -\frac{\mathcal{B}}{\sqrt{1-e^2}} \left(\frac{1-e}{1-e\cos u} \right)^{\ell+1} e^{-im\Phi(u)+i\omega_\alpha t(u)} \left[(\ell+1) e \sin\Phi(u) + im(1+e\cos\Phi(u)) \right], \tag{C.2}$$

$$g(u) = -i\tilde{k}(1-e) \left(\frac{1-e}{1-e\cos u} \right)^{\ell} e^{-i\omega_\alpha t(u')+im\Phi(u')}. \tag{C.3}$$

We first focus on the second term in the integrand. Using the parity of the trigonometric functions, it can be shown that

$$\begin{aligned}\int_{-\pi}^{\pi} du \left(f(u) \int_{-\pi}^{u} du' g(u') \right) + c.c. =& 2\,\mathrm{Re}\left[\int_{-\pi}^{\pi} du \left(f(u) \int_{-\pi}^{0} du' g(u') \right) \right] \\ =& \,\mathrm{Re}\left[\int_{-\pi}^{\pi} du \left(f(u) \int_{-\pi}^{\pi} du' g(u') \right) \right] \\ =& \,\mathrm{Re}\left[\Delta Q_\alpha^* \int_{-\pi}^{\pi} du f(u) \right]. \end{aligned} \tag{C.4}$$

Note that the integral over u' now has a fixed integration limit and therefore can be separately integrated, giving us the last line of the equation. We are now left with two terms

$$\frac{\Delta a}{a} = \mathrm{Re}\left[\left(2Q_\alpha^*(-\pi) e^{ik\pi} + \Delta Q_\alpha^* \right) \int_{-\pi}^{\pi} du f(u) \right]. \tag{C.5}$$

The next step is to integrate $f(u)$. It turns out that the calculation is simpler if we make a variable transformation from the eccentric anomaly to the true anomaly:

$$\frac{1-e}{1-e\cos u} = \frac{1+e\cos\Phi}{1+e}, \tag{C.6}$$

and

$$du = \frac{\sqrt{1-e^2}}{1+e\cos\Phi} d\Phi. \tag{C.7}$$

Through an integration-by-part, we obtain

$$\int_{-\pi}^{\pi} du f(u) = -\,\mathcal{B}\left\{ -\left[\left(\frac{1+e\cos\Phi}{1+e} \right)^{\ell+1} e^{-im\Phi + i\omega_\alpha t(\Phi)} \right]_{-\pi}^{\pi} - \int_{-\pi}^{\pi} du g(u) \right\}$$

$$= \mathcal{B}\left(\Delta Q_\alpha^{(\mathrm{eq})} - \Delta Q_\alpha\right). \tag{C.8}$$

Combining Eqs. (C.8) and (C.5), we finally obtain Eq. (4.15).

C.2 The explicit forms of the orbital element integrals

The explicit forms of the functions in the integrand of Eqs. (4.22) and (4.23) are given in this section.

$$\begin{aligned} F_{\gamma 1} =& \frac{1}{e\sqrt{1-e^2}} \int_{-\pi}^{\pi} du \left(\frac{1-e}{1-e\cos u}\right)^{\ell+1} e^{-im\Phi(u)+i\omega_\alpha t(u)} \\ & \times \left[(\ell+1)\cos\Phi - im\sin\Phi\left(\frac{2+e\cos\Phi}{1+e\cos\Phi}\right)\right], \end{aligned} \tag{C.9}$$

$$\begin{aligned} F_{\gamma 2} =& -\frac{i\tilde{k}(1-e)}{e\sqrt{1-e^2}} \int_{-\pi}^{\pi} du \left(\frac{1-e}{1-e\cos u}\right)^{\ell+1} e^{-im\Phi(u)+i\omega_\alpha t(u)} \\ & \times \left[(\ell+1)\cos\Phi - im\sin\Phi\left(\frac{2+e\cos\Phi}{1+e\cos\Phi}\right)\right] \int_{-\pi}^{u} du' \left(\frac{1-e}{1-e\cos u'}\right)^{\ell} e^{-i\omega_\alpha t(u')+im\Phi(u')}, \end{aligned} \tag{C.10}$$

$$\begin{aligned} F_{\mathcal{T}1} =& \frac{1}{(1-e^2)^{5/2}} \int_{-\pi}^{\pi} du \left(\frac{1-e}{1-e\cos u}\right)^{\ell+1} e^{-im\Phi(u)+i\omega_\alpha t(u)} Q_\alpha^*(u) \\ & \times \left\{ \frac{3}{2\sqrt{1-e^2}}(u-e\sin u)\left[(\ell+1)e\sin\Phi + im(1+e\cos\Phi)\right] \right. \\ & \left. - (\ell+1)(1+e)(1-e\cos u) \right\}, \end{aligned} \tag{C.11}$$

$$\begin{aligned} F_{\mathcal{T}2} =& -\frac{i\tilde{k}(1-e)}{(1-e^2)^{5/2}} \int_{-\pi}^{\pi} du \left(\frac{1-e}{1-e\cos u}\right)^{\ell+1} e^{-im\Phi(u)+i\omega_\alpha t(u)} Q_\alpha^*(u) \\ & \times \left\{ \frac{3}{2\sqrt{1-e^2}}(u-e\sin u)\left[(\ell+1)e\sin\Phi + im(1+e\cos\Phi)\right] \right. \end{aligned}$$

$$- (\ell+1)(1+e)(1-e\cos u)\Bigg\} \int_{-\pi}^{u} du' \left(\frac{1-e}{1-e\cos u'}\right)^{\ell} e^{-i\omega_\alpha t(u')+im\Phi(u')}, \tag{C.12}$$

Appendix D

Unstable pulsation modes of anisotropic neutron stars

D.1 Direct form of the pulsation equations of anisotropic neutron stars

The governing equations of the perturbations from the perturbed Einstein equations and perturbed stress energy conservation are directly listed below. After a series of substitutions and simplifications, these equations reduce to four coupled first-order ordinary differential equations (Eqs. (5.18)-(5.21)) as described in Sec. 5.2.1.

$$\nabla_\alpha T^{\alpha t}=0: \quad \tilde{W}'=\ell(\ell+1)e^{\lambda/2}(1-\bar{\sigma})\tilde{V}+\frac{r^2}{2}e^{\lambda/2}(1-\bar{\sigma})\tilde{K} - \frac{r^2e^{\lambda/2}}{\rho+p_r}\left(\tilde{R}+\rho'\frac{e^{-\lambda/2}}{r^2}\tilde{W}\right)+\frac{2\bar{\sigma}}{r}\tilde{W} \tag{D.1}$$

$$(t,t): \quad 8\pi r^2\tilde{R}=e^{-\lambda}r^2\tilde{K}''+\left(3-\frac{r\lambda'}{2}\right)e^{-\lambda}r\tilde{K}'-\frac{(\ell-1)(\ell+2)}{2}\tilde{K} - e^{-\lambda}r\tilde{H}_0'-\left[(1-r\lambda')e^{-\lambda}+\frac{\ell(\ell+1)}{2}\right]\tilde{H}_0, \tag{D.2}$$

$$(r,t): \quad \tilde{K}'=\frac{\ell(\ell+1)}{2r^2}\tilde{H}_1+\left(\frac{\nu'}{2}-\frac{1}{r}\right)\tilde{K}-\frac{8\pi(\rho+p_r)e^{\lambda/2}}{r^2}\tilde{W}+\frac{1}{r}\tilde{H}_0, \tag{D.3}$$

$$(\theta-\phi,t): \quad \tilde{H}_1'=\left[4\pi(\rho-p_r)e^{\lambda}r+\frac{1-e^{\lambda}}{r}\right]\tilde{H}_1+e^{\lambda}\tilde{K}+e^{\lambda}\tilde{H}_0 + 16\pi(\rho+p_r)e^{\lambda}\left(1-\bar{\sigma}\right)\tilde{V}, \tag{D.4}$$

$$(r,r): \quad -8\pi r^2\tilde{P}_r = \left(1+\frac{r\nu'}{2}\right)re^{-\lambda}\tilde{K}' + \omega^2 e^{-\nu}r^2\tilde{K} - \frac{(\ell-1)(\ell+2)}{2}\tilde{K} - 2\omega^2 e^{-\nu-\lambda}r\tilde{H}_1 - e^{-\lambda}r\tilde{H}_0' + \left[\frac{\ell(\ell+1)}{2} - (1+r\nu')e^{-\lambda}\right]\tilde{H}_0, \tag{D.5}$$

$$(\theta-\phi,r): \quad \omega^2 e^{-\nu}\tilde{H}_1 = \tilde{K}' - \tilde{H}_0' - \nu'\tilde{H}_0, \tag{D.6}$$

$$(\theta-\phi,\theta-\phi): \quad -16\pi e^{\lambda}\left(\tilde{P}_r - \tilde{S}\right) = \tilde{K}'' + \left(\frac{2}{r}+\frac{\nu'-\lambda'}{2}\right)\tilde{K}' + \omega^2 e^{\lambda-\nu}\tilde{K} - \tilde{H}_0'' - \left(\frac{2}{r}+\frac{3\nu'}{2}-\frac{\lambda'}{2}\right)\tilde{H}_0' + \omega^2 e^{\lambda-\nu}\tilde{H}_0 - \left[\nu'' + \nu'\left(\frac{1}{r}+\frac{\nu'-\lambda'}{2}\right) - \frac{\lambda'}{r}\right]\tilde{H}_0 - \omega^2 e^{-\nu}\left[2\tilde{H}_1' + \left(\frac{2}{r}-\lambda'\right)\tilde{H}_1\right], \tag{D.7}$$

$$\nabla_\alpha T^{\alpha r} = 0: \quad \tilde{P}_r' = \frac{\rho+p_r}{r^2}e^{\lambda/2}\left(\omega^2 e^{-\nu} + \frac{\nu'}{2}e^{-\lambda}A\right)\tilde{W} - \left(1+\frac{1}{c_s^2}\right)\frac{\nu'}{2}\tilde{P}_r - \frac{\rho+p_r}{2}\tilde{H}_0' + (\rho+p_r)\bar{\sigma}\tilde{K}' - (\rho+p_r)\omega^2 e^{-\nu}\tilde{H}_1 - \frac{2}{r}\tilde{S}, \tag{D.8}$$

$$\nabla_\alpha T^{\alpha\theta} = 0: \quad \tilde{P}_r = \omega^2 e^{-\nu}(\rho+p_r)(1-\bar{\sigma})\tilde{V} - \frac{\rho+p_r}{2}\tilde{H}_0 + \tilde{S}. \tag{D.9}$$

Here, $\tilde{R}$, $\tilde{P}_r$, and $\tilde{S}$ are expansion coefficients defined through $\delta q = \sum_{\ell,m}\tilde{Q}Y_{\ell m}e^{i\omega t}$, where q and Q represents the set of quantities (ρ, p_r, σ) and $(\tilde{R}, \tilde{P}_r, \tilde{S})$ respectively. The perturbation variables with an overhead tilde are related to the perturbation variables in Sec. 5.2.1 in the following ways:

$$r^\ell K = \tilde{K}, \quad r^\ell H_0 = \tilde{H}_0, \quad r^\ell V = -\tilde{V}, \quad r^\ell S = \tilde{S}, \quad r^{\ell+1}H_1 = \tilde{H}_1, \quad r^{\ell+1}W = \tilde{W}. \tag{D.10}$$

D.2 Alternative derivation of Eq. (5.20)

In this section, we provide an alternative way to derive the pulsation equations, Eq. (5.20) in specific. Instead of using the t-component of Eq. (5.13), we utilize the continuity equation of particle number density and the relation of thermodynamics.

At the end, we explain how this method allows incorporating a more general form of the EOS in the perturbed configuration.

In the derivation of the pulsation equations for isotropic stars, it is common to introduce the particle number density, n, which is governed by the continuity equation (see, e.g., [154]):

$$\nabla_\alpha(nu^\alpha) = 0 \implies \frac{\Delta n}{n} = -\frac{1}{2}h^{\alpha\beta}\Delta g_{\alpha\beta}. \tag{D.11}$$

The number density is an independent variable in the EOS, i.e., $p = p(n)$, $\rho = \rho(n)$, but does not enter the equation of motion directly once we have ρ as a function of p. The pressure p here is the isotropic pressure. The Lagrangian perturbation of n is related to that of ρ through the thermodynamic relation

$$\Delta\rho = (\rho + p)\frac{\Delta n}{n}. \tag{D.12}$$

Combining Eqs. (D.11), (D.12) and the adiabatic relation $\gamma\Delta\rho/(\rho+p) = \Delta p/p$ gives the t-component of the stress energy conservation (Eq. (5.13)) of an isotropic fluid.

While Eq. (D.11) still holds in the anisotropic case, Eq. (D.12) needs to be modified, since the work done on the fluid does not depend only on the volume change, but is directional dependent. This requires us to explicitly write down the change in energy due to work done in each direction (see, e.g., [67, 131], for the generalized thermodynamic relations in an anisotropic medium):

$$\begin{aligned}\Delta\rho =& \rho\frac{\Delta n}{n} - p_r\Delta U^r{}_r - p_t(\Delta U^\theta{}_\theta + \Delta U^\phi{}_\phi)\\ =& (\rho + p_r)\frac{\Delta n}{n} + \sigma(\Delta U^\theta{}_\theta + \Delta U^\phi{}_\phi),\end{aligned} \tag{D.13}$$

where $\Delta U_{\alpha\beta}$ is the perturbative Lagrangian strain tensor [218] [1], given by

$$\Delta U_{\alpha\beta} = \Delta h_{\alpha\beta} = \frac{1}{2} h_\alpha{}^\mu h_\beta{}^\nu \Delta g_{\mu\nu}, \tag{D.14}$$

and $\Delta U^\alpha{}_\beta = g^{\alpha\mu}\Delta U_{\mu\beta}$. Equation (D.13), substituted with the adiabatic relation, Eq. (5.15), reads

$$\frac{\Delta p_r}{p_r} = \gamma \left[\frac{\Delta n}{n} + \bar{\sigma}(\Delta U^\theta{}_\theta + \Delta U^\phi{}_\phi) \right]. \tag{D.15}$$

One can show that this is equivalent to Eq. (5.20) using Eqs. (D.11) and (D.14), which are explicitly written as

$$\frac{\Delta n}{n} = \sum_{\ell,m} \left[\frac{1}{2} H_0 + K - \frac{e^{-\lambda/2}}{r} W' - \frac{\ell+1}{r^2} e^{-\lambda/2} W - \frac{\ell(\ell+1)}{r^2} V \right] r^\ell Y_{\ell m} e^{i\omega t}, \tag{D.16}$$

$$\Delta U^\theta{}_\theta + \Delta U^\phi{}_\phi = \sum_{\ell,m} \left[-K + 2e^{-\lambda/2} \frac{W}{r^2} + \frac{\ell(\ell+1)}{r^2} V \right] r^\ell Y_{\ell m} e^{i\omega t}. \tag{D.17}$$

Notice that in general, the anisotropic fluid can have different adiabatic constants in each direction depending on the anisotropy EOS. That is,

$$\frac{\Delta p_r}{p_r} = -\sum_i \gamma_i \Delta U^i{}_i, \tag{D.18}$$

where γ_i denotes the adiabatic index in the i-th spatial direction. We can even include the stress-strain relation in an elastic medium as given in [43, 44]. This suggests a further generalization of the pulsation equations described in Sec. 5.2.1. We leave it

[1] In fluid dynamics, it is more common to use the strain rate tensor to describe the deformation of fluid elements during the flow. Since each fluid element in the pulsating star oscillates about its equilibrium position, the strain rate just differs from the strain by a factor of $i\omega e^{-\nu/2}$.

for future studies.

D.3 Relativistic Cowling approximation of non-radial modes in anisotropic stars

To see how our equations reduce to the relativistic Cowling limit, we rewrite the variable X in terms of the Eulerian pressure perturbation,

$$\delta p_r = \sum_{\ell,m} r^\ell P_r Y_{\ell m} e^{i\omega t}, \tag{D.19}$$

and using its definition in terms of Δp, introduced in Sec. 5.2.1:

$$X = -e^{\nu/2} P_r - e^{(\nu-\lambda)/2} p_r' \frac{W}{r}. \tag{D.20}$$

To see how the pulsation equations reduce to the form in [73], it is better to express them in terms of differential equations of P_r. Substituting Eq. (D.20) into Eqs. (5.20) and (5.21), we obtain

$$W' = re^{\lambda/2}(1-\bar{\sigma})K + \left(-\frac{\ell+1}{r} + \frac{2\bar{\sigma}}{r} - \frac{p_r'}{\gamma p_r}\right) W - \frac{re^{\lambda/2}}{\gamma p_r} P_r + \frac{re^{\lambda/2}}{2} H_0 - \frac{\ell(\ell+1)}{r} e^{\lambda/2}(1-\bar{\sigma}) V, \tag{D.21}$$

$$\begin{aligned} P_r' = &- \frac{\rho + p_r}{2}\left[r\omega^2 e^{-\nu} + \frac{\ell(\ell+1)}{2r}(1-2\bar{\sigma})\right] H_1 - \frac{\rho+p_r}{2}(1-2\bar{\sigma})\left(\frac{\nu'}{2} - \frac{1}{r}\right) K \\ &+ \frac{\rho+p_r}{r} e^{\lambda/2}\left[4\pi(\rho+p_r)(1-2\bar{\sigma}) + \omega^2 e^{-\nu} + \frac{\nu'}{2} e^{-\lambda} A\right] W \\ &- \left[\frac{\ell}{r} + \left(1 + \frac{\rho+p_r}{\gamma p_r}\right)\frac{\nu'}{2}\right] P_r - \left[\frac{\rho+p_r}{2}\left(\frac{1}{r} - \frac{\nu'}{2}\right) + \frac{p_r'}{2}\right] H_0 - \frac{2}{r} S. \end{aligned} \tag{D.22}$$

We see that the differential equation with P_r is simpler than Eq. (5.21), since most of the lengthy terms in Eq. (5.21) come from the derivative of the terms other than P_r' within Eq. (D.20).

We also have

$$(\rho + p_r)(1-\bar{\sigma})\omega^2 e^{-\nu} V = -P_r - \frac{\rho + p_r}{2} H_0 + S. \tag{D.23}$$

To reduce Eqs. (D.21)-(D.23) to the relativistic Cowling limit given in [73] the approximation procedure is not by simply taking all metric perturbations to zero. The steps involved are the same as the isotropic case described in, e.g., [219, 220], where we set H_0, K, H_1 to zero in Eqs. (D.21)-(D.23), and further drop the term $4\pi(\rho+p_r)^2 e^{(\lambda+\nu)/2} W/r$ in the second line of Eq. (D.22). The reason for removing this term comes from Eq. (5.19) in the Cowling limit, assuming H_1 does not reduce to zero in the same way as H_0, K and K', leaving us an algebraic relation between H_1 and W. Reference [221] has given an argument about H_1 being larger than the other metric perturbations in the Newtonian limit[2].

The set of pulsation equations in relativistic Cowling approximation is explicitly given by

$$W' = \left(-\frac{\ell+1}{r} + \frac{2\bar{\sigma}}{r} - \frac{p_r'}{\gamma p_r}\right) W - \frac{r e^{\lambda/2}}{\gamma p_r} P_r - \frac{\ell(\ell+1)}{r} e^{\lambda/2}(1-\bar{\sigma}) V, \tag{D.24}$$

$$P_r' = \frac{\rho + p_r}{r} e^{\lambda/2} \left[\omega^2 e^{-\nu} + \frac{\nu'}{2} e^{-\lambda} A\right] W - \left[\frac{\ell}{r} + \left(1 + \frac{\rho + p_r}{\gamma p_r}\right) \frac{\nu'}{2}\right] P_r - \frac{2}{r} S, \tag{D.25}$$

$$P_r = -(\rho + p_r)(1-\bar{\sigma})\omega^2 e^{-\nu} V + S. \tag{D.26}$$

[2]The choice of H_1 leads to ambiguity in the Cowling limit of the full GR formalism. Reference [221] has provided another way to treat H_1, which leads to another version of relativistic Cowling approximation that works better for g-modes [219].

This set of equations is equivalent to Eqs. (27), (29) and (30) of [73] with a barotropic EOS, and can further be reduced to the isotropic limit of the relativistic Cowling approximation formulas [222].

D.4 Integral relation of the eigenvalue and eigenfunctions

As given in Eqs. (5.40) and (5.41), the eigenfrequencies and the eigenfunctions of the pulsation equations are related through the integral equations

$$\omega^2 \int_0^\infty (I_1 + J_1)dr = \int_0^\infty (I_2 + J_2)dr + I_3(R) + J_3(R) + I_4(\infty), \tag{D.27}$$

where J_1 to J_3 vanish in the isotropic limit and are non-zero only inside the star. In this section, we provide the explicit forms of the terms I_1 to I_4 and J_1 to J_3.

The terms I_1 to I_4 are obtained from Eq. (16) of [151], and are explicitly written as:

$$I_1 = e^{\frac{\lambda-\nu}{2}} r^2 \left\{ (\rho + p_r) \left[\frac{1}{r^4} \left| \tilde{W} \right|^2 + \frac{\ell(\ell+1)}{r^2} \left| \tilde{V} \right|^2 \right] - \frac{\ell(\ell+1)}{16\pi e^\lambda r^2} \left| \tilde{H}_1 \right|^2 - \frac{1}{16\pi} \left[\left| \tilde{K} \right|^2 + 2\,\mathrm{Re}\left(\tilde{K} \tilde{H}_0^* \right) \right] \right\}, \tag{D.28}$$

$$I_2 = e^{\frac{\lambda+\nu}{2}} r^2 \Bigg\{ - \frac{(\rho + p_r)\nu' A}{2e^\lambda r^4} |W|^2 + \frac{1}{\gamma p_r} \left| \tilde{P}_r \right|^2 + \left[\frac{\ell(\ell+1)}{16\pi r^2} - \frac{3(\rho + p_r)}{4} \right] \left| \tilde{H}_0 \right|^2 - \frac{1}{16\pi e^\lambda} \left| \tilde{K}' \right|^2 + \frac{\rho + p_r}{\gamma p_r} \mathrm{Re}\left(\tilde{P}_r \tilde{H}_0^* \right) - \frac{(\rho + p_r) A}{e^{\lambda/2} r^2} \mathrm{Re}(\tilde{W} \tilde{H}_0^*) + \frac{1}{8\pi e^\lambda} \mathrm{Re}\left[\left(\nu' \tilde{H}_0 + \tilde{H}_0' \right) \tilde{K}'^* \right] \Bigg\}, \tag{D.29}$$

$$I_3 = \frac{e^{\nu}\rho}{2}\left[2e^{-\nu/2}\,\mathrm{Re}\left(\tilde{W}\tilde{H}_0^*\right) + \frac{\nu'}{r^2}\left|\tilde{W}\right|^2\right], \tag{D.30}$$

$$I_4 = \frac{e^{\nu}r^2}{16\pi}\left[\tilde{K}^*\left(\tilde{H}_0' + \nu'\tilde{H}_0 - \tilde{K}'\right) - \tilde{K}'\tilde{H}_0^*\right]. \tag{D.31}$$

Here, $\tilde{P}_r$ is defined through $\delta p_r = \sum_{\ell,m}\tilde{P}_r Y_{\ell m}e^{i\omega t}$, and the symbol Re denotes taking the real part. The perturbation variables with overhead tilde are related to those defined in Sec. 5.2.1 through Eq. (D.10). We see that I_1 to I_3 are real while I_4 is in general complex if we impose the purely outgoing boundary condition at infinity [151, 223].

The terms J_1 to J_3 are derived using the procedures described in Appendix A of [151], with the Einstein equations and stress energy conservation in the anisotropic case.

$$J_1 = -\,\ell(\ell+1)e^{\frac{\lambda-\nu}{2}}(\rho+p_r)\bar{\sigma}\left|\tilde{V}\right|^2, \tag{D.32}$$

$$\begin{aligned} J_2 =& e^{\frac{\nu}{2}}\left[(\rho+p_r)\bar{\sigma}\left(-\tilde{K}' + \frac{2e^{-\frac{\lambda}{2}}A}{r^3}\tilde{W}\right) - \frac{2\bar{\sigma}}{r}\left(1+\frac{\rho+p_r}{\gamma p_r}\right)\tilde{P}_r + \frac{2}{r}\tilde{S}\right]\tilde{W}^* \\ &+ e^{\frac{\nu+\lambda}{2}}\left(\bar{\sigma}\tilde{P}_r + \frac{\rho+p_r}{2}\bar{\sigma}\tilde{H}_0 - \tilde{S}\right)\left[r^2\tilde{K}^* + \ell(\ell+1)\tilde{V}^*\right], \end{aligned} \tag{D.33}$$

$$J_3 = \frac{2e^{\nu}\rho}{r^3}\bar{\sigma}\left|\tilde{W}\right|^2. \tag{D.34}$$

The perturbation variables of the terms J_1 and J_3 are paired in the same way as I_1, while J_2 is in general complex as the complex perturbation variables cannot be paired in the same ways as I_1 to I_3. Although it is not obvious that the complex pulsation variables within J_2 cannot be paired up to form a real term, we verified this by numerically computing the integral using the solutions of the QNMs.

Appendix E

Testing gravity with double white dwarfs

E.1 Dependence of the statistical error on the observation time

The observation time dependence of $\Delta\gamma$ of the DWD system for $n = -1$ is shown in Fig. E.1, which follows a power law with an index of -3.78 at large $T_{\rm obs}$. Note that this scaling is close to the $T_{\rm obs}^{-3.5}$ dependence of the non-GR parameter in Eq. (17) of [75], where they show an approximate expression for the statistical error of the time-variation of the Newtonian gravitational constant using a similar waveform model as the one we use here.

We can also demonstrate this scaling by considering Eq. (6.20) in the large $T_{\rm obs}$ limit. The Fisher matrix element of the ppE parameter is given by

$$\begin{aligned}\mathbf{\Gamma}_{\gamma\gamma} \approx & \frac{\pi^2 \mathcal{A}^2 \nu^{2n}}{38115 S_n(f_0)} \Big[7623 \dot{f}_{\rm GR}^2 T_{\rm obs}^5 \\ & + 385(11+2n) \dot{f}_{\rm GR} \ddot{f}_{\rm GR} T_{\rm obs}^6 + 5 \ddot{f}_{\rm GR}^2 (11+2n)^2 T_{\rm obs}^7 \Big], \end{aligned} \tag{E.1}$$

where we have assumed $\mathcal{A}$ is time-independent for simplicity. Hence, for large $T_{\rm obs}$,

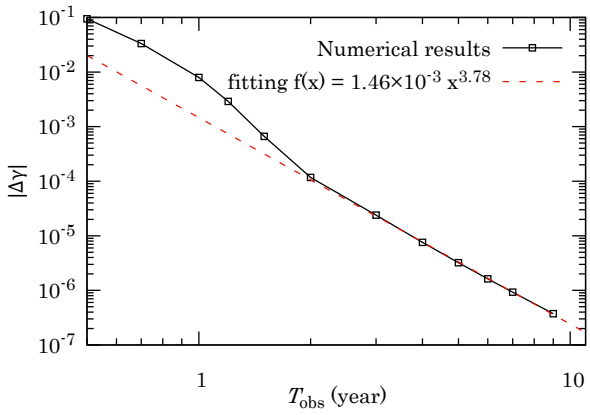

Figure E.1: The statistical error on γ of the DWD system in Table E.1 at different $T_{\rm obs}$ for $n = -1$. A fitting formula for the data points with $T_{\rm obs} \geq 3$ years is shown.

the $T_{\rm obs}^7$ term dominates. Similarly, $\mathbf{\Gamma}_{\mathcal{M}\gamma}$ and $\mathbf{\Gamma}_{\mathcal{M}\mathcal{M}}$ also have $T_{\rm obs}^7$ dependence in this limit. This causes $|\Delta\gamma|$ to scale as $T_{\rm obs}^{-3.5}$.

E.2 Constraints from other potential LISA sources

In this section, we repeat the calculation of the statistical uncertainties on γ presented in Sec. 6.2.1 for some other potential LISA quasi-monochromatic sources, including neutron star-white dwarf binaries (NS-WD), extreme-mass-ratio-inspiral (XMRI) [224], and the verification binary ZTF J1539+5027 (see Table E.1).

In Fig. E.2, we present the statistical uncertainties of the SMG non-GR parameter estimated by the Fisher matrix with the ppE model as described in Sec. 6.2.1 for various LISA sources. For the XMRI source, we assume it is composed of a $0.05M_\odot$ brown dwarf and a $4 \times 10^6 M_\odot$ supermassive black hole, emulating a GW source at the galactic center. All the sources contain at least one star with low compactness and therefore may give strong constraints on the SMG non-GR parameter. From

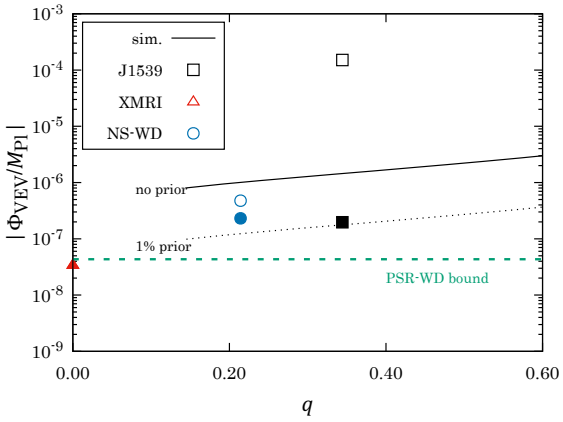

Figure E.2: The statistical error of the SMG non-GR parameter for various sources that are not considered in Fig. 6.5. The black lines correspond to the statistical error of the source shown in Fig. 6.5. For each source, the open symbol represents the statistical error without prior and the solid symbol represents that with a 1% Gaussian prior on the chirp mass.

the figure, we see that the statistical errors are comparable but are weaker than the current bound from PSR J1738+0333. One exception is the XMRI, due to its potentially large SNR [224] if the orbit is close enough. The population of these systems is currently uncertain[1]. We also expect the astrophysical systematics to be much smaller for XMRIs than DWDs due to the smaller radius and magnetic field strength of the brown dwarfs. That again means the GW measurement alone is insufficient to improve the bound on the SMG theories. Prior information on the chirp mass (e.g., 1% Gaussian priors on the chirp mass, as indicated by the solid symbols in Fig. E.2) is required for better constraints.

	SNR (1 yr)	ϕ_0 [rad]	ψ [rad]	ι [rad]	θ [rad]	ϕ [rad]	f_0 [mHz]	$\mathcal{M}$ [$M_\odot$]
sim.	95	2.2722	0.4413	0.7885	2.1405	4.3525	18.509	0.35
ZTF J1539+5027	14.9	–	–	1.4687	1.9869	−2.7048	4.8217	0.30
NS-WD	214	–	–	1.5708	1.7208	4.600	20.0	0.53
XMRI	19700	–	–	1.5708	1.7208	4.600	2.0	72.5

Table E.1: Source parameters of the DWD binaries. The simulated source (sim.) corresponds to source 4 of Table 1 in [74]. One of the LISA verification binaries, ZTF J1539+5027 [225], is also included. For the unspecified angles, we simply take the values as 0.

E.3 Constraining other non-GR theories

Theories involving axions are also a good candidate to test with DWD systems as the axion charges become larger for less compact stars [226–228]. Axion-like particles (ALPs) are pseudo-scalar fields that extend the standard model. One example is the QCD axions that are introduced to resolve the strong CP problem in quantum chromodynamics (QCD) [229–231]. ALPs are also popular dark matter (DM) candidates [232]. For QCD axion, it has been shown to account for the observed DM abundance if the decay constant is above 10^{12}GeV [233]. The ALP parameters have been constrained by both laboratory experiments [234–236] and astrophysical observations [237–239]. The addition of GW observations by LISA can provide an independent probe of such particles.

During inspiral, the extra force from the ALPs affects the orbital phase. In particular, the scalar Larmor radiation causes a change in the orbital decay rate [228, 240]. The effect depends on the axion dipole moment p of a binary sourced by the axion charges,

[1] In [224], they use a steady state power-law distribution function of the brown dwarfs to estimate that there are ∼20 such sources within 10^{-3} pc of the galactic center of the Milky Way. Around 5 are high-frequency sources with circular orbits. However, the actual event rate depends also on the formation and death rate of these systems.

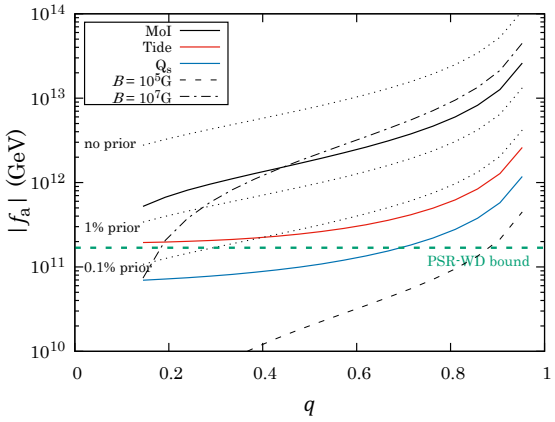

Figure E.3: Similar to Fig. 6.5 but showing the statistical and systematic errors of the axion decay constant f_a against the mass ratio q.

which can be approximated by

$$p = 4\pi f_a \mathcal{M}\eta^{2/5} r \left(C_1^{-1} - C_2^{-1}\right), \tag{E.2}$$

where f_a is the axion decay constant (see [240]). Relating to the ppE parameter, γ, defined in Eqs. (6.3) and (6.4), we have

$$\gamma = \frac{5\pi}{48}\eta^{2/5}\frac{G}{\hbar c^5} f_a^2 \left(\frac{1}{C_1} - \frac{1}{C_2}\right)^2. \tag{E.3}$$

Notice that Eq. (E.3) has similar dependence on η, γ and compactness as the SMG parameter in Eq. (6.27). Hence, similar constraints can be found using the DWD systems as shown in Fig. E.3.

In Fig. E.3, we show the statistical and systematic error of f_a in the same manner as Fig. 6.5. The statistical errors are obtained by imposing a Gaussian prior of different widths on the chirp mass and the current bound is obtained from the pulsar-WD binary PSR J0348+0432 [241] (a similar but less stringent bound is obtained from J1738+0333). Due to the similarity of the dependence of the non-GR parameter on

the WD parameters, the constraints obtained are qualitatively the same as SMG.

E.4 Derivation of the spin-induced quadrupole moment contribution to the frequency evolution

To derive the correction to the orbital decay rate due to the spin-induced quadrupole moment for a synchronized binary, we first identify the perturbation of the potential energy. Then, we derive the perturbation to the orbital radius as a function of orbital frequency (i.e., modified Kepler's third law). Finally, we apply the energy balance law to obtain the perturbation to the orbital decay rate. For simplicity, we assume the system is spin-aligned and consider the contribution of the quadrupole moment of star 1 only[2] and assume that the spin of the star remains synchronized with the orbit. As we sill see, this leads to a slightly different orbital decay rate from [76] that considered binaries without synchronization.

The potential of the binary system is given by

$$V(r) = -\frac{M}{r}\left(1 + \frac{Q_s}{2m_1 r^2}\right), \tag{E.4}$$

where M is the total mass of the binary, and the spin-induced quadrupole moment scalar is defined through

$$Q_{ij} = -Q_s\left(n_i n_j - \frac{1}{3}\delta_{ij}\right), \tag{E.5}$$

and the unit vector is set as $\boldsymbol{n} = (0, 0, 1)$. The radial component of the equation of

[2]The contribution from star 2 can easily be included by taking the correction, changing the index 1 and 2, and adding this to the correction from star 1 only)

motion can be obtained from Eq. (E.4):

$$\ddot{r} - r\Omega^2 = -\frac{M}{r^2}\left(1 + \frac{3Q_s}{2m_1 r^2}\right), \tag{E.6}$$

where $\ddot{r}$ is taken to be zero for circular orbits. The modified Kepler's law is given by

$$r = \left(\frac{M}{\Omega^2}\right)^{1/3}\left(1 + \frac{Q_s\Omega^{4/3}}{2m_1 M^{2/3}}\right). \tag{E.7}$$

The change in $\dot{f}$ is then determined by the rate of energy dissipation

$$\dot{f} = \frac{\dot{E}}{\pi\frac{dE}{d\Omega}}, \tag{E.8}$$

where $\Omega = \dot{\phi}$ and $\dot{E} = dE/dt$ is given by

$$\begin{aligned}\dot{E} =& -\frac{32}{5}\mu^2 r^4\Omega^6, \\ =& -\frac{32}{5}\mu^2 M^{4/3}\Omega^{10/3}\left(1 + 2\frac{Q_s\Omega^{4/3}}{M^{2/3}m_1}\right),\end{aligned} \tag{E.9}$$

and $\frac{dE}{d\Omega}$ is derived from $E(\Omega)$

$$\begin{aligned}E(\Omega) =& \frac{1}{2}\mu r^2\Omega^2 - \frac{M\mu}{r}\left(1 + \frac{Q_s}{2m_1 r^2}\right) \\ =& -\frac{1}{2}\mu M^{2/3}\Omega^{2/3}\left(1 - \frac{Q_s\Omega^{4/3}}{M^{2/3}m_1}\right).\end{aligned} \tag{E.10}$$

Here, we assume $Q_s \propto \Omega^2$, $\frac{dE}{d\Omega}$ is then

$$\frac{dE}{d\Omega} = -\frac{1}{3}\mu M^{2/3}\Omega^{-1/3}\left(1 - \frac{6Q_s\Omega^{4/3}}{M^{2/3}m_1}\right). \tag{E.11}$$

This leads to a different $\frac{dE}{d\Omega}$ from that in [76] which considered binaries that are not

synchronized.

By substituting Eqs. (E.9) and (E.11) into Eq. (E.8), we have $\Delta_{Q_s} = \dot{f}/\dot{f}_{\rm GR} - 1$:

$$\Delta_{Q_s} = \frac{8 Q_s \Omega^{4/3}}{M^{2/3} m_1}. \tag{E.12}$$

Appendix F

Probing crystalline quark matter within the neutron star core

F.1 Newtonian pulsation equations

The pulsation equations in Newtonian theory are described in Sec. 2.5. For numerical computation, the radial part of the equations is cast into a system of six coupled ordinary differential equations:

$$r\frac{dz_1}{dr} = -\left(1+2\frac{\alpha_2}{\alpha_3}\right)z_1 + \frac{1}{\alpha_3}z_2 + \ell\left(\ell+1\right)\frac{\alpha_2}{\alpha_3}z_3, \tag{F.1}$$

$$\begin{aligned} r\frac{dz_2}{dr} = &\left(-c_1V\Omega^2 - 4V + UV + 12\Gamma_1\frac{\alpha_1}{\alpha_3}\right)z_1 + \left(V - 4\frac{\alpha_1}{\alpha_3}\right)z_2 \\ &+ \ell\left(\ell+1\right)\left(V - 6\Gamma_1\frac{\alpha_1}{\alpha_3}\right)z_3 + \ell\left(\ell+1\right)z_4 + Vz_6, \end{aligned} \tag{F.2}$$

$$r\frac{dz_3}{dr} = -z_1 + \frac{1}{\alpha_1}z_4, \tag{F.3}$$

$$\begin{aligned} r\frac{dz_4}{dr} = &\left(V - 6\Gamma_1\frac{\alpha_1}{\alpha_3}\right)z_1 - \frac{\alpha_2}{\alpha_3}z_2 + \Bigg\{-c_1V\Omega^2 + \frac{2}{\alpha_3}\big[\left(2\ell(\ell+1)-1\right)\alpha_1\alpha_2 \\ &+ 2\left(\ell(\ell+1)-1\right)\alpha_1^2\big]\Bigg\}z_3 \\ &+ \left(V-3\right)z_4 + Vz_5, \end{aligned} \tag{F.4}$$

$$r\frac{dz_5}{dr} = \left(1-U\right)z_5 + z_6, \tag{F.5}$$

$$r\frac{dz_6}{dr} = U\left(-A_N r + \frac{V}{\Gamma_1} - 2 + 2\frac{\alpha_2}{\alpha_3}\right) z_1 - \frac{U}{\alpha_3} z_2 + \ell\,(\ell+1)\,U\left(1 - \frac{\alpha_2}{\alpha_3}\right) z_3 + \ell\,(\ell+1)\,z_5 - U z_6, \tag{F.6}$$

where the dependent variables z_1 to z_6 are defined as

$$z_1 = \frac{\xi_r}{r}, \tag{F.7}$$

$$z_2 = \alpha_2\left[\frac{1}{r^2}\frac{d}{dr}\left(r^2\xi_r\right) - \frac{\ell(\ell+1)}{r}\xi_\perp\right] + 2\alpha_1\frac{d\xi_r}{dr}, \tag{F.8}$$

$$z_3 = \frac{\xi_\perp}{r}, \tag{F.9}$$

$$z_4 = \alpha_1\left(\frac{d\xi_\perp}{dr} - \frac{\xi_\perp}{r} + \frac{\xi_r}{r}\right), \tag{F.10}$$

$$z_5 = \frac{\delta\Psi}{gr}, \tag{F.11}$$

$$z_6 = \frac{1}{g}\frac{d\delta\Psi}{dr}, \tag{F.12}$$

where g is the Newtonian gravitational acceleration given by m/r^2 and the functions Ω, c_1, α_1, α_2, α_3, A_N, U and V are defined as

$$\begin{aligned} &\Omega = \sqrt{\frac{R^3\omega^2}{M}}, \quad c_1 = \left(\frac{r}{R}\right)^3\frac{M}{m}, \quad A_N = \frac{1}{\rho}\frac{d\rho}{dr} - \frac{1}{\Gamma_1 p}\frac{dp}{dr}, \\ &\alpha_1 = \frac{\mu}{p}, \qquad \alpha_2 = \Gamma_1 - \frac{2}{3}\frac{\mu}{p}, \quad \alpha_3 = \Gamma_1 + \frac{4}{3}\frac{\mu}{p}, \\ &U = \frac{r}{m}\frac{dm}{dr}, \qquad V = -\frac{r}{p}\frac{dp}{dr}. \end{aligned} \tag{F.13}$$

Here M and R are the stellar mass and radius, $\Gamma_1 = \rho/p(\partial p/\partial\rho)_S$ is the adiabatic index defined in Sec. 2.5, A_N is the Newtonian Schwarzschild discriminant and it vanishes in cold compact objects except at the density discontinuities. Also see the definitions of ξ_r and $\xi_\perp$ in Eq. (2.50). Equations (F.1)–(F.6) describe the linear perturbations of the HS solid core. Notice that there are no independent equations

for $\delta\rho$ and δp since the variable $\delta\rho$ is related to z_2 through Eq. (F.8) and the perturbed continuity equation Eq. (2.45):

$$\frac{1}{r^2}\frac{d}{dr}\left(r^2\xi_r\right) - \frac{\ell(\ell+1)}{r}\xi_\perp = -\frac{\Delta\rho}{\rho}, \tag{F.14}$$

whereas the variable δp can be related to $\delta\rho$ through the linearized thermodynamic identity:

$$\frac{1}{\rho}\Delta\rho = \frac{1}{\Gamma_1 p}\Delta p. \tag{F.15}$$

Here Δf represents the Lagrangian perturbation of a variable f depending on r (see Sec. 2.5), which is related to the Eulerian perturbation δf by

$$\Delta f = \delta f + \xi_r \frac{df}{dr}. \tag{F.16}$$

To numerically obtain the pulsation modes, we integrate Eqs. (F.1)–(F.6) from the center to the stellar radius. At the solid-fluid interface, we employ continuity conditions of the pulsation variables z_1, z_2, z_4 and z_5. The continuity of z_1 is the direct consequence of the assumption that the volume element at the interface contains no void if the phase transition happens slowly compared to the pulsation motion (see e.g., [242]). The continuity of z_2 and z_4 comes from the continuity of the stress in the radial and tangential directions. Lastly, the Poisson equation guarantees the continuity of z_5[1].

The above equations for z_1–z_6 describe the pulsation problem of the solid core. Al-

[1]Note that z_3 and z_6, which are related to the tangential displacement and the first derivative of the gravitational potential perturbation respectively, are not required to be continuous. The former is the consequence of the so-called "free-slipping" condition and the latter is allowed by the Poisson equation.

though we can in principle obtain the pulsation equations inside fluid by taking the $\mu \to 0$ limit, it is straightforward to see that Eqs. (F.3) and (F.4) become trivial in this limit and we effectively have only four coupled differential equations. Therefore, it is often better to introduce another set of dependent variables for the fluid problem. Inside the fluid envelope, we employ the formulation by [129] (see also P.225 of [27]):

$$r\frac{dy_1}{dr} = \left(\frac{V}{\Gamma_1} - 3\right) y_1 + \left[\frac{\ell\left(\ell+1\right)}{c_1\Omega^2} - \frac{V}{\Gamma_1}\right] y_2 + \frac{V}{\Gamma_1} y_3, \tag{F.17}$$

$$r\frac{dy_2}{dr} = \left(c_1\Omega^2 + A_N r\right) y_1 + \left(1 - U - A_N r\right) y_2 + A_N r y_3, \tag{F.18}$$

$$r\frac{dy_3}{dr} = \left(1 - U\right) y_3 + y_4, \tag{F.19}$$

$$r\frac{dy_4}{dr} = -UA_N r y_1 + \frac{UV}{\Gamma_1} y_2 + \left[\ell\left(\ell+1\right) - \frac{UV}{\Gamma_1}\right] y_3 - U y_4. \tag{F.20}$$

Here the pulsation variables are given by

$$y_1 = z_1 = \frac{\xi_r}{r}, \tag{F.21}$$

$$y_2 = \frac{1}{gr}\left(\frac{\delta p}{\rho} + \delta\Psi\right), \tag{F.22}$$

$$y_3 = z_5 = \frac{\delta\Psi}{gr}, \tag{F.23}$$

$$y_4 = z_6 = \frac{1}{g}\frac{d\delta\Psi}{dr}. \tag{F.24}$$

y_2 is also related to $\xi_\perp$ through

$$y_2 = c_1\Omega^2 z_3 = \frac{\omega^2}{g}\xi_\perp. \tag{F.25}$$

Equation (F.22) implies that the continuity of radial stress across the interface is

equivalent to

$$[V\,(y_1 - y_2 + y_3)]_{\text{fluid}} = [z_2]_{\text{solid}}\,. \tag{F.26}$$

Here the square brackets "[ ]" with the subscripts "fluid" or "solid" indicates that the expression enclosed is evaluated at the fluid side or the solid side of the interface respectively.

To determine y_4 at the interface, one last continuity condition is derived by integrating Eq. (F.20) across the interface, using the fact that the derivative of ρ in A_N behaves like a Dirac delta function in r. Doing so, one can find:

$$[Uy_1 + y_4]_{\text{fluid}} = [Uz_1 + z_6]_{\text{solid}}\,. \tag{F.27}$$

This equation corresponds to the continuity of the Newtonian gravitational force at the perturbed interface.

At the surface, we have similar continuity conditions as Eqs. (F.26) and (F.27):

$$y_1 - y_2 + y_3 = 0, \tag{F.28}$$

$$Uy_1 + y_4 = -\,(\ell + 1)\,y_3, \tag{F.29}$$

where all quantities are evaluated at $r = R$. The second equation comes from the continuity of y_3 and we have applied the solution to the Poisson equation in vacuum (i.e., $\delta\Psi \propto r^{-\ell-1}$).

While integrating Eqs. (F.1)-(F.6) from $r = 0$ numerically for the solid core, we consider only the regular solutions, which can be obtained from a Taylor series expansion of z_1–z_6 near $r = 0$. We modify the expressions of the regular solutions derived by

[202] to fit our definition of pulsation variables:

$$z_1 = A_0 r^{\ell-2} + A_2 r^{\ell}, \tag{F.30}$$

$$z_2 = B_0 r^{\ell-2} + B_2 r^{\ell}, \tag{F.31}$$

$$z_3 = C_0 r^{\ell-2} + C_2 r^{\ell}, \tag{F.32}$$

$$z_4 = D_0 r^{\ell-2} + D_2 r^{\ell}, \tag{F.33}$$

$$z_5 = \frac{E_0}{gr} r^{\ell-2} + \frac{E_2}{gr} r^{\ell}, \tag{F.34}$$

$$z_6 = \frac{1}{g}\left[F_0 + 3\sigma A_0 - (\ell+1)E_0\right] r^{\ell-2} \tag{F.35}$$

$$+ \frac{1}{g}\left[(\ell+2)F_2 - 3\sigma A_2\right] r^{\ell}, \tag{F.36}$$

where the coefficients are related by

$$A_0 = \ell C_0, \tag{F.37}$$

$$B_0 = 2(\ell-1)\alpha_1 A_0, \tag{F.38}$$

$$D_0 = \frac{2\alpha_1(\ell-1)}{\ell} A_0, \tag{F.39}$$

$$E_0 = 3\sigma C_0 + \frac{1}{\ell} F_0, \tag{F.40}$$

$$C_2 = \frac{\beta_2}{\beta_1} D_2 + \frac{\rho}{p\beta_1}\left\{F_0 + \left[\omega^2 + (3-\ell)\sigma\right] A_0\right\}, \tag{F.41}$$

$$A_2 = -\ell C_2 + \frac{1}{\alpha_1} D_2, \tag{F.42}$$

$$B_2 = \gamma_1 C_2 + \gamma_2 D_2, \tag{F.43}$$

$$E_2 = \frac{3}{2}\sigma(2l-3)\left[(\ell+3)A_2 - \ell(\ell+1)C_2\right], \tag{F.44}$$

$$F_2 = (\ell+2)E_2 - 3\sigma A_2, \tag{F.45}$$

and σ, β_1,β_2, γ_1 and γ_2 are given by

$$\sigma = \frac{4\pi}{3}\rho, \tag{F.46}$$

$$\beta_1 = 2l^2(\ell+2)\alpha_2 + 2\ell(\ell^2+2l-1)\alpha_1, \tag{F.47}$$

$$\beta_2 = \ell(\ell+5) + \ell(\ell+3)\frac{\alpha_2}{\alpha_1}, \tag{F.48}$$

$$\gamma_1 = 2\ell(\ell+2)\alpha_2 + 2\ell(\ell+1)\alpha_1, \tag{F.49}$$

$$\gamma_2 = 2(\ell+1) + (\ell+3)\frac{\alpha_2}{\alpha_1}. \tag{F.50}$$

By choosing arbitrary values of C_0, D_2 and F_0 (or any 3 of the 12 coefficients), we can obtain three independent regular series solutions about $r = 0$ for the pulsation problem in the solid core.

If we consider HS models with a fluid quark matter core (i.e., the $\Delta = 0$ limit for the CCS phase), we also need the regular solutions for Eqs. (F.17)–(F.20) near $r = 0$. Following [129], the regular solutions satisfy the following equations

$$y_2 = \frac{c_1\omega^2}{\ell} y_1, \tag{F.51}$$

$$y_4 = \ell y_3. \tag{F.52}$$

Hence, there are two independent regular solutions at the center.

F.2 Maxwell Construction

The quark-hadron matter phase transition can either be of first or second order depending on the charge screening effect and the surface tension between the phases. They can respectively be constructed through a Maxwell construction or a Gibbs

construction which results in a mixed phase [243].

We focus on the Maxwell construction, which gives a first-order phase transition with a sharp density jump at the transition pressure P_t inside the HS. The transition point is determined by the following equations ([84, 244]):

$$P_t = p_1(\mu_B, \mu_e) = p_2(\mu_B, \mu_e), \tag{F.53}$$

$$\mu_B = \mu_{B1} = \mu_{B2}, \tag{F.54}$$

where μ_B, μ_e are the baryon chemical potential and electron chemical potential. The subscripts 1 and 2 of the pressure indicate the hadronic phase and the quark matter phase respectively. Average chemical potential of quarks μ_q is given by:

$$\mu_q = \frac{\mu_u + \mu_d + \mu_s}{3}. \tag{F.55}$$

Since three quarks form one baryon, we can relate the chemical potentials by

$$3\mu_q = \mu_B. \tag{F.56}$$

For a given NS EOS, μ_B can be determined with the Euler equation

$$\mu_B = \frac{\rho + p}{n_B}, \tag{F.57}$$

where ρ is the energy density and n_B is the baryon number density given by

$$n_B = n_n + n_p, \tag{F.58}$$

where n_n and n_p are the number density for neutrons and protons respectively.

F.3 Consistency check of the hybrid method

In this section, we comment on the validity of the hybrid method that we employed in our analysis. We solved the TOV equation to construct accurate HS background models, while we used *Newtonian* pulsation theory to compute the i-modes for simplicity and applied the method in [194] to compute the tidal coupling. Ideally, one should compare the results from such an approximate, hybrid method against a fully consistent analysis that solves relativistic perturbation equations. However, given that the framework for solving the latter has not been established yet, we instead follow Yu *et al.* [18] and compare the hybrid method against a fully-Newtonian one in which both the background and perturbation equations are solved within Newtonian gravity[2]. Such a study allows us to estimate the relativistic effect (in the background solution).

Δ (MeV)	Method	f(Hz)	$\lvert I_{n_i 22}\rvert$	$\lvert\delta\phi\rvert$
5	Full Newtonian	584.37	0.040	3.167
	Hybrid	443.03	0.020	1.136
15	Full Newtonian	1020.3	0.295	55.853
	Hybrid	714.86	0.143	21.901
25	Full Newtonian	1128.4	0.399	83.460
	Hybrid	863.44	0.248	45.009

Table F.1: The comparison of the numerical results of the 1.4 $M_\odot$ models with the EOS Heb3-QM-1 with a full Newtonian calculation and hybrid approach (TOV equations for background and Newtonian equations for pulsation and tidal coupling). Notice that the frequencies differ by about 25 % and phase shifts are off by a factor of a few.

To be more precise, Yu *et al.* [18] studied the detectability of dynamical tides for

[2]We should also emphasize that the full Newtonian approach, despite being consistent throughout the background, pulsation modes and tidal coupling calculations, is not the so-called "consistent" approach either since the background structure is not accurately determined. The Newtonian treatment in the pulsation mode and tidal coupling problem is also expected to have discrepancies in the size of M/R compared to that of the fully-GR formalism.

hyperon stars. They compared the deviation in the g-mode tidal coupling coefficient $I_{n\ell m}$ calculated with the hybrid method from that calculated with a full Newtonian approach and found that $I_{n\ell m}$ was off by less than 5%. Since the normalization of the eigenmodes in their study contains the mode frequencies, $I_{n\ell m}$ also has a different normalization constant compared to our definition (see Eq. (2.41)). We therefore compare the estimate of $\delta\phi$ in the two methods, which is independent of the normalization.

Table F.1 compares the oscillation properties (f, $|I_{n_i 22}|$ and $|\delta\phi|$) computed with the hybrid and Newtonian methods. We fix the stellar mass at $1.4M_\odot$ and use the EOS Heb3-QM-1[3] while varying Δ. Notice that the phase shift magnitude computed with the hybrid approach is smaller than that of the full Newtonian approach by a factor of a few. On the other hand, the difference in the oscillation frequency between the two methods is about 25%. Although the discrepancy in $\delta\phi$ between the two approaches for the i-mode is larger than that for the g-modes in [18], it is still within the same order of magnitude. Meanwhile, the i-mode phase shift changes by orders of magnitude as we vary the EOSs. Therefore, we expect that the discrepancy does not significantly affect our conclusion except for the marginal cases and we consider the hybrid approach to be a valid order of magnitude estimate of the phase shift. We leave the consistent analysis in full GR for future work.

[3]We choose Heb3-QM-1 out of the four low P_t EOS due to its lower i-mode frequency. For the other EOSs, there are avoided crossings as we change Δ between the i-mode and other modes which distort the wavefunction.